



저작자표시-비영리-변경금지 2.0 대한민국

이용자는 아래의 조건을 따르는 경우에 한하여 자유롭게

- 이 저작물을 복제, 배포, 전송, 전시, 공연 및 방송할 수 있습니다.

다음과 같은 조건을 따라야 합니다:



저작자표시. 귀하는 원저작자를 표시하여야 합니다.



비영리. 귀하는 이 저작물을 영리 목적으로 이용할 수 없습니다.



변경금지. 귀하는 이 저작물을 개작, 변형 또는 가공할 수 없습니다.

- 귀하는, 이 저작물의 재이용이나 배포의 경우, 이 저작물에 적용된 이용허락조건을 명확하게 나타내어야 합니다.
- 저작권자로부터 별도의 허가를 받으면 이러한 조건들은 적용되지 않습니다.

저작권법에 따른 이용자의 권리는 위의 내용에 의하여 영향을 받지 않습니다.

이것은 [이용허락규약\(Legal Code\)](#)을 이해하기 쉽게 요약한 것입니다.

[Disclaimer](#)

Ph.D. DISSERTATION

**STUDY ON THE SYNTHESIS AND ANALYSIS OF
DISTRIBUTED METALLIC NANOPARTICLES AND
THEIR PLASMONIC CHARACTERISTICS**

**금속 나노입자 분산구조의 합성과 그에 의한
플라즈모닉 특성 분석에 관한 연구**

By

HANSIK YUN

FEBRUARY 2013

DEPARTMENT OF ELECTRICAL ENGINEERING AND
COMPUTER SCIENCE
COLLEGE OF ENGINEERING
SEOUL NATIONAL UNIVERSITY

Abstract

STUDY ON THE SYNTHESIS AND ANALYSIS OF DISTRIBUTED METALLIC NANOPARTICLES AND THEIR PLASMONIC CHARACTERISTICS

HANSIK YUN
DEPARTMENT OF ELECTRICAL ENGINEERING AND
COMPUTER SCIENCE
COLLEGE OF ENGINEERING
SEOUL NATIONAL UNIVERSITY

Light interacts with electrons, atoms, and molecules in materials: light is reflected, refracted, or diffracted when it illuminates certain materials, while molecular structures of materials are sometimes transformed when they are stimulated by light. Since surface plasmons are also an interaction between photons of light and free electrons of metal materials, they can be an attractive research topic in many different fields in science and engineering, such as optical physics, electronics, chemistry, and material science. In this regard, it is necessary to conduct lively interdisciplinary study of surface plasmons to develop plasmonics as one of the next generation technology leaders. As an attempt to conduct the interdisciplinary research on surface plasmons, this dissertation demonstrated both chemical fabrication of various metallic nanoparticle arrays and optical analysis of their surface plasmons.

In this thesis, I suggested a new chemical method called site-selective synthesis, which enables to synthesize and align silver (Ag) nanoparticles simultaneously in a

designed trench. The mechanism of the site-selective synthesis method is that silver nanoparticles can be nucleated and grown selectively on polyvinylpyrrolidone (PVP) domains by attraction (or repulsion) between silver ions and the hydrophilic PVP island domains in a silica matrix of the trench (or the hydrophobic fluorosilane layer). On the silver nanoparticles in the trench, surface plasmons were excited by obliquely incident light, reradiating the enhanced electromagnetic fields in the far- and near-fields. Even for a large angle of incidence in total internal reflection (TIR), the patterned silver nanoparticle array underwent strong scattering with a high intensity, due to the surface plasmon effect. This research shows the possibility of designing metal nanoparticle arrays for a plasmonic device as well as increasing procedural efficiency in fabrication of metal nanoparticle arrays.

When metal nanoparticles become an array structure, plasmonic mixed states occur so that their optical properties change. A combined structure of metal nanoparticles on a metal layer was suggested in order to acquire a surface plasmon resonance (SPR) signal and a fluorescence image simultaneously based on the plasmonic mixed states of propagating surface plasmons (PSPs) and localized surface plasmons (LSPs). Although PSPs and LSPs generally have conflicting properties, i.e. propagation and localization of surface plasmons, they can coexist as a form of the mixed state on the proposed structure at an optimized condition. For the structure of Ag nanocubes with silicon dioxide shells on the Ag layer (AgNC@SiO₂), the plasmonic mixed states can appear in either interspaces among AgNC@SiO₂ particles, or SiO₂ gaps between AgNCs and Ag layers. As a result of scanning structural parameters, including an inter-particle distance, core size, shell thickness, and layer thickness, I found that a slope of the minimum reflectance band on the θ - λ_R map increased as AgNC@SiO₂ particles went close to one another. Decrease of the AgNC diameter and SiO₂ shell thickness also influenced on a slope and position of the band. Therefore, the slope of the minimum reflectance band means the proportion of LSPs to PSPs in their plasmonic mixed states. In particular, the real distribution of the inter-particle distances measured in experimental samples was fitted to the Weibull distribution and then the statistical data were fed back to a calculation process. As a result, the recalculation results agreed with the experimental θ - λ_R maps and

fluorescence images. This agreement supports the validity of the simulation approach and the experimental method used for investigating the proposed structure. Those plasmonic mixed properties of PSPs and LSPs will be useful in various practical applications such as bio sensors.

As part of an effort to understand a plasmonic coupling between PSPs and LSPs in depth, a densified lattice array structure of AgNC@SiO₂ without the Ag layer was proposed. I found the plasmonic intermediate state between PSPs and LSPs on the lattice array of AgNCs with few nanometer gaps through simulation and proved the existence of the intermediate property by using both a self-assembled monolayer (SAM) of AgNC@SiO₂ in experiment and a feedback of statistical data for gap distribution to a recalculation. The intermediate state has two distinguishing bands on the θ - λ_r map on the contrary to a PSP or LSP state which has only one of diagonal and vertical bands (D- and V-bands) on the map. Analysis of H_y -field profiles on the bands demonstrates the reversal transition between PSPs and LSPs in each other's band. The cross point between D- and V-bands becomes a metastable state, such as a saddle point, so that a breakage of PSP phase equilibrium, sudden discontinuity of LSPs, and rapid changes of the reflectance occur around that point.

As described above, this study suggested a new chemical method for metal nanoparticle arrays and investigated the plasmonic coupling and intermediate state between PSPs and LSPs using two kinds of metallic nanoparticle arrays. In order to conduct this research, chemical and optical approaches are used in the preparation of samples, measurement of plasmonic properties, and simulation analysis of the results. This complex approach is expected to be a model of interdisciplinary research.

Keywords: surface plasmon, propagating surface plasmon, localized surface plasmon, metal nanoparticle array, plasmonic mixed state, plasmonic intermediate state

Student number: 2009-30200

Contents

Abstract	i
Contents.....	iv
List of Figures.....	vi
Chapter 1. Introduction.....	1
1.1. Introduction of plasmonics	1
1.2. Fundamental principles of surface plasmons.....	2
1.3. Motivation of this dissertation	8
1.4. Scope and organization	10
Chapter 2. Site-selective synthesis of silver nanoparticles in a trench and their surface plasmons	12
2.1. Concept	13
2.2. Chemical fabrication.....	14
2.2.1. Experiment	14
2.2.2. Results and discussion.....	17
2.3. Optical measurement.....	24
2.3.1. Experiment	24
2.3.2. Results and discussion.....	25
2.4. Conclusion	32

Chapter 3. Plasmonic mixed states of PSPs and LSPs on AgNC@SiO₂ on Ag layer	34
3.1. Concept	36
3.2. Simulation	38
3.2.1. Effect of plasmonic mixed states on the minimum reflectance band	39
3.2.2. Effect of structural parameters on the position and intensity of the minimum reflectance band	42
3.3. Experiment	44
3.3.1. Chemical fabrication: AgNC@SiO ₂ on Ag layer	44
3.3.2. Optical measurement: dual detection of SPR signals and fluorescence images	45
3.3.3. Results and discussion	46
3.4. Conclusion	63
Chapter 4. Plasmonic intermediate states on AgNC@SiO₂ SAM	65
4.1. Concept	65
4.2. Simulation	67
4.2.1. Intermediate states of PSPs and LSPs	69
4.2.2. Effect of structural parameters on two minimum reflectance bands	73
4.3. Experiment	75
4.3.1. Chemical fabrication and optical measurement	75
4.3.2. Results and discussion	76
4.4. Conclusion	82
Chapter 5. Conclusion	84
Bibliography	86
국문 초록	95

List of Figures

Figure 1.1. Schematic illustration of (a) propagating surface plasmons on a thin metal layer and (b) localized surface plasmons on metal nanoparticles [9].	3
Figure 1.2. ω - k dispersion relationship of propagating surface plasmon.	4
Figure 1.3. (a) The Kretschmann configuration (b) Reflectance curve of a 50 nm thin silver layer as a function of incident angle. The minimum reflectance dip shifts toward a high incident angle as the refractive index of an environment increases.	5
Figure 1.4. Normalized extinction spectra for Ag wire, cube and sphere nanoparticles. Wire-shaped particles have 90 ± 12 nm diameter and >30 aspect ratio, cubic particles have 79 ± 12 nm edge length and spherical particles have 38 ± 12 nm diameter [13].	6
Figure 1.5. Two configurations of a pair of metal nanoparticles with respect to the polarization of the incident light. The dotted lines notify the induced electric field lines of the polarized particle.	7
Figure 1.6. Experimental extinction spectra of arrays of particle pairs for polarization (a) parallel and (b) perpendicular to the pair axis. The particle has a diameter of 150 nm and a height of 14 nm [17].	7
Figure 2.1. Schematic illustration of the mechanism for the site-selective synthesis of Ag nanoparticles in a trench.	14
Figure 2.2. Schematic procedure of site-selective synthesis of silver nanoparticles in trench.	16
Figure 2.3. SEM images of cross-sectional morphologies of (a)-(c) the PVP/silica layers and (d) the fluorosilane layer on a silicon wafer. The PVP/silica layers were prepared by mixing in ratios of PVP solution and silica sol solution as (a) 1:3, (b) 2:2, and (c) 3:1. The PVP domains are homogeneously distributed in the form of islands with diameters of ca. 10 nm. The thicknesses of the PVP/silica layer and fluorosilane layer are ca. 200 nm and ca. 10 nm. The striped region under the mixed layer is fragments of silicon wafer which occur naturally and horizontally when they are broken to determine the cross-	

section. Each scale bar is 100 nm. CCD images of a water droplet on (e) PVP/silica and (f) fluorosilane layer. The contact angle between the two black lines and the surface energies are indicated in the images..... 18

Figure 2.4. Schematic illustrations of circular shaped trenches packed with Ag nanoparticles: (a) sparse coverage, due to insufficient PVP island domains in the PVP/silica layer and (b) over-dense coverage, due to the over-exposure of the fluorine layer by FIB. (c)-(f) SEM images for each case. (g)-(i) SEM images of vacant trenches with three different widths and depths of (g) 100 nm, (h) 200 nm, and (i) 300 nm. The scale bars are (c) and (e) 2 μ m, (d) and (f) 100 nm, and (g)-(i) 200 nm. 20

Figure 2.5. SEM images of Ag nanoparticle-clusters in (a) rectangular, (b) triangular, and (c)-(h) circular trenches as results of the site-selective synthesis. Width, depth, and length (or diameter) of each trench are 100 nm, 100 nm, and 10 μ m, respectively. There are Ag nanoparticles with three different kinds of sizes in the same dimension. The Ag nanoparticle sizes are (a)-(d) 47 ± 12 nm, (e) and (f) 17 ± 8 nm, (g) and (h) bimodal distribution of 28 ± 9 nm and 94 ± 43 nm approximately. (d), (f), and (h) are magnified images of black boxes in (c), (e), and (g), respectively. The scale bars of (d), (f), and (h) are 100 nm and others are 2 μ m. 22

Figure 2.6. Average size and size distributions of Ag nanoparticles in Figures 2.5(d), (f), and (h), which were counted from SEM images. The average sizes are approximately 47 ± 12 nm (Figure 2.5(d)), 17 ± 8 nm (Figure 2.5(f)), and bimodal distribution of 28 ± 9 nm and 94 ± 43 nm (Figure 2.5(h)). The lines are drawn as a guide. 23

Figure 2.7. Graph showing the relationship between the intensity of CCD pixels and optical power. All scattering intensities measured in the far-field are included in the range from 0 to 25 μ W. The extrapolated line of data in the red dotted frame of the inset is shown as a red line. 25

Figure 2.8. Image of (a) total internal reflection (TIR) set-up with prism, laser, and microscope lens and (b) terminology for the direction of the trench and the polarization of incident light. (c) Picture of experimental set-up. The polarization of incident light is switchable between transverse electric (TE) and transverse magnetic (TM) polarization by a half wave plate before the laser source and the incident angle is changed from 34° to

70° by a motorized rotation stage. The CCD camera, which is not shown here, is adapted to microscopy. The incident light has no y -directional momentum. 27

Figure 2.9. Dark field images of rectangular trenches (a)-(c) without and (d)-(f) with Ag nanoparticles. (a) and (d) are reflective scattering images by an unpolarized white light, halogen source, with unspecific momentum, and the others are transmissive scattering images through a hemicylindrical prism (b) and (e) by TM polarized light, (c) and (f) by TE polarized light of 660 nm with incident angle of 44°. The orange colored arrows indicate the directional momentum of incident light on the xy -plane of the sample surface. The regions within the white dotted frames of (b) are the sample images used to calculate their average brightness which means the scattering intensity from Ag nanoparticles and trenches. Each scale bar is 2 μm 28

Figure 2.10. Graphs of scattered intensity vs. incident angle of (a) TM and (b) TE polarized light for the transmissive scattering images of the rectangular trenches with and without Ag nanoparticles. Some representative CCD images are inserted with their corresponding incident angles in the graphs. Laser source illuminates the sample through hemicylindrical prism with wavelength of 660 nm and incident angles from 34° to 70°. For convenience, Ag nanoparticles (NPs) are marked as AgNPs. 30

Figure 2.11. Transmission images of circular trench (a) without and (d) with Ag nanoparticles measured with a prism in TIR condition. NSOM images of circular trench (b) without and (e) with Ag nanoparticles measured with a prism in TIR condition. The enhanced near-field intensity profiles of cross-sections (the dotted lines QR and ST) of the images (b) and (e) are shown in (c) and (f). Laser source illuminates the sample with wavelength of 660 nm, TM polarization, and incident angle of 48°. Each scale bar is 2 μm 31

Figure 3.1. Schematic illustrations of (a) surface plasmon resonance sensor [78], (b) metal-enhanced fluorescence [79], and (c) the concept structure of Ag nanocubes with SiO₂ shell (AgNC@SiO₂) on thin metal layer for dual detection of SPR signal and fluorescence image..... 36

Figure 3.2. Schematic illustration of the proposed structure and parameters for simulation..... 38

Figure 3.3. Change of minimum reflectance band on θ - λ_R map depending on period....	40
Figure 3.4. θ - λ_R maps for Ag cores (30 nm) with SiO ₂ shell (10 nm) on Ag layer (50 nm) in (a) 100 nm and (b) 2000 nm of period condition. H_y -field profiles at (c) 69.55° and (d) 44.24° of different incident angles and 580 nm of same wavelength in different phase of incident light. Black open circles marked on the maps of (a) and (b) indicate positions where H_y -field profiles of (c) and (d) were calculated, respectively.....	41
Figure 3.5. Effect of SiO ₂ shell thickness on the minimum reflectance band. The thicknesses are (a) 1 nm, (b) 10 nm, and (c) 35 nm.	43
Figure 3.6. Effect of Ag core size on the minimum reflectance band. The diameters are (a) 20 nm, (b) 30 nm, and (c) 40 nm.	43
Figure 3.7. Effect of Ag layer thickness on the minimum reflectance band. The thicknesses are (a) 30 nm, (b) 50 nm, and (c) 70 nm.	44
Figure 3.8. Experimental set-up of the Kretschmann configuration.	46
Figure 3.9. TEM images of (a) AgNC and (b) AgNC@SiO ₂ . Molecular structures of (c) Fluorescein isothiocyanate (FITC) and (d) Rhodamine B isothiocyanate (RITC).	47
Figure 3.10. FE-SEM images of AgNC@SiO ₂ coated on Ag layer by (a) 20-, (b) 2.5-, (c) 1.25-fold dilutions, and (d) undiluted solution. The scale bars are 500 nm.	48
Figure 3.11. Reflectance spectra of (a) AgNC on glass, (b) AgNC@SiO ₂ on glass, (c) AgNC on Ag layer, and (d) AgNC@SiO ₂ on Ag layer in dark field mode. Blue, green, and red spectra were measured for samples of 2.5-fold, 1.25-fold dilutions, and undiluted solution.....	49
Figure 3.12. Optical microscope images of (a) Ag layer, (b) AgNC@SiO ₂ on glass, (c) AgNC@SiO ₂ on Ag layer, (d) AgNC@SiO ₂ with FITC on Ag layer, and (e) AgNC@SiO ₂ with RITC on Ag layer, which were measured in Kretschmann configuration. The thickness of the Ag layer is 50 nm, the diameter of AgNC is 30 nm, and the thickness of SiO ₂ shell is 10 nm.....	51
Figure 3.13. The experimental θ - λ_R maps of the samples coated on 50 nm Ag layer with (a) 20-fold, (b) 1.25-fold dilution, and (c) undiluted AgNC@SiO ₂ solutions.....	52
Figure 3.14. The Weibull distribution graphs with various values of α and β	54
Figure 3.15. Inter-particle distance distributions (a)-(c) measured in experimental data	

and (d)-(f) calculated with the average and standard deviation values of the samples. They follow the Weibull distributions: (a) and (d) for the undiluted, (b) and (e) for 1.25-fold, and (c) and (f) for 2.5-fold diluted AgNC@SiO₂ solutions 55

Figure 3.16. Schematic illustration of a structure and parameters for simulation including the Weibull distribution..... 56

Figure 3.17. Change of θ - λ_R maps depending on standard deviations, which are (a) 0 nm, (b) 10 nm, (c) 40 nm, and (d) 80 nm, in the Weibull distribution of inter-particle distance with an average distance of 117 nm..... 57

Figure 3.18. Effects of standard deviations on the convergence of the minimum reflectance at an incident angle of 60° and a wavelength of 600 nm in iteration of the simulation. The standard deviations are (a) 10 nm, (b) 40 nm, (c) 49 nm, and (d) 80 nm in the Weibull distribution of the inter-particle distance with 117 nm of the average distance. The green dots, the upper blue lines, and the lower red lines are raw, average, and standard deviation data of reflectance, respectively..... 58

Figure 3.19. H_y -field profiles of AgNCs (30 nm) with SiO₂ shell (10 nm) distributed on Ag layer (50 nm) at an incident angle of 50° and a wavelength of 650 nm. Their average distances are same, 117 nm, and their standard deviations are (a) 15 nm, (b) 27 nm, (c) 40 nm, (d) 49 nm, and (e) 80 nm. 59

Figure 3.20. Effect of unit (particle) number in a period on and convergence of reflectance. There are (a) 20, (b) 30, (c) 40, (d) 50, and (e) 60 of units per period in the Weibull distribution. The green dots, the upper blue lines, and the lower red lines are raw, average, and standard deviation data of reflectance, respectively..... 60

Figure 3.21. Comparisons of θ - λ_R maps for three kinds of inter-particle distances (a)-(c) without and (d)-(f) with the Weibull distribution. The three kinds of distances are: (a) and (d) 117 nm, (b) and (e) 200 nm, and (c) and (f) 300 nm. The standard deviations are (d) 40.1 nm, (e) 84.9 nm, and (f) 149.2 nm, which are same as the values of the experimental samples and Figure 3.15. 60

Figure 3.22. Comparison of three kinds of data for 20-fold dilution of AgNC@SiO₂ on Ag layer. They are (a) Experimental, (b) simulation θ - λ_R maps, and fluorescence images at (c) 44°, (d) 43°, and (e) 42°..... 62

Figure 3.23. Comparison of three kinds of data for the undiluted AgNC@SiO₂ solution on Ag layer. They are (a) Experimental, (b) simulation θ - λ_R maps, and fluorescence images at (c) 57°, (d) 55°, and (e) 51°. 62

Figure 3.24. Switching the fluorescent colors from red to green depending on the incident angle from (a) 51° to (b) 57°. 63

Figure 4.1. (a) Concept image of plasmonic intermediate state between PSPs and LSPs on a lattice array of the cubic units. (b) Structure and parameters used in simulation. One period includes one cubic unit. P , d , t , θ , and R are period, core diameter, shell thickness, incident angle, and reflectance. 67

Figure 4.2. θ - λ_R maps of (a) AgNC (35 nm) with shell (0 nm), (b) AgNC (35 nm) with shell (2 nm), and (c) AgNC (35 nm) with shell (17.5 nm). There are (a) D-band, (b) two hybrid bands, and (c) V-band. (d)-(f) θ - λ_R maps of structures corresponding to (a)-(c) for an environmental refractive index of 1.00 (air). 69

Figure 4.3. θ - λ_R maps of (a) AgNC (35 nm) with shell (17.5 nm) and (b) AgNC (35 nm) with shell (0 nm). H_y -field profiles at θ and λ_R of (c) 70° and 441 nm in (a), (c) 62° and 452 nm in (a), (e) 80° and 475 nm in (b), (f) 64.5° and 800 nm in (b). 71

Figure 4.4. (a) θ - λ_R map of AgNC (35 nm) with shell (2 nm) and H_y -field profiles at θ and λ_R of (b) 70° and 508 nm (c) 62° and 615 nm, (d) 50° and 637.5 nm, (e) 63.7° and 633 nm, (f) 70° and 652 nm, (g) 66.5° and 660 nm, and (h) 62.75° and 720 nm. (b)-(d) show transition from PSP to LSP and (f)-(h) show a transition from LSP to PSP. H_y -field profile of (e) shows a metastable state at a saddle point, O , on the θ - λ_R map of (a). 72

Figure 4.5. H_y -field profiles around the cross point or saddle point, O , on (a) θ - λ_R map for the lattice array of AgNC (43 nm) with shell (3.5 nm). 73

Figure 4.6. Effect of (a) shell thickness and (b) core diameter on two hybrid bands of θ - λ_R map. 74

Figure 4.7. H_y -field profiles of AgNC (35 nm) with shell thickness (t) at 70° and λ_R . t and λ_R are (a) 1 nm and 813 nm, (b) 1.5 nm and 704 nm, (c) 3 nm and 582 nm, (d) 6 nm and 495 nm, and (e) 17.5 nm and 437 nm. 75

Figure 4.8. (a) TEM image of AgNC@SiO₂ (43 nm / 3.5 nm). SEM images of (b) monolayer, (c) partial monolayer, and (d) multilayer of AgNC@SiO₂. Scale bars are (a)

20 nm and (b)-(d) 200 nm. 77

Figure 4.9. (a)-(c) Experimental and (d)-(f) calculated θ - λ_R maps for (a) and (d) AgNC (43 nm) with shell (0 nm), (b) and (e) AgNC (43 nm) with shell (3.5 nm), and (c) and (f) AgNC (43 nm) with shell (21.5 nm). The positions of dips on the experimental maps of (a)-(c) are marked with circular black dots at the same positions on the simulation maps of (d)-(f). The whole regions in the experimental maps are denoted by dotted boxes on the simulation maps. 78

Figure 4.10. For an environmental refractive index of 1.00 (air), (a)-(c) experimental and (d)-(f) calculated θ - λ_R maps for (a) and (d) AgNC (43 nm) with shell (0 nm), (b) and (e) AgNC (43 nm) with shell (3.5 nm), and (c) and (f) AgNC (43 nm) with shell (21.5 nm). The positions of dips on the experimental maps of (a)-(c) are marked with circular black dots at the same positions on the simulation maps of (d)-(f). The whole regions in the experimental maps are denoted by dotted boxes on the simulation maps. 79

Figure 4.11. (a) Gap distribution of AgNC@SiO₂ in sample. The average gap distance is 49.3 nm and standard deviation is 7.47 nm. (b) Randomly generated gap distribution with normality. (c) Simulation condition. One period includes one hundred of randomly distributed cubic units with normality. P , d , t , θ , and R are period, core diameter, shell thickness, incident angle, and reflectance. (d) Initial calculated, (e) experimental, and (f) recalculated θ - λ_R maps. Positions of dips on the experimental map in (e) are marked with yellow open circles at the same positions on simulation maps of (d) and (f). For environmental refractive index of 1.00 (air), (g) Initial calculated, (h) experimental, and (i) recalculated θ - λ_R maps. Positions of dips on the experimental map in (h) are marked with yellow open circles at the same positions on simulation maps of (g) and (i) 81

Chapter 1

Introduction

1.1. Introduction of plasmonics

Light and materials are indispensable to each other for their valuable properties to appear and be used in human society. They have not only passive relationship, which, namely, is that light propagates through medium materials and materials show their characteristic optical properties by light, but also active relationship, that they can transform each other in ways, such as photosynthesis and diffraction. Light and materials are long standing subjects which have been observed and studied since ancient times because human beings have always lived with them in nature.

Research of materials originated from ancient alchemy. The attempts of alchemists to clarify and anticipate the products of chemical reactions resulted in the establishment of early conceptions of chemical elements and rudimentary periodic tables [1, 2]. They learned how to extract metals from ores and how to compose many types of materials. Such practical applications of alchemy made contributions to a wide range of modern chemical and material sciences. In addition, various organic and inorganic materials, such as plastic, metal alloy, semiconductor, and liquid crystal, have played extremely important roles in the modern industry.

Recently, studies of nano-scale materials have drawn great attention with the appearance of nanotechnology since nano-materials were known to have properties distinguishable from those of bulk materials. Studies of light, on the other hand, trace

way back to the ancient times when transparent crystal was first used. Ancient people made various lenses and prisms by polishing crystals, and then developed geometrical optics with the primary instruments [3, 4]. Through the development of the geometrical optics, simple phenomena such as reflection and refraction could be explained, but the principles of interference and diffraction could not. Those principles then were clearly explained when the existence of electromagnetic waves was predicted by Maxwell's equations [5]. Classical optics has had a great impact on major industries, such as telecommunication, display, and medicine until now. Nanophotonics, the study of light on the nano-scale, is also a currently active and vibrant research field of nanotechnology.

Various approaches have been used in studying nanophotonics, such as photonic crystal, silicon photonics and plasmonics, in order to apply the distinguishing properties of nano-photonics to practical technology. Among them, plasmonics has a particular advantage of minimizing the volume and the response time of a device, resulting from the interaction between photons and electrons in the smallest scale of them. Surface plasmons are quasi-particles of free electrons collectively oscillated by external stimulation at interface between metal and dielectric materials [6-8]. Interestingly, SPs do not use transparent dielectric but metal as a medium, in contrast to other approaches for nanophotonics. For the reason of such differentiated properties, plasmonics has received great attention as one of the leading candidates in the core technology for next-generation devices, such as optical integrated circuit, optical memory and bio sensor chip.

1.2. Fundamental principles of surface plasmons

Surface plasmon is an optical phenomenon arising from the collective oscillation of free electrons at the interface between a metal and a dielectric when the electrons are disturbed from their equilibrium positions by light, in which the free electrons of a metal are driven by the alternating electric field to coherently oscillate at a resonant frequency. Surface plasmon is mainly categorized into two classes [6-10]. One is propagating surface plasmon (PSP) and the other is localized surface plasmon (LSP) as shown in

Figure 1.1. PSPs continuously propagate along flat surface of metal layer after excitation with prism or grating under a condition matching momentums of light and plasmon. Contrary to PSPs, LSPs go around only discontinuous metal nanostructure and their property is dependent on the size and shape of the structure.

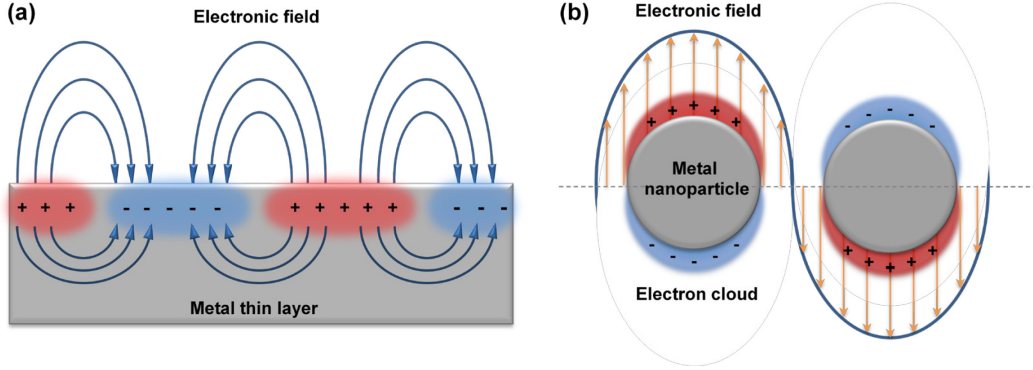


Figure 1.1. Schematic illustration of (a) propagating surface plasmons on a thin metal layer and (b) localized surface plasmons on metal nanoparticles [9].

In general, PSP can be characterized by the characteristic equation for a flat metal–dielectric structure or its dispersion relation, and it can be delivered from phase matching condition of Maxwell’s equations, as shown in equation below for a single interface structure [11, 12]:

$$\omega = c_0 k_x \sqrt{\frac{\epsilon_m + \epsilon_d}{\epsilon_m \epsilon_d}}, \quad (1.1)$$

where ω is the angular frequency of light or PSP, c_0 the speed of light in vacuum, k_x the propagation constant of PSP, and ϵ_m and ϵ_d correspond to electric permittivity (dielectric constant) of metal and dielectric, respectively. Since the surface plasmon is associated with an evanescent field, it can be excited by irradiation with an evanescent light wave

satisfying the dispersion relationship at the boundary between the metal and the dielectric [6-8]. Excitation of the surface plasmon can be performed with the evanescent field generated by total internal reflection, a fine grating, or any other subwavelength structure. Dispersion relations of air, a certain dielectric medium, and PSP are shown in Figure 1.2.

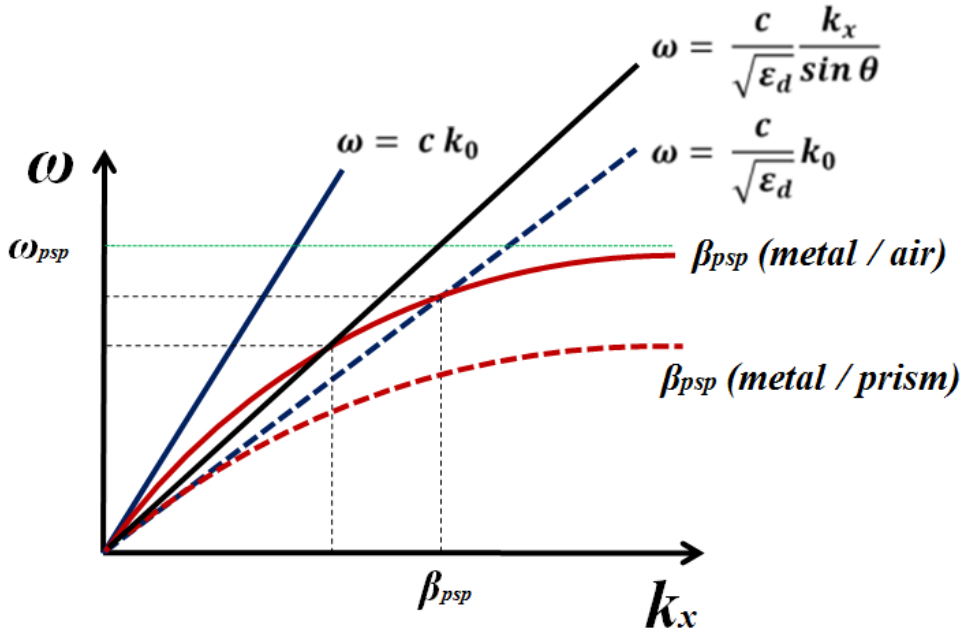


Figure 1.2. ω - k dispersion relationship of propagating surface plasmon.

Figure 1.3 shows a schematic illustration of the Kretschmann configuration and a plot of the reflectance as a function of the incidence angle. At the angle of surface plasmon resonance, incident photons excite the surface plasmons and the photon energy is transferred to the surface plasmon, resulting in a dip in the reflection curve. The sharpness of the dip depends on the ratio of the imaginary part to the real part of the dielectric constant of the metal. A sharp dip represents a strong resonance of the plasmon, or a high intensity of the field. If the dispersion relation is changed because of a change of the refractive index of an environment, the intersection with the light line will also change. Therefore the minimum in reflectance will occur at different light wavelength.

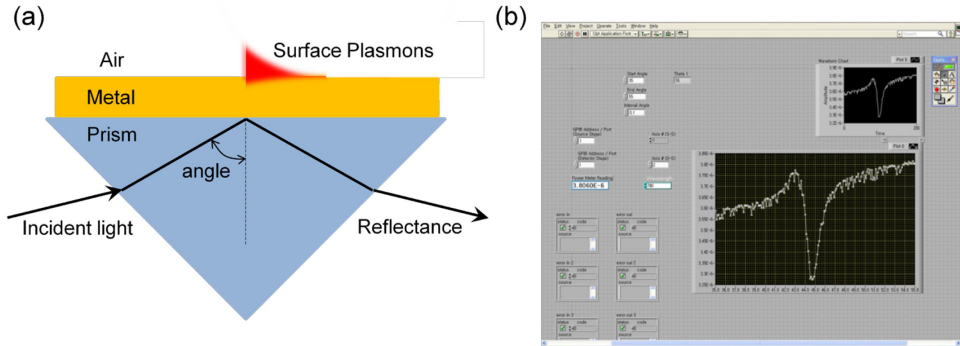


Figure 1.3. (a) The Kretschmann configuration. (b) Reflectance curve of a 50 nm thin silver layer as a function of incident angle. The minimum reflectance dip shifts toward a high incident angle as the refractive index of an environment increases.

Figure 1.1(b) shows LSPs which is the interaction between the electric field of incident light and the free electrons of a metal sphere whose size is smaller than the wavelength of light. The electric field can cause free electrons to move away from the metal particle in one direction, creating a dipole that can switch direction with the change in electric field. When the wavelength of the dipole plasmon is approximately the same as the incident light, a resonance condition is reached, leading to constructive interference and the strongest signal for the plasmon. For spherical nanoparticles of Au and Ag with diameters less than 30 nm, mainly dipole plasmon resonance is involved; however, for larger particles, quadrupole plasmon resonance from two negatively charged poles and two positively charged poles may be observed. The resonance wavelength and intensity of surface plasmons are determined primarily by the dielectric constant of materials, the shape or size of metal nanoparticle, polarization of incident light. This dependence offers the ability to tailor the LSP of metal nanoparticles through shape-controlled synthesis as shown in Figure 1.4 [13].

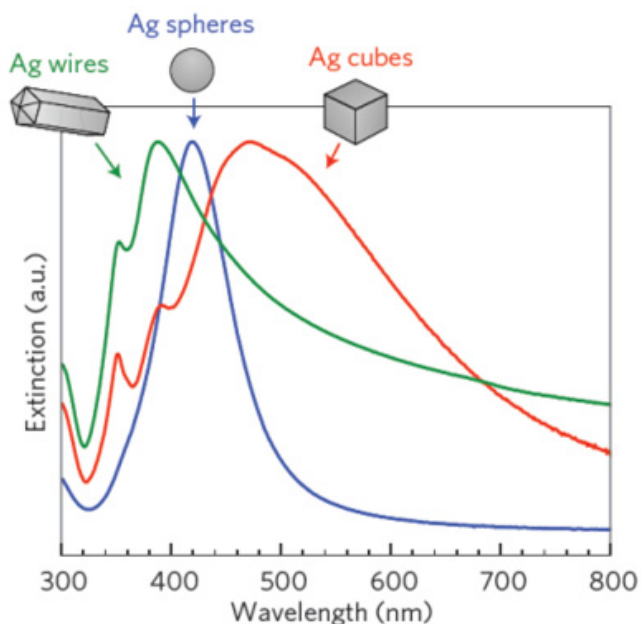


Figure 1.4. Normalized extinction spectra for Ag wire, cube and sphere nanoparticles. Wire-shaped particles have 90 ± 12 nm diameter and >30 aspect ratio, cubic particles have 79 ± 12 nm edge length and spherical particles have 38 ± 12 nm diameter [13].

When the particles go close to each other, the electromagnetic fields get comparable to the exciting field and the particles become electromagnetically coupled. The effect of an inter-particle distance on surface plasmons can be considered in a simple case for only two interacting nanoparticles. To gain qualitative insight, the particle pair can be described as two interacting dipolar oscillators. For parallel polarization, the near field of one particle dipole acting on another points to the same direction, whereas for polarization perpendicular to the pair axis, it points to the opposite direction as shown in Figure 1.5 [14-16]. Thus, if both particles are excited together, the dipole field weakens the exciting field at the position of the other particle in perpendicular polarization of light, while it strengthens the exciting field in parallel polarization of light. In analogy to

coupled harmonic oscillators, one therefore expects a shift of the resonance to shorter wavelengths for perpendicular polarization and to longer wavelengths for parallel polarization. Figure 1.6 shows that the degenerate modes of the two identical nanoparticles split up and shift to the red or the blue depending on the polarization of the exciting light [17].

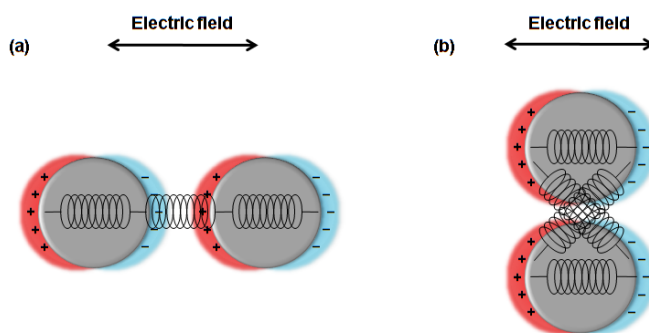


Figure 1.5. Two configurations of a pair of metal nanoparticles with respect to the polarization of the incident light. The dotted lines notify the induced electric field lines of the polarized particle.

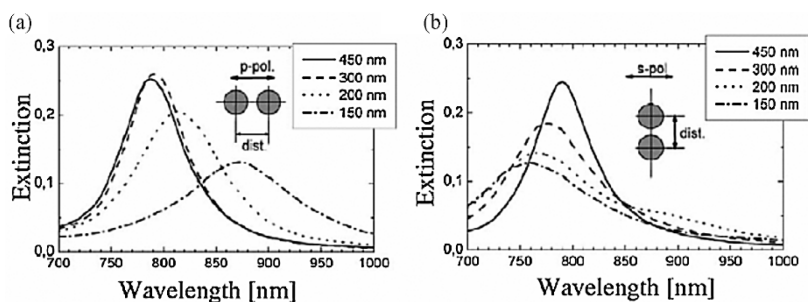


Figure 1.6. Experimental extinction spectra of arrays of particle pairs for polarization (a) parallel and (b) perpendicular to the pair axis. The particle has a diameter of 150 nm and a height of 14 nm [17].

1.3. Motivation of this dissertation

In the Middle Ages in Europe, glassmakers unwittingly took advantage of plasmon effects when they created colorful stained-glass windows that incorporated small metal particles in the glass. One of the first known, and most famous, uses of surface plasmons is a Roman glass work dating from the Byzantine Empire in the 4th century AD - the Lycurgus Cup [18]. While the cup appears green under normal lighting, it becomes vibrant red color when illuminated from within. It is the metal nanoparticles embedded in the dielectric of the cup that is important to the color. Although the plasmonic properties were naturally found from the LSP of metal particles, most scientists investigated surface plasmon using a simple model of the boundary between metal and dielectric materials in order to search out the physics of surface plasmon. As a result, Kretschmann and Otto recognized that a prism could be used to increase the momentum of the excitation photons, in order to excite PSP at a thin metallic layer on the prism [19, 20]. In both experiments, the presence of PSP is confirmed by a drastic dip in the intensity of the far-field reflected light observed as the angle of incidence is scanned, for p -polarized light. Due to its relative ease of construction, the so-called Kretschmann configuration became a useful tool for the investigation of fundamental plasmon kinetics, and served as a good platform for SPR biomolecular detectors.

Since surface plasmons have two different properties, PSP and LSP, it would seem that research on surface plasmons has been separated largely into two approaches. Physicists and electronic engineers have tried to discover new kinetics of surface plasmon and design plasmonic devices in order to realize plasmonic integrated circuits, which are mainly included in the PSP category. Chemist and materials engineers have tried to synthesize new functional materials and fabricate optimal nanostructures in order to apply plasmonic properties to medicine and bio sensor, mostly included in the LSP category. Although both research approaches have produced satisfactory results, attempts to explore a boundary or the common region between PSP and LSP can generate a significant synergy effect in plasmonics. I also have a great interest in the collaboration

between photonics and materials science to study the surface plasmons. It is assumed that this interdisciplinary research will be helpful to understand the kinetics of surface plasmons and design their optimized nanostructure, considering the indispensability of light and materials to each other.

In this paper, therefore, I intend to focus on metal nanoparticle arrays. They have advantages in two standpoints as follow. First, they can be supposed as elemental units which construct a certain plasmonic metal structure as molecules compose materials. Plasmonic properties were initially found from the mixture form of metal and dielectric nanoparticles in nature, which have been used without conscious awareness to various products until now. Second, they can be controlled in component materials, size and shape with a bottom-up approach, which is mostly included in chemistry and materials science. Surface plasmons at metal nanoparticles are also minutely controlled because the plasmonic properties are sensitive to the size and shape of the particles. Therefore, metal nanoparticles can be not only a start point to explore the common region between the PSP on a flat metal layer and the LSP on the metal particles, but also a link point to combine photonics with materials science. Array structures of metal nanoparticles, in particular, can be an amplifier to enhance the weak plasmonic intensity of a nanoparticle as well as an excellent tuner to minutely change plasmonic signals, as a result of a coupling effect in the periodic structure [16, 17]. The plasmonic coupling effect can be a useful tool to analyze various plasmonic properties depending on different structural parameters of the array. Studies on the plasmonic properties of the similar structures, which are a single [21], random [22, 23], and periodic array [24-26] of metal particles on a thin metal film, have been conducted. When the structures are exposed to light, they cause the plasmonic properties, such as a strong shift of the plasmon resonance, multi-peaks in the extinction spectra, an enhanced transmission, and a wide absorption band. Those phenomena can be explained as resulting from image-like interactions with the metal surface and, more importantly, through hybridization between the nanoparticle plasmons and the delocalized surface plasmons of the metal layer. However, because they focused on only a normal transmittance or reflectance properties when an incident light illuminates normally on the surface of the structures, it needs further research on the

relation of the LSP and PSP in the momentum matching condition. In particular, an investigation on the incident angle-dependent properties can provide important information to be utilized in practical applications.

Based on the above facts, I expect that an unexplored boundary region between PSP and LSP can come out open through the suggested interdisciplinary study of photonics and materials science. Last but not least, this research will serve as a bridgehead for a synergistic effect on a basic study of plasmonics.

1.4. Scope and organization

This dissertation focuses on the distributed structures of metallic nanoparticles and their plasmonic states. The research is divided into three categories: surface plasmon of metal nanoparticle in trench, plasmonic mixed states of core-shell nanocube arrays on a metal layer, and plasmonic intermediate states on a self-assembled monolayer of core-shell nanocubes.

This dissertation is organized as follows. Chapter 1 introduces plasmonics and explains the fundamental principles to be used in this research, and then presents motivation, scope, and organization of this dissertation.

Chapter 2 covers site-selective synthesis and surface plasmon of silver nanoparticle array in trench. In this chapter, the fundamental principle of metal nanoparticle synthesis is briefly reviewed and then a new chemical method, with which both synthesis and array can be conducted at a time, is proposed. This approach in this paper is defined as "site-selective synthesis" of silver nanoparticles in trench. After the explanation of the concept, principle, experimental procedure, and detailed results of this new means, the plasmonic properties of silver nanoparticle array are analyzed with the optical results measured using the Kretschmann configuration.

In Chapter 3, plasmonic mixed states of a core-shell nanocube array on thin metal layers is discussed. In this chapter, the conceptual structure for investigating the plasmonic mixed state of PSP on thin metal layers, and LSP in the gap between metal

nanocubes and thin metal layers is proposed. I trace changes of the minimum reflective bands on an incident angle-wavelength map in various structural parameters, such as period, core size, shell thickness and layer thickness, based on a simulation tool called the Rigorous Coupled Wave Analysis (RCWA). Then, synthesis of silver nanocubes with silicon dioxide shell and their optical measurement are conducted in order to confirm it in experiment. The Weibull distribution is introduced with statistics for the recalculation of the proposed structure so as to check the effect of the inter-particle distance distribution on the band. In addition, the possibility of detecting surface plasmon resonance signals and fluorescence images at the same time is experimentally demonstrated.

Chapter 4 covers a plasmonic intermediate state between PSP and LSP on self-assembled monolayers of silver nanocubes with silicon dioxide shell (AgNC@SiO_2). In this chapter, a structure is suggested to find the intermediate state in a narrow window of the distance between silver nanocubes. The RCWA simulation data show distinguishable properties, such as two minimum reflectance bands, transitions between PSP and LSP, and rapid change of the plasmonic state at crosspoint. The validity of the proposed concept is confirmed by comparing experimental data with the results of the statistical recalculation. Different kinds of plasmonic states are investigated in Chapters 3 and 4. First, in the structure of the periodically distributed AgNC@SiO_2 on an Ag layer, the propagating surface plasmon on the Ag layer can be partially localized at the SiO_2 gap between the AgNC and Ag layer. As a result, the plasmonic state is changed from PSP to the mixed state of PSP and LSP as the inter-particle distance decreases or the population density of the particles increases. On the other hand, plasmonic intermediate states can be found in the monolayer of AgNC@SiO_2 . The transition between PSP and LSP occurs in a narrow region of the inter-particle gaps while PSP and LSP are excited on a continuously contacted and completely separated AgNC , respectively.

Finally, concluding remarks for this dissertation are provided in Chapter 5.

Chapter 2

Site-selective synthesis of silver nanoparticles in a trench and their surface plasmons

Metal nanoparticles have been widely studied in the burgeoning fields of nano-science and technology because of their unique properties, which include a large surface area per unit volume, high electrical conductivity, and their surface plasmon properties [27, 28]. In order to exploit the beneficial properties of nano-sized metal particles, many research groups have examined the use of metal nanoparticles in combination with various practical devices, such as highly efficient solar cells [29-32], three-dimensional color holography [33, 34], and compact bio-sensors [35-37]. Particular attention has been paid to the synthesis and arrangement of metal nanoparticles. These two techniques facilitate the versatile utilization of surface plasmon [38-42]. Various synthetic techniques have been developed for producing size- and shape-controlled metal nanoparticles [41-44], and a number of reliable methods have also been developed for producing metal nanoparticle arrays through diverse top-down and bottom-up processes [45-48].

However, studies of synthesis and arraying metal nanoparticles have so far been conducted separately, not in an integrated manner, by different research groups. The fact of the matter is that the synthesis of metal nanoparticles in precisely pre-designed shapes and sizes is not an easy task, and it is even more difficult to arrange the nanoparticles in a targeted pattern. Furthermore, in terms of product quality and process cost, performing the synthesis and arrangement in two sequential steps is inefficient. It is a particularly

significant challenge to develop a convenient method for synthesizing and arranging metal nanoparticles precisely in pre-designed structures, such as grooves or trenches, which would be very useful in the field of optics, because the light field can be confined in and propagate along these structures [49].

In order to solve these problems, I propose a new method for simultaneously synthesizing and locating metal nanoparticles in a pre-patterned trench. I refer to the proposed method as the "site-selective synthesis" of metal nanoparticles. The results supporting a detailed mechanism and the plasmonic properties are deeply progressed and reported in this paper. Using this method, I am able to prepare Ag nanoparticles in controlled sizes in a very narrow trench to demonstrate the feasibility of the process. The plasmonic properties of the sample were examined by measuring the intensity of light scattered from Ag nanoparticles. I analyzed their LSP characteristics both in the far- and near-field regimes. The results showed that the fabricated structure is capable of robustly reradiating electromagnetic fields at larger angles than the critical angle of the total internal reflection (TIR).

2.1. Concept: site-selective synthesis of Ag nanoparticles in a trench

I hypothesized that, if it were possible to selectively create nucleation sites in a trench, then it should be possible to selectively synthesize Ag nanoparticles on the nucleation sites, as illustrated in Figure 2.1, which shows a scheme for the site-selective synthesis of Ag nanoparticles in a pre-patterned trench through solution chemistry. The main mechanism of the site-selective synthesis can be explained by i) the selective attraction of Ag^+ ions to the hydrophilic PVP/silica trench and the repulsion of Ag^+ ions away from the hydrophobic fluorosilane layer [60-63], and ii) the selective nucleation of Ag nanoparticles on the PVP domains in the PVP/silica layer as the result of chemical interactions between Ag^+ ions and PVP [52-59]. Hence, Ag nanoparticles can be

selectively nucleated and grown on the PVP domains in the trench. Namely, the hydrophilic nature of the PVP/silica trench enables the chemical reactant to selectively approach the trench and the PVP domains in the PVP/silica trench, which contains nucleation sites for the formation of Ag nanoparticles. These dual functions of the PVP domains in the PVP/silica layer will be crucial in selectively depositing Ag nanoparticles in the trench.

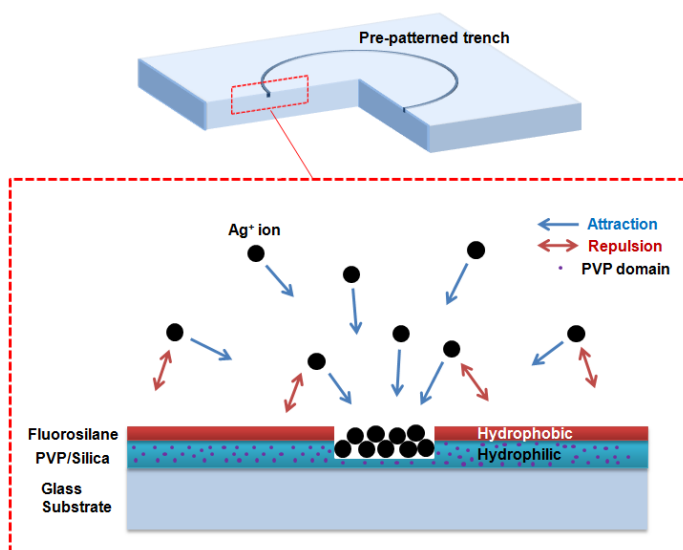


Figure 2.1. Schematic illustration of the mechanism for the site-selective synthesis of Ag nanoparticles in a trench.

2.2. Chemical fabrication

2.2.1. Experiment

Preparation of a hydrophilic substrate: A glass wafer with a thickness of 1 mm was used as the substrate for measuring the transmission image. The wafer was cut into

rectangular shaped pieces with dimensions of 20 mm x 10 mm, and then immersed in a mixture of sulfuric acid and hydro peroxide (volume ratio 1:1) at 100°C for 1 h in order to remove impurities and to create a hydrophilic surface. The chemicals remaining on the surface were removed by sonication and the wafer pieces were rinsed with deionized water. Finally, they were blown dry in a stream of nitrogen gas and dried at 120°C in a convection oven for 1 h.

Preparation of chemicals for surface treatment: Two types of chemical solutions, a polyvinylpyrrolidone (PVP)/silica solution and a fluorosilane solution, were prepared in order to create, respectively, hydrophilic and hydrophobic surfaces on the cleaned wafer. The PVP/silica solution, was prepared by mixing PVP and a silica sol solution at various weight ratios. The PVP solution was prepared by dissolving PVP (0.3 g, average mol wt 10,000, Sigma-Aldrich) in ethanol (10 mL, J. T. Baker, $\geq 98\%$). The silica sol solution was prepared using a sol-gel process. Tetraethoxysilane (TEOS; 1 g, Sigma-Aldrich, $\geq 99\%$) and ethanol (10 mL) were stirred in a vial that was maintained at a temperature of 30°C in oil bath. After 5 min, nitric acid (0.6 mg) was rapidly injected into the mixture, which was then stirred at the same temperature for 20 h. The fluorosilane solution, a second chemical, was EGC-1720 obtained from Novec, 3M.

Chemical coating and FIB milling: The wafer was spin coated with the PVP/silica solution at 6000 rpm for 1 min and dried at 100°C for 2 min. In the case of the fluorosilane solution, the same coating process with a spin speed of 3000 rpm, was sequentially repeated on the same sample. After the baking the sample at 100°C for 1 h to harden each layer, all of the fluorosilane and part of the PVP/silica in a trench were milled by a means of a focused ion beam (FIB; Quanta 200 3D, FEI) at 30 keV and 0.8 pA. Three trench shapes, rectangular, triangular, and circular, were patterned on the chemically treated surface of the sample. The length (or diameter), width, and depth of the trenches were 10 μm , 100 nm, and 100 nm, respectively.

Site-selective synthesis of Ag nanoparticles: Silver was selected as the metal because it has high electrical and thermal conductivities which are suitable for applications to various practical electronic or optic devices. Butylamine was used as the reducing agent because the amine group plays an important role as a mild reducing agent to produce Ag nanoparticles at a low temperature [51]. PVP was used as a typical stabilizer which prevents particle aggregation and controls the average size of Ag nanoparticles [52-59]. The sample was fixed inside the wall of a vial with a clip. In the case of Ag nanoparticles with average diameter of ca. 47 nm, silver nitrate (2 mg), PVP (1 mg), and ethanol (20 mL) were mixed with a magnetic stirring bar for 2 min. Butylamine (1 mg) was quickly injected into the vial and the solution heated to 70°C and the completion of the synthesis reaction required from 5 to 20 min depending on the size of Ag nanoparticles. After the reaction, the sample was washed exhaustively with ethanol to remove the reactive solution and the sample was dried at 80°C. Above all procedure is shown in Figure 2.2.

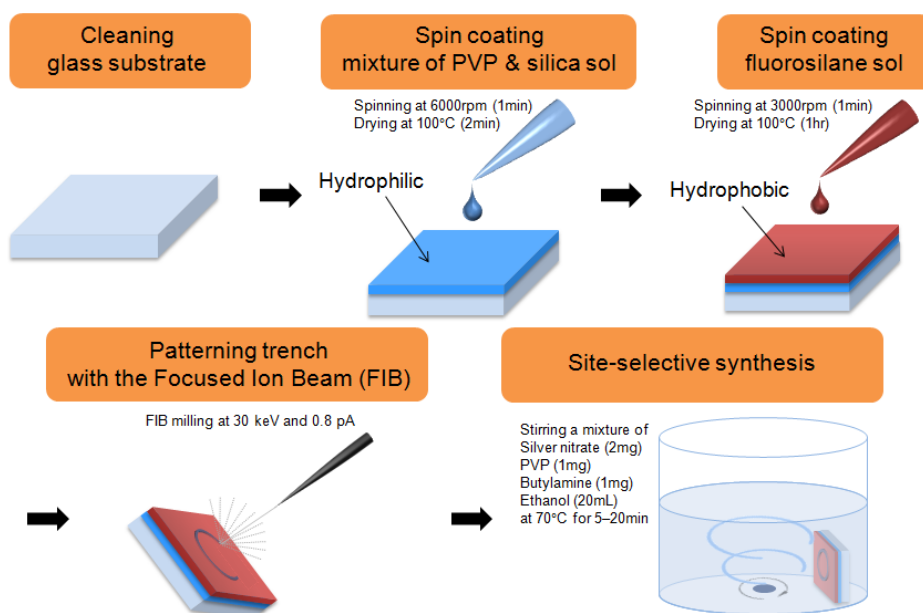


Figure 2.2. Schematic procedure of site-selective synthesis of silver nanoparticles in trench.

2.2.2. Results and discussion

Based on this concept, I explored the practical roles of the PVP domains and the fluorosilane layer in the site-selective synthesis of Ag nanoparticles. As documented in the experimental section, I coated two thin layers of PVP/silica and fluorosilane on a silicon wafer, and then examined the surface energy and the cross-sectional morphology of each layer.

The cross-sectional morphologies of the PVP/silica layer and the fluorosilane layer were examined by the field emission scanning electron microscopy (FE-SEM) as shown in Figure 2.3. Very interestingly, the PVP domains were homogeneously distributed in the form of ca. 10 nm-sized islands in the PVP/silica layer with a thickness of ca. 200 nm. In addition, the population of islands increased with increasing concentration of PVP in the PVP/silica solution (Figures 2.3(a)-(c)). This clearly explains why Ag nanoparticles are selectively formed only in the pre-designed PVP/silica trench because the PVP island domains are involved in chemical interactions with Ag^+ ions and consequently direct the growth of Ag nanoparticles specially to the PVP domains. However, it is not categorically assumed that increasing the concentration of PVP in the PVP/silica solution can raise the selectivity for synthesizing Ag nanoparticles in the trench. An excess of PVP, higher than the ratio in Figure 2.3(c), causes phase separation and fracturing between PVP and silica in the layer. Therefore, I used PVP/silica mixture in the ratio shown in Figure 2.3(c) for the site-selective synthesis of Ag nanoparticles. On the other hand, to provide a better demonstration of the formation of fluorosilane layer, I coated it on a silicon wafer, because the fluorosilane layer does not reveal sufficient contrast when formed on a PVP/silica layer. Figure 2.3(d) confirms the formation of a ca. 10 nm-thick-fluorosilane layer on the silicon wafer, of which the thickness is consistent with the manufacturer's specifications (3M datasheet) [65].

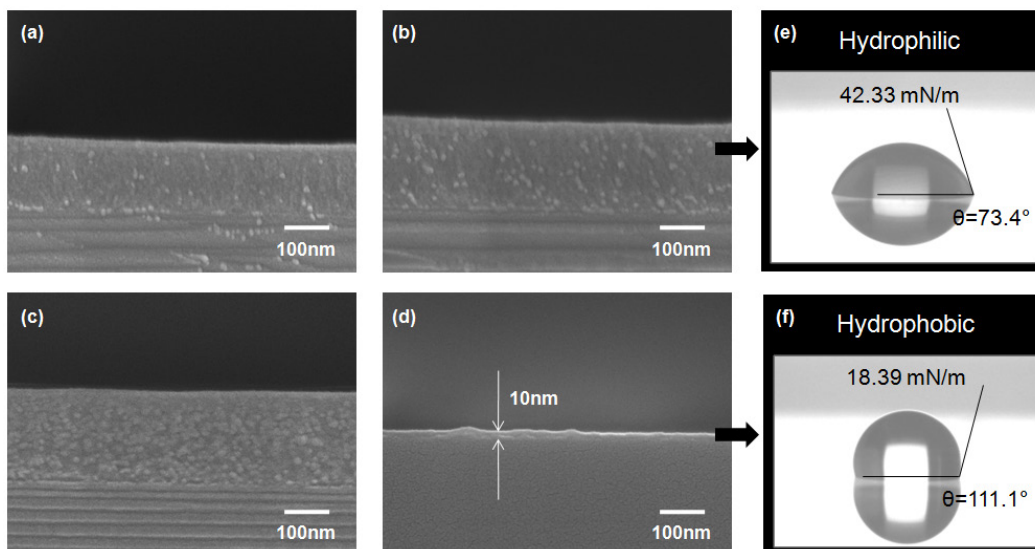


Figure 2.3. SEM images of cross-sectional morphologies of (a)-(c) the PVP/silica layers and (d) the fluorosilane layer on a silicon wafer. The PVP/silica layers were prepared by mixing in ratios of PVP solution and silica sol solution as (a) 1:3, (b) 2:2, and (c) 3:1. The PVP domains are homogeneously distributed in the form of islands with diameters of ca. 10 nm. The thicknesses of the PVP/silica layer and fluorosilane layer are ca. 200 nm and ca. 10 nm. The striped region under the mixed layer is fragments of silicon wafer which occur naturally and horizontally when they are broken to determine the cross-section. Each scale bar is 100 nm. CCD images of a water droplet on (e) PVP/silica and (f) fluorosilane layer. The contact angle between the two black lines and the surface energies are indicated in the images.

Figures 2.3(e) and (f) show the contact angle for each layer confirming that the PVP/silica layer is hydrophilic while the fluorosilane layer is hydrophobic. From the contact angles of a water droplet and a diiodomethane droplet on the surface of each layer, it is possible to calculate the surface energies of the PVP/silica layer (42.33 mN/m) and the fluorosilane layer (18.39 mN/m) using the Owens-Wendt-Rabel-Kaelble approximation [64]. These values imply that the PVP/silica layer enables the Ag precursor solution to be more easily wetted than the fluorosilane layer because of the high surface energy of the PVP/silica layer. The hydrophilic PVP/silica layer could allow the Ag precursor solution to access the pre-designed trench. It should be noted that Ag nanoparticles are grown only on the PVP/silica trench because of the chemical attraction between Ag^+ ions and PVP domains. In contrast, no Ag nanoparticles were deposited on the fluorosilane layer because of the low surface energy. This clearly indicates that the PVP domains and the fluorosilane play critical roles in the selective formation of Ag nanoparticles in the PVP/silica trench.

In order to succeed in the site-selective synthesis of Ag nanoparticles in a pre-designed pattern, the population density of PVP domains and accurate milling of fluorosilane layer must be carefully controlled. The population density of the PVP island domains in the PVP/silica layer should be sufficient to guarantee the homogeneous nucleation and growth of Ag nanoparticles in the trench because the insufficient PVP domains in the PVP/silica layer cannot provide enough nucleation sites for Ag nanoparticles so that they cause the sparse distribution of Ag nanoparticles in the trench (Figures 2.4(a), (c), and (d)). In addition, only the fluorosilane on the target shape should be precisely milled by the focused ion beam (FIB) because the nucleation of Ag nanoparticles occurs wherever fluorosilane is broken off. Figures 2.4(b), (e), and (f) show that an excess synthesis of Ag nanoparticles near the trench may occur. In addition, the structural quality of real trenches can be observed in SEM images of Figures 2.4(g)-(i). The trenches with both width and depth of 100 nm, 200 nm, and 300 nm were milled by FIB at 30 keV and 0.8 pA, and their top views are measured with FE-SEM. Because the edges of rectangular trenches are expressed as the bright portions in the SEM images, the high contrast and clarity of the boundary lines imply the sharpness of the trench edges.

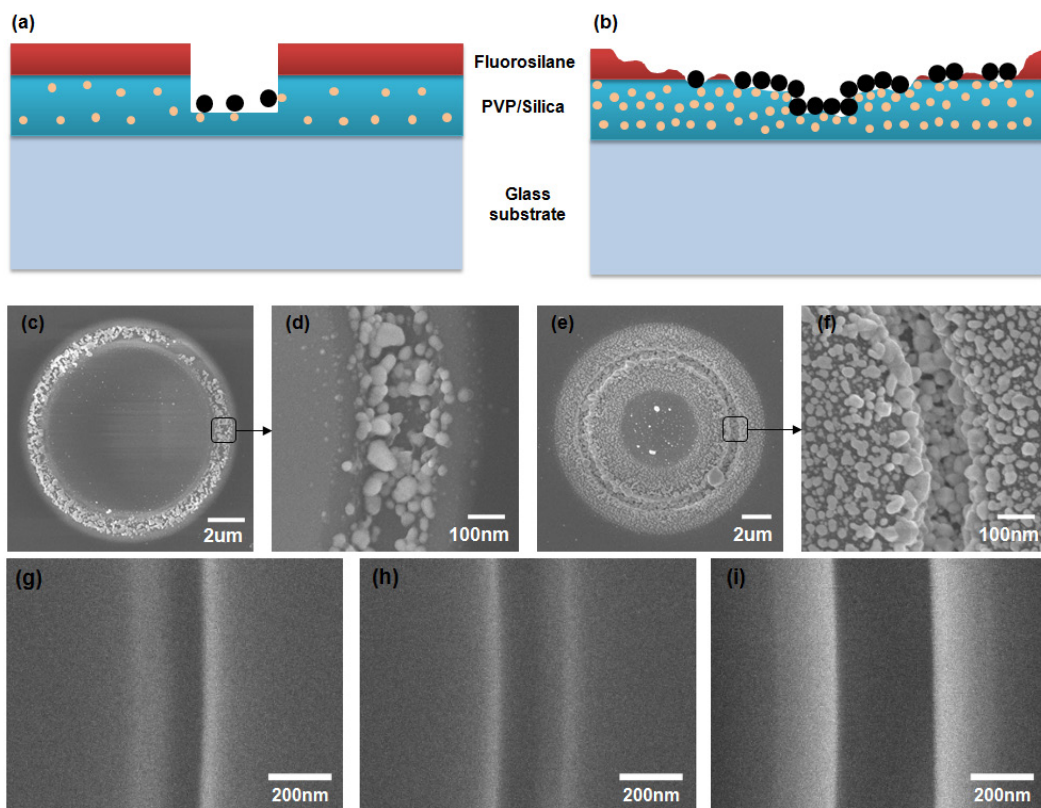


Figure 2.4. Schematic illustrations of circular shaped trenches packed with Ag nanoparticles: (a) sparse coverage, due to insufficient PVP island domains in the PVP/silica layer and (b) over-dense coverage, due to the over-exposure of the fluorine layer by FIB. (c)-(f) SEM images for each case. (g)-(i) SEM images of vacant trenches with three different widths and depths of (g) 100 nm, (h) 200 nm, and (i) 300 nm. The scale bars are (c) and (e) 2 μm , (d) and (f) 100 nm, and (g)-(i) 200 nm.

The verticality and sharpness of the rectangular trench increase as both width and depth increase. The structural property can affect optical properties such as geometrical scattering of trench. Consequently, Ag nanoparticles can be formed in exact patterns with regular sizes when the trench is precisely tailored by FIB and has sufficient homogeneous PVP island domains.

In order to demonstrate the versatility of the newly proposed site-selective synthesis of Ag nanoparticles in the pre-patterned trenches, I synthesized Ag nanoparticles in pre-patterned trenches with circular, rectangular, and triangular shapes with 100 nm depths, 100 nm widths, and 10 μm lengths (or diameters) as shown in Figure 2.5. Here, I choose these three different pre-designed shapes as model patterns because these shapes are the basic geometries for forming various complex patterns. Figures 2.5(a)-(c) clearly show that Ag nanoparticles can be selectively nucleated in the pre-designed patterns through the proposed scheme and the narrow trench successfully directs the growth of Ag nanoparticles to the pattern, even though the shapes of the trenches are artificial. Typical magnified SEM image for Ag nanoparticles in the trench are shown in Figure 2.5(d) to check the size and morphology of the Ag nanoparticles. This confirms that Ag nanoparticles in sizes of ca. 47 ± 12 nm are selectively deposited on the trench. In addition, this structure prepared using the proposed method has excellent physical stability. The nanoparticles in the trench are resistant to external stimulation, for example, sonication, a process frequently used for cleaning. I presume that the PVP-Ag⁺ ion complexes are formed in the nucleation and the initial growth processes, and the PVP that covers Ag nanoparticles may then become entangled with the excess of PVP domains in the trench and increase the adhesion to the PVP/silica layer of the trench during clustering [54, 57, 66].

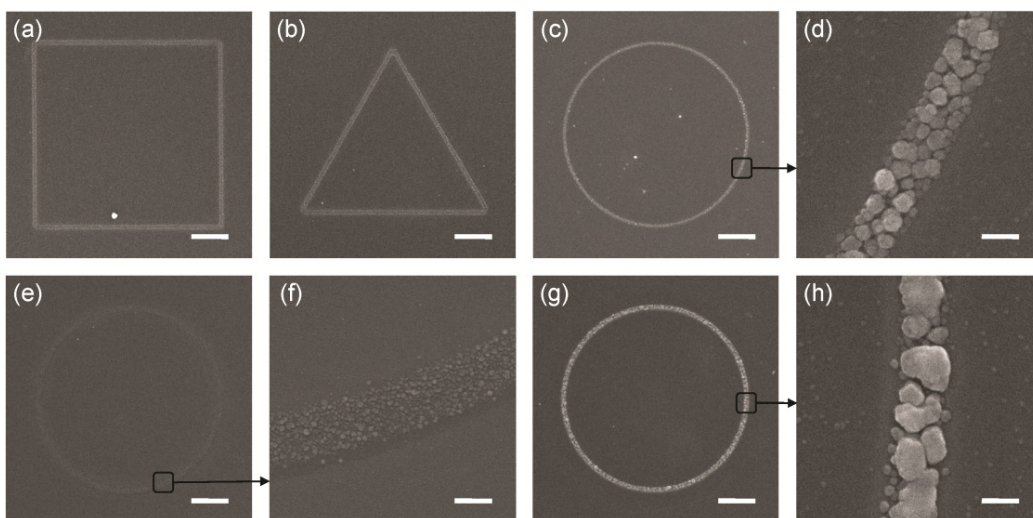


Figure 2.5. SEM images of Ag nanoparticle-clusters in (a) rectangular, (b) triangular, and (c)-(h) circular trenches as results of the site-selective synthesis. Width, depth, and length (or diameter) of each trench are 100 nm, 100 nm, and 10 μm , respectively. There are Ag nanoparticles with three different kinds of sizes in the same dimension. The Ag nanoparticle sizes are (a)-(d) 47 ± 12 nm, (e) and (f) 17 ± 8 nm, (g) and (h) bimodal distribution of 28 ± 9 nm and 94 ± 43 nm approximately. (d), (f), and (h) are magnified images of black boxes in (c), (e), and (g), respectively. The scale bars of (d), (f), and (h) are 100 nm and others are 2 μm .

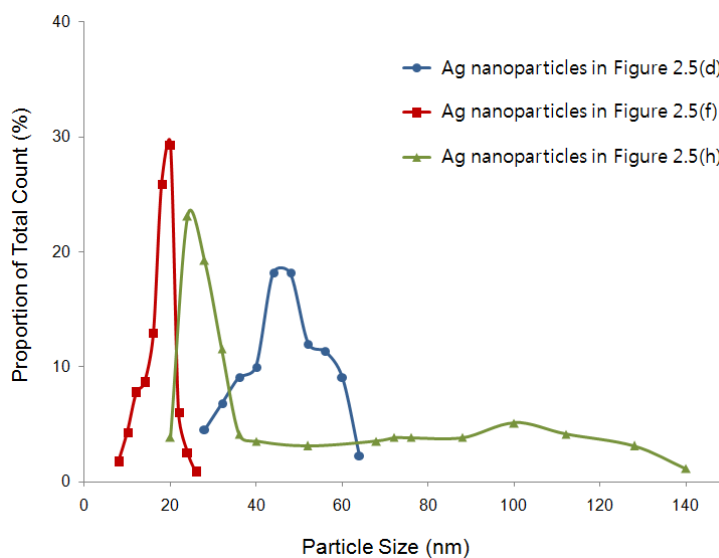


Figure 2.6. Average size and size distributions of Ag nanoparticles in Figures 2.5(d), (f), and (h), which were counted from SEM images. The average sizes are approximately 47 ± 12 nm (Figure 2.5(d)), 17 ± 8 nm (Figure 2.5(f)), and bimodal distribution of 28 ± 9 nm and 94 ± 43 nm (Figure 2.5(h)). The lines are drawn as a guide.

Another important issue for the versatility of the site-selective synthesis is to be able to control the size of Ag nanoparticles in a trench because LSP is strongly dependent on the size of Ag nanoparticles. It could be controllable by changing the conditions such as the amount of ingredient chemicals, the temperature, and time for the synthesis reaction. Figures 2.5(c)-(h) show three different size distributions of Ag nanoparticles synthesized using different amounts of silver nitride and butylamine. The average sizes and the distributions were measured from the SEM images of Figures 2.5(d), (f), and (h) and the detailed results are shown in Figure 2.6. They are approximately 47 ± 12 nm (Figures 2.5(c) and (d)), 17 ± 8 nm (Figures 2.5(e) and (f)), and have a bimodal distribution of 28 ± 9 nm and 94 ± 43 nm (Figures 2.5(g) and (h)), which are roughly consistent with the changes in the amounts of starting materials used. The input amounts of silver nitride, butylamine, and PVP were 0.7 mg, 0.35 mg, and 0.35 mg in Figures 2.5(e) and (f), 2 mg,

1 mg, and 1 mg in Figures 2.5(c) and (d), and 4 mg, 2 mg, and 2 mg in Figures 2.5(g) and (h). Considering the uniformity in particle size, an obtainable maximum size exists, which is limited by geometrical factors, such as the width or depth of the trench as shown in Figure 2.5(h). This can be inferred from the SEM image of Figure 2.5(h) and the size distribution. When Ag nanoparticles grow larger than the limit, the irregularity in their shapes and sizes tends to increase because grown nanoparticles combine with one another, resulting in the formation of large particles.

2.3. Optical measurement

2.3.1. Experiment

The surface and the cross-sectional morphologies of the samples were examined by field emission scanning electron microscopy (FE-SEM; JSM 6700F, JEOL) and surface energies were measured with the contact angle analyzer (DSA100, KRUSS). Optical far-field images were measured using a modified optical microscopy setup that contained a charge-coupled device (CCD) camera (XCD-SX90CR, Sony) and an objective lens with a magnification of 100 and a numerical aperture of 0.8 (LMPlanFLN, OLYMPUS Corp.). The samples were illuminated from the bottom through a fused silica hemicylindrical prism (refractive index = 1.46) at 660 nm with a laser diode module (LQA660-110C, Newport) with the incident angle from 34° to 70°. The brightness of CCD pixels were calibrated by an optical power meter (1830-C, Newport). The linear relation between two types of data can be found in the dotted box of Figure 2.7. The reference source was a halogen lamp emitting white light. The electromagnetic field intensities and profiles in the near-field of the samples were measured using a near-field scanning optical microscope (NSOM; Multiview 4000, Nanonics).

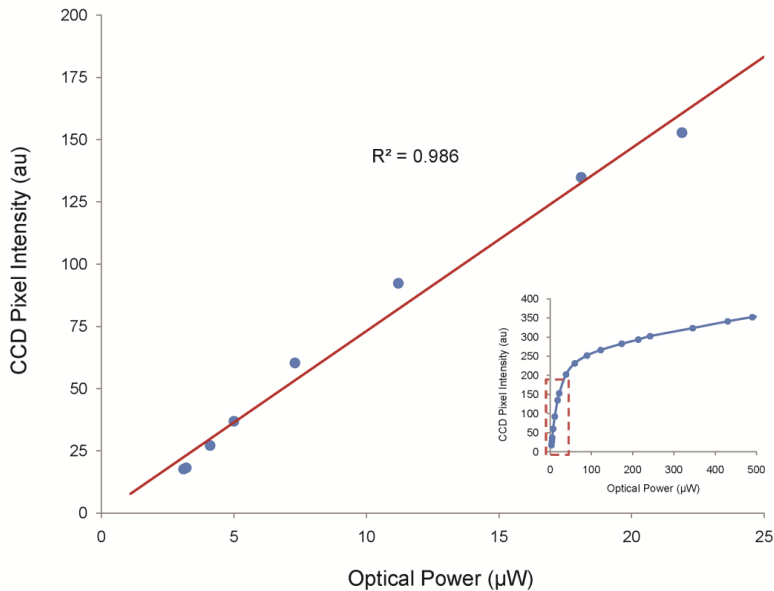


Figure 2.7. Graph showing the relationship between the intensity of CCD pixels and optical power. All scattering intensities measured in the far-field are included in the range from 0 to 25 μW . The extrapolated line of data in the red dotted frame of the inset is shown as a red line.

2.3.2. Results and discussion

The synthesized metal nanoparticle patterns exhibit useful plasmonic features. To illustrate the plasmonic characteristics of ca. 47 ± 12 nm Ag nanoparticles in a pre-patterned trench, I observed the polarization-dependent and incident angle-dependent response of a rectangular trench with and without Ag nanoparticles in the far-field. This measurement is a general method for demonstrating plasmonic properties because surface plasmon excitation shows different responses according to the polarization and the incident angle of light [67]. Figure 2.8 shows an illustration of the microscope set-up

and the terminology for the direction of a trench and the polarization of incident light. The dark field images of the samples were obtained with a CCD camera at several incident angles using 660 nm laser diode light source in the TIR geometry as shown in Figure 2.8(a). I chose a 660 nm laser diode as an excitation light source in order to determine the LSP effect because I observed that the color of light scattering from the sample was yellowish red in a dark field under a white light source in optical microscopy (Figure 2.9(d)). Although the LSP peak for the dispersed Ag nanoparticles in solution is in the range from 400 to 500 nm, the peak tends to shift toward longer wavelength when clusters are formed [68, 69]. Therefore I presume that LSP can be excited on Ag nanoparticle clusters in the trench at 660 nm although it may not be the exact maximum for the LSP peak. The samples were illuminated by either transverse electric (TE) or transverse magnetic (TM) polarized light obliquely incident through a fused silica hemicylindrical prism (refractive index = 1.46) with the incident angle being changed from 34° to 70°. For a better explanation, I used *x*- and *y*-trenches as terminologies to indicate the *x*- or *y*-directional sides of the rectangular shape, as depicted in Figure 2.8(b). Note that the incident light has no *y*-directional momentum in Figure 2.8 and the direction of the momentum projected onto the sample plane is parallel to the *x*-direction, as depicted with arrows in Figures 2.9(b), (c), (e), and (f). As a preliminary test, I present the dark field images (Figures 2.9(a) and (d)) obtained from incident unpolarized white light, a halogen source, which has an unspecific momentum. These findings verify that the light intensity scattered from Ag nanoparticles in the trench is enhanced (Figure 2.9(d)), compared with that from a vacant trench (Figure 2.9(a)). To provide further insights, the dependencies of scattering light on the incidence angle and the polarization of the incident light are shown in Figures 2.9(b), (c), (e), and (f). The dark field images obtained from the sample without Ag nanoparticles are shown in Figures 2.9(a)-(c) as a reference in order to comparatively analyze the plasmonic effects of Ag nanoparticles in the specified light (Figures 2.9(d)-(f)).

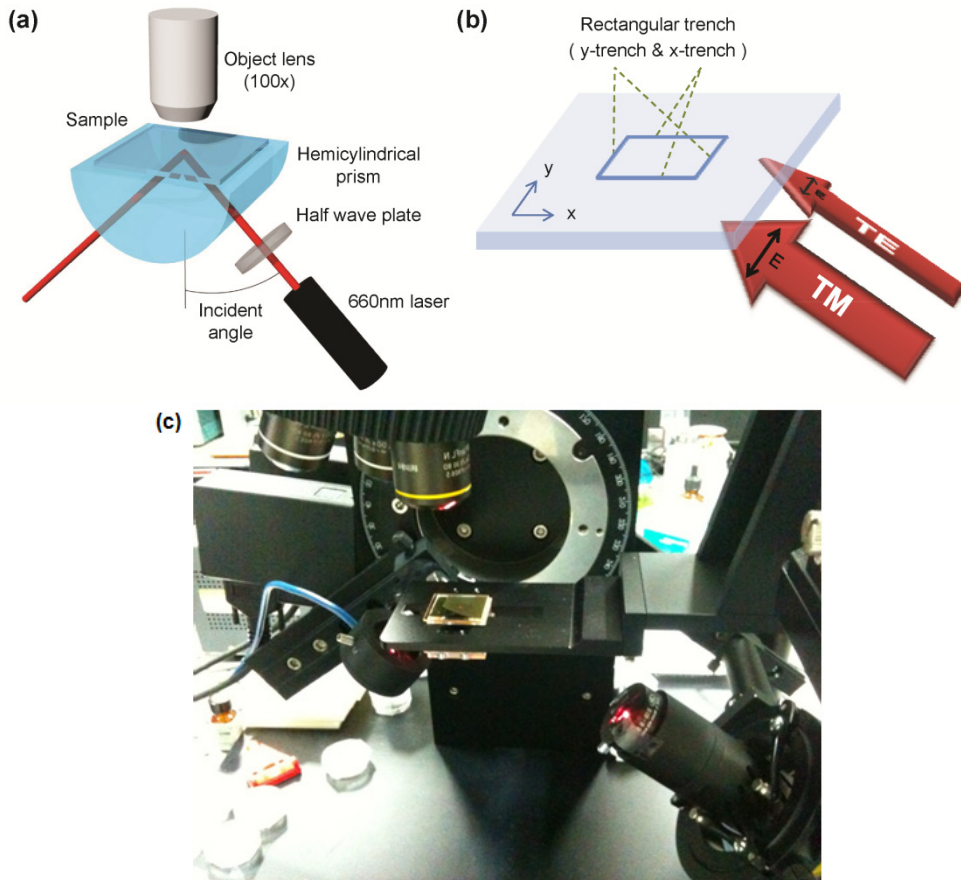


Figure 2.8. Image of (a) total internal reflection (TIR) set-up with prism, laser, and microscope lens and (b) terminology for the direction of the trench and the polarization of incident light. (c) Picture of experimental set-up. The polarization of incident light is switchable between transverse electric (TE) and transverse magnetic (TM) polarization by a half wave plate before the laser source and the incident angle is changed from 34° to 70° by a motorized rotation stage. The CCD camera, which is not shown here, is adapted to microscopy. The incident light has no y -directional momentum.

In the patterned substrate without Ag nanoparticles (Figures 2.9(a)-(c)), only scattering in the two y -trenches is observed because the direction of the trenches is perpendicular to the momentum of the incident light. Note that the scattering in x -trenches is not observable in both TE and TM polarizations. This scattering caused by the vacant trench is nearly independent of the polarization state of the incident light and is referred to herein as geometrical scattering. On the other hand, when the trench is occupied by Ag nanoparticles, the scattered field along the two x -trenches can be observed, as in Figures 2.9(e) and (f). The scattering in x -trenches is caused by the metal nanoparticles serving as light scatterers. Furthermore, the scattering in the two y -trenches

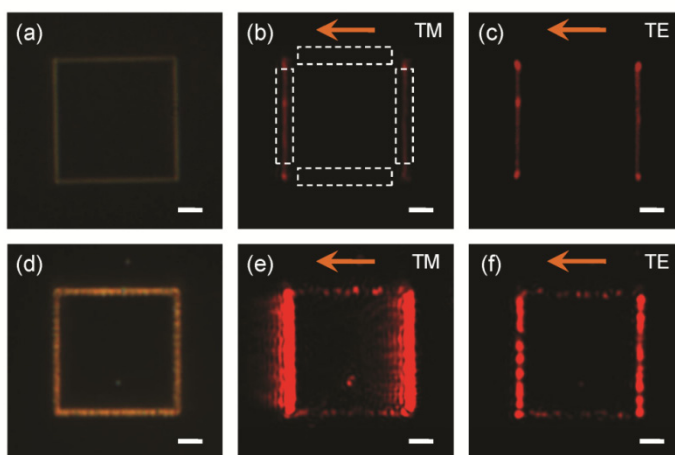


Figure 2.9. Dark field images of rectangular trenches (a)-(c) without and (d)-(f) with Ag nanoparticles. (a) and (d) are reflective scattering images by an unpolarized white light, halogen source, with unspecific momentum, and the others are transmissive scattering images through a hemicylindrical prism (b) and (e) by TM polarized light, (c) and (f) by TE polarized light of 660 nm with incident angle of 44° . The orange colored arrows indicate the directional momentum of incident light on the xy -plane of the sample surface. The regions within the white dotted frames of (b) are the sample images used to calculate their average brightness which means the scattering intensity from Ag nanoparticles and trenches. Each scale bar is 2 μm .

can be enhanced as in Figures 2.9(e)-(f) because of excitation of Ag nanoparticles in the trench by LSP. I refer to the scattering by the excitation of LSP as plasmonic scattering. In other words, the scattered intensities in the y -trenches are governed by both the geometrical and plasmonic scattering and are stronger than those of the x -trenches.

In Figures 2.9(e)-(f), the scattered intensities in the y -trenches are stronger for the TM polarized incident light. In order to examine the reason for this, I extracted the light intensity in each side of the trench from the captured CCD images. The extraction was conducted for the vicinity of the x - or y -trench regions which are depicted by dotted lines in Figure 2.9(b). For each region, the average brightness of the image pixels is taken to quantify the scattered intensities. The angle-dependent scattered intensities for the x - and y -trenches are plotted in Figures 2.10(a) and (b) with some corresponding CCD images included as insets located at the upper two rows. At the high incident angle regime, the intensities of all samples show a monotonous decrease, regardless of the conditions such as the direction of the trench, the polarization of incident field, and the existence of Ag nanoparticles. These general phenomena occur because the amount of the evanescent field, which leaks from the TIR structure and excites the surface plasmon, diminishes with an increase in the incident angle. When Ag nanoparticles are present in the trench, however, the scattered intensities by TM polarization are enhanced by a larger amount than those by TE polarization. In particular, the intensity is at a maximum near the critical angle of the TIR in TM polarization because the evanescent field reaches a maximum at that angle and the intensities around the maximum do not rapidly increase but gradually increase because of the deviations in the uniformity of the size and of the irregularity in the spatial distribution of Ag nanoparticles. For incident TM polarized light, the LSP conditions will be changed with the variation in the incident angle because the direction of the electric field is transverse to the y -trench (see Figure 2.8(b)). For the incident TE polarized light, however, the direction of the electric field is parallel to the y -trench and the resonance condition will not be affected by the incidence angle. The LSP conditions with a metal nanoparticle geometry can be found in the literature [40].

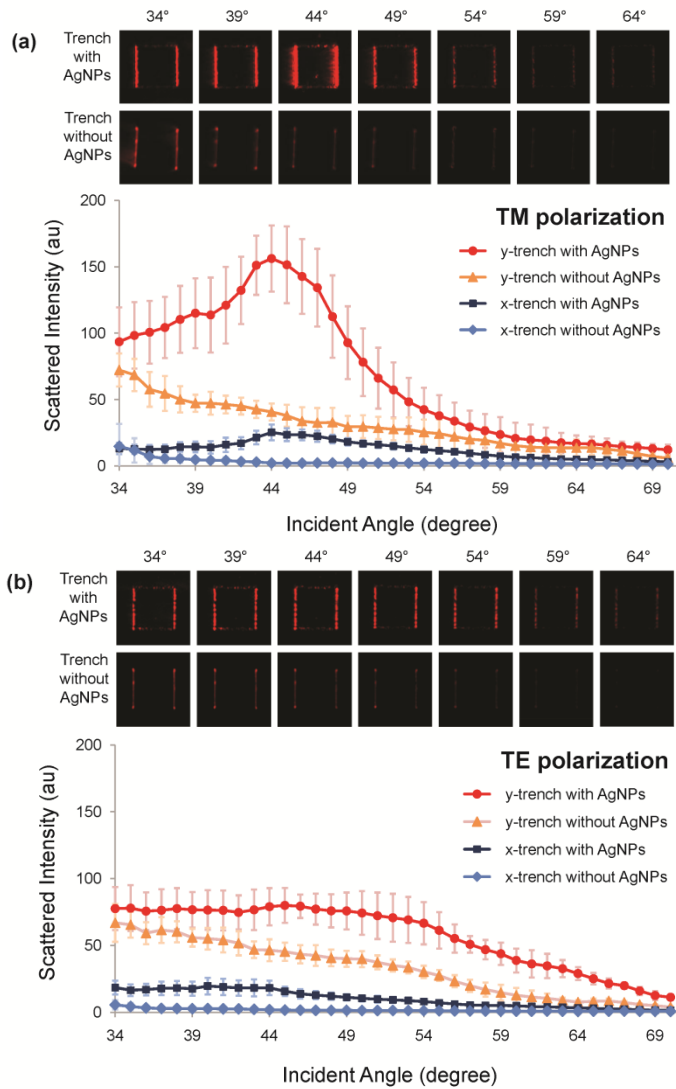


Figure 2.10. Graphs of scattered intensity vs. incident angle of (a) TM and (b) TE polarized light for the transmissive scattering images of the rectangular trenches with and without Ag nanoparticles. Some representative CCD images are inserted with their corresponding incident angles in the graphs. Laser source illuminates the sample through hemicylindrical prism with wavelength of 660 nm and incident angles from 34° to 70°. For convenience, Ag nanoparticles (NPs) are marked as AgNPs.

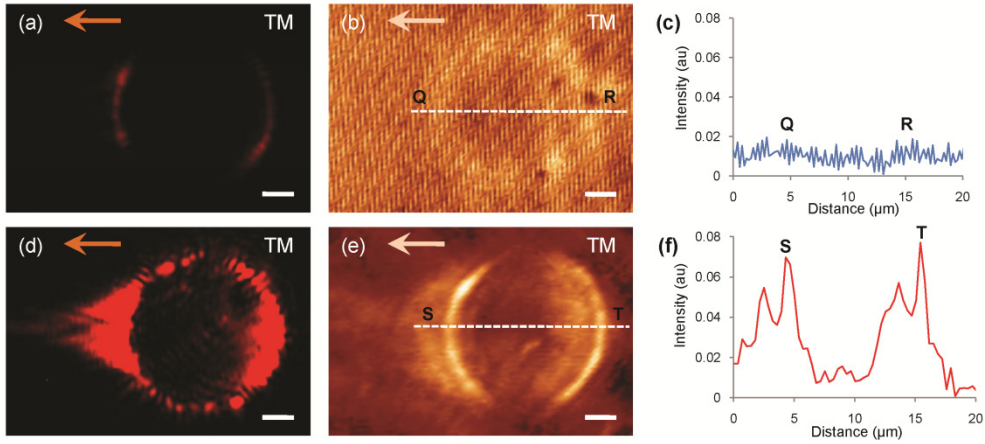


Figure 2.11. Transmission images of circular trench (a) without and (d) with Ag nanoparticles measured with a prism in TIR condition. NSOM images of circular trench (b) without and (e) with Ag nanoparticles measured with a prism in TIR condition. The enhanced near-field intensity profiles of cross-sections (the dotted lines QR and ST) of the images (b) and (e) are shown in (c) and (f). Laser source illuminates the sample with wavelength of 660 nm, TM polarization, and incident angle of 48° . Each scale bar is $2\ \mu\text{m}$.

Finally, I measured the far- and near-field response of a circular shaped sample which was illuminated using the same set-up with an incident angle of 48° to more carefully cross-check the LSP in another pattern instead of the rectangular shape. In both the far- and near-field scattering intensities, a significant difference was observed between those from a sample with and without Ag nanoparticles, as shown in Figures 2.11(a)-(f). The measured near-field intensities are particularly useful in terms of proving the existence of a significant effect of plasmonic scattering on total scattering in the circular trench, because the radiation characteristics of LSP show a strong near-field enhancement [70-73]. The profiles of the near-field intensity along the line of QR in Figure 2.11(b) and along the line of ST in Figure 2.11(e) are depicted in Figures 2.11(c) and (f), respectively. Note that the distance between the two peaks is exactly matched

with the diameter of the circular trench. As known from the profiles, the highest intensities of the near-field response at S and T correspond to the LSP excitation of Ag nanoparticles in the trench region and are enhanced at least four times higher than the intensities in the vacant trench regions at Q and R. Therefore, it can be concluded that the LSP excited by Ag nanoparticles can highly enhance the scattering at the trench, even though light illuminates it under TIR conditions.

2.4. Conclusion

Physically stable Ag nanoparticles can be selectively synthesized on a pre-patterned trench by taking advantage of selective hydrophobic and hydrophilic properties. In order to synthesize the precise pattern of Ag nanoparticles with a regular size, the PVP/silica layer should have sufficiently homogeneous PVP island domains for the appropriate nucleation of Ag nanoparticles in the trench and the fluorosilane layer should be sharply milled according to a pre-designed shape so that no surplus PVP domains are present out of the trench. The site-selectively synthesized Ag nanoparticles in a rectangular trench show polarization-dependent and incident angle-dependent scattering responses, as evidenced by optical measurements in the far- and near-fields. These dependencies imply that the causes of the responses are not only geometrical scattering due to the structure of the trench, but also plasmonic scattering due to the presence of Ag nanoparticles.

In terms of the process, the proposed site-selective synthesis technique may be a direct, effective, and convenient method for synthesizing and depositing Ag nanoparticles in various trenches with complex shapes at the same time. Although Corbierre et al. [74] already reported that E-beam lithography can directly array small sized metal nanoparticles on a flat substrate by thermally decomposing metal precursor such as Au(I)-thiolate, the site-selective synthesis technique proposed here has certain advantages: i) convenience in directly synthesizing metal nanoparticles, ii) less contamination of the other sites except the pre-designed trench, which will be helpful for

further use, and iii) good physical stability of metal nanoparticles that are deposited on a pre-designed trench due to chemical interactions between the metal nanoparticles and PVP. In terms of applications, although the site-selective synthetic process has some limitations in terms of producing Ag nanoparticles with a uniform shape and narrow size distribution, potential applications can be found, provided the process is further optimized. Because the Ag nanoparticles in the pre-designed trench can efficiently absorb incident light and highly reradiate it, even though the intensity of the incident light is weak or the incident angles are large, they can be applied to solar cells and SPR sensors. Moreover, if the Ag nanoparticles are synthesized in a metallic trench, which can be made by milling after depositing a thin metal layer between the fluorosilane and the PVP/silica layer, the LSP can be dramatically enhanced due to the coupling modes between them [69, 70]. I believe that the proposed method can contribute to several research fields, such as plasmonics, nano-optics, and optoelectronics.

Chapter 3

Plasmonic mixed states of PSPs and LSPs on AgNC@SiO₂ on Ag layer

The surface plasmon refers to a collective oscillation of electrons at an interface between metal and dielectric [8]. It has been received attention as a leading candidate for a core technology to realize next-generation devices, such as optical integrated circuits, optical memory, solar cells, and bio sensor chips because the surface plasmon can be manipulated with high speed in small volume of nano-scale. Surface plasmons can be categorized into two classes: propagating surface plasmons (PSPs) and localized surface plasmons (LSPs) [6-10]. PSPs are excited and continuously propagate along the flat surface of a metal layer on a dielectric prism when momentum of light matches to that of surface plasmons in dispersion relationship [6-8]. Contrary to PSPs, LSPs go around only discontinuous metal nanostructures and their properties are dependent on the size and shape of the structure [13-16].

While most plasmonic applications mainly adapt only one type of surface plasmons due to their opposite properties of propagation and localization, plasmonic sensors can use both properties simultaneously because they sensitively respond to small changes of the environmental refractive index [39]. Plasmonic sensors have been already commercialized in current industry [77]. The commercialized surface plasmon resonance (SPR) sensors produce detection results as a form of a distinctive dip signal in spectral reflectance due to the refractive index-dependent PSP excitation as shown in Figure 3.1(a) [78]. On the other hand, Figure 3.1(b) shows a fluorescence image sensor using LSPs in

laboratory scales though it has not been commercialized yet. It is used in detecting single molecules because fluorophores near metal nanoparticles can be excited by electromagnetic fields confined to the nanoparticles so that they can emit fluorescence with higher intensity than those without metal nanoparticles [79-81]. Although the SPR signal type can give clear quantitative data for bulk target materials contacted on a wide flat metal surface, the signal becomes weak when the volume or number of samples is small, and it cannot distinguish complex signal data when the sample is composed of different elements. Although the fluorescence image type can detect fine materials by using small metal nanoparticles, the image data are less quantitative than those of the SPR sensor.

We can acquire high quality and quantity of information from both signal and image data because each type of either PSPs or LSPs can supplement the weakness of the opposite type if using both of them at a time. Therefore, I tried to combine a thin metal layer for PSP excitation with metal nanoparticles for LSP excitation in order to provide the possibility and potential of the simultaneous dual detection, as shown in Figure 3.1(c). An SPR dip signal and fluorescence image can be detected through changes of PSPs on the thin metal layer and LSPs confined to metal nanoparticles, respectively, if this concept works well. I, especially, expect that PSPs excited on the thin metal layer can be partially localized as a form of LSP around metal nanoparticles in a certain optimized condition when metal nanoparticles are homogeneously distributed with a constant gap between the nanoparticles and the thin metal layer.

In order to verify the possibility of this concept, I calculated spectral reflectance and electromagnetic field profile of the proposed structure by using two-dimensional simulations. The experimental sample structure was prepared as a form of silver nanocube (AgNC) with silicon dioxide (SiO₂) shell on an Ag flat film in chemical synthesis and spin coating. The spectral reflectance and fluorescence image were measured in various angles of incident light. Statistic treatment for spatial distribution of particles was additionally conducted in order to accurately compare the results of calculation with the experimental data. I demonstrated effectuality of both simulation and experiment by showing that the nanoparticles on a flat metal layer follow the Weibull distribution and the statistically recalculated results are similar to the experimental results.

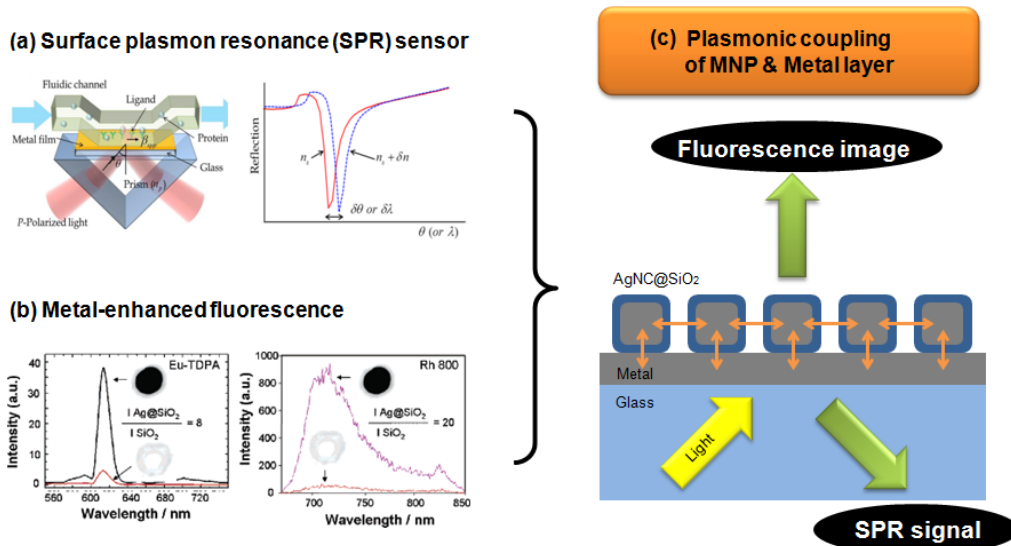


Figure 3.1. Schematic illustrations of (a) surface plasmon resonance sensor [78], (b) metal-enhanced fluorescence [79], and (c) the concept structure of Ag nanocubes with SiO₂ shell (AgNC@SiO₂) on thin metal layer for dual detection of SPR signal and fluorescence image.

3.1. Concept: plasmonic mixed states of PSPs and LSPs on AgNC@SiO₂ on Ag layer

PSP excited on the thin metal layer in Kretschmann configuration has enough intensity to detect a small change of refractive index, and LSP excited at metal nanoparticles can confine enough electromagnetic fields to enhance the fluorescence intensity of fluorophores around nanoparticles. It is, therefore, possible that PSP and LSP share strong electromagnetic fields in one metal structure if the structure is designed to be partially and concurrently available to excitation of both PSP and LSP. These simultaneous excitations enable the structure to utilize PSP and LSP for each appropriate purpose at a time. Additionally, plasmonic mixed states between PSP and LSP may occur

if they are excited at a region close to each other. Therefore, a concept structure can be suggested as shown in Figure 3.1(c). The SPR dip signal can be detected in reflectance mode with spectrometer, and fluorescence image can be pictured in transmittance mode with objective lens and CCD camera. The plasmonic mixed states can be induced not only among metal nanoparticles but also at small dielectric gaps between metal nanoparticles and metal layer. Figure 3.2 shows the geometries of the structure with the defined structural parameters. Ag was selected as metal materials of thin layer and nanocube because it has the longest propagation length of PSP in noble metals. SiO₂ thin shell is wrapped around Ag nanocube instead of coating SiO₂ thin layer on the whole surface of the Ag layer because SiO₂ must exist between metal nanoparticles and a thin layer to prevent their direct contact. In order to raise sensitivity of SPR, target molecules should contact directly on the metal surface of the thin layer except particles. Spectral reflectance at various incident angles, which can be converted into incident angle verse wavelength of reflectance graph (θ - λ_R map), should be calculated and measured to confirm the excitation of surface plasmons in the Kretschmann configuration. The data can be appropriate values to represent the excitation of the surface plasmons because light absorption as a result of the surface plasmon excitation causes the decrease of reflectance at an interface between the metal structure and prism in total internal refraction (TIR) condition and the Kretschmann configuration has been also verified as a classical experimental method in plasmonics for a long time [6-8]. Therefore the change of θ - λ_R map will imply alteration of the surface plasmon on the transformed structure.

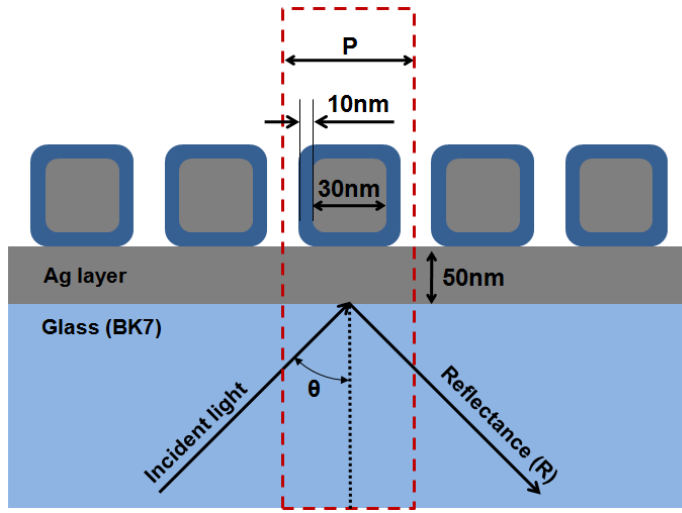


Figure 3.2. Schematic illustration of the proposed structure and parameters for simulation

3.2. Simulation

I calculated the reflective spectra from 400 nm to 800 nm at the incident angles from 40° to 80° using a simulation tool, the Rigorous Coupled Wave Analysis (RCWA) [82-84] to make a θ - λ_R map for one fixed structure. Two-dimensional (2D) simulation was selected because it is more efficient to save time than three-dimensional (3D) calculation. It is appropriate for enormous calculations in minutely scanning inter-particle distance, incident angle, and wavelength. In addition, when light illuminates to Ag nanocubes on an Ag layer in one direction on a perpendicular plane to the Ag layer plane, it can be approximated to the case of that light goes through a periodic array of long rods with square side in short axis direction. Although 3D calculation can make a more exact θ - λ_R map than 2D calculation can, I will demonstrate the validity of 2D simulation by comparing the results with the experimental data later.

3.2.1. Effect of plasmonic mixed states on the minimum reflectance band

Figure 3.3 shows that the θ - λ_R map changes as the period of core-shell units decreases from 3000 nm to 60 nm. The blue (or yellow) band on the map means minimum reflectance caused by surface plasmon excitation at specific incident angle and wavelength. The excitation type of the surface plasmons seems to be changed according to various periods of core-shell units on Ag layer. The position and slope of the band for the period 3000 nm is similar to those for 50 nm Ag layer without core-shell units. There may not be any plasmonic interaction between two core-shell units and only one unit on the wide Ag layer cannot give any influence on the PSP excitation condition because the period 3000 nm is a long length over a hundred times of 30 nm Ag core unit. Therefore, incident light may recognize the surface of the core-shell units on Ag layer with 3000 nm period as the surface of the 50 nm Ag layer without the units, so that the same type of surface plasmon, PSP, may be excited on two different structures. However, the position and shape of the minimum reflectance band are changed slowly, and finally the slope of the band becomes steep, as a period, which is a distance between core-shell units, decreases. In other words, the slope of the band increases as the population density of units on the Ag layer increases. In particular, the continuous band for the period 3000 nm is transformed into a discontinuous band, which consists of many small vertical bands, for the period 3000 nm and the number of small bands decreases in a sequence while the core-shell units go close to each other, and finally they become one band with a rapid slope again. Since the steep slope of the band means that the surface plasmon excitation condition becomes insensitive to the incident angle, we can instinctively infer that the influence of LSP, which is almost independent of incident angle [85-87], on the minimum reflectance band increases as the inter-unit distance decreases in Figure 3.3.

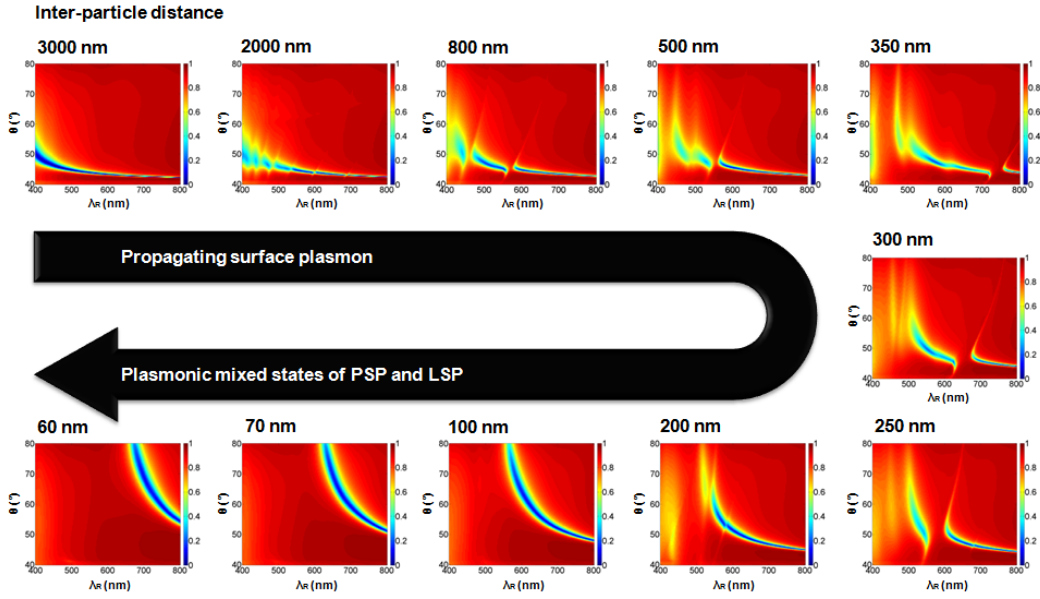


Figure 3.3. Change of the minimum reflectance band on θ - λ_R map depending on period.

I calculated H_y -field profiles at two points marked with black open circles on the map in Figures 3.4(a) and (b), where reflectance is minimum at the same wavelength 680 nm for each opposite period 3000 nm and 100 nm, in order to investigate the reason for increasing the slope of the band in a short period, as shown in Figures 3.4(c) and (d). In the case of the period 3000 nm, a core-shell unit does not have any influence on H_y -field made by PSPs on the Ag layer, so that LSPs cannot exist around it. Only PSPs contribute to the minimum reflectance band. On the contrary, in the case of the period 100 nm, H_y -fields are strongly confined to the SiO₂ gap between metal layer and Ag cores. The reason is that the excited and propagating surface plasmons are changed to a kind of LSPs at the gaps when PSPs meet the periodic core-shell nanoparticles on the way. Therefore, the coincident plasmonic waves of PSPs and LSPs are propagating at the 70° incident angle and 680 nm of wavelength. Those are the plasmonic mixed states between PSPs and LSPs, which are induced on the structure with a specific period in the excitation condition matched for both.

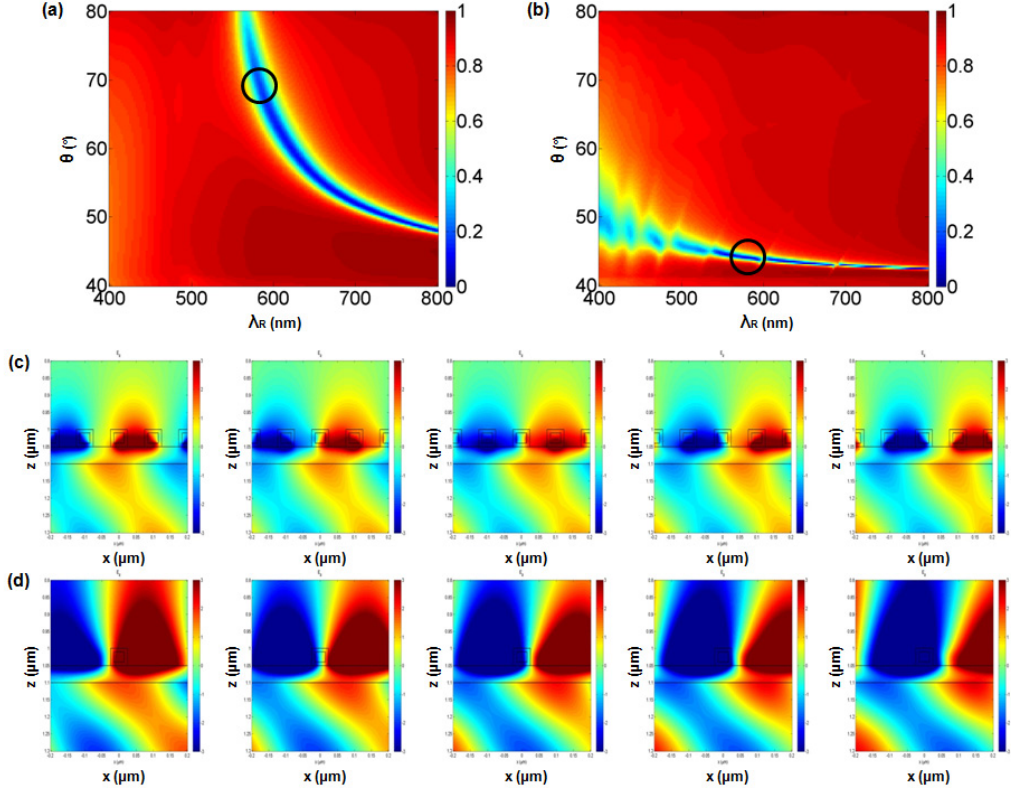


Figure 3.4. θ - λ_R maps for Ag cores (30 nm) with SiO₂ shell (10 nm) on Ag layer (50 nm) in (a) 100 nm and (b) 2000 nm of period condition. H_y -field profiles at (c) 69.55° and (d) 44.24° of different incident angles and 580 nm of same wavelength in different phase of incident light. Black open circles marked on the maps of (a) and (b) indicate positions where H_y -field profiles of (c) and (d) were calculated, respectively.

3.2.2. Effect of structural parameters on the position and intensity of the minimum reflectance band

Figure 3.5 shows the effect of SiO₂ shell thickness on the minimum reflectance band on the θ - λ_R map. The shell thickness means a gap between Ag core units and Ag layer. The shell thickness cannot influence on inter-unit distance because the distance is longer than the unit diameter. Therefore shell thickness is a factor which decides the resonance wavelength of the surface plasmons for the structure. In Figure 3.5, the position of the band gradually moves toward a long wavelength as shell thickness increases, because surface plasmons with a long resonance wavelength can be appropriately confined to the widened gap. The slope of the band is also influenced by the thickness. PSPs, which have the incident angle-dependent property, mainly induce the minimum reflectance band because the mixed state of PSPs and LSPs cannot help becoming weak as the gap distance, which is shell thickness, increases. The band mostly affected by LPSs has a steep slope so that it becomes insensitive to the incident angle. The phenomena can be confirmed in Figure 3.5. The band slope of Figure 3.5(a) is steeper than that of Figure 3.5(c). The band in Figure 3.5(a) becomes similar to that for a metal layer with grating because the structure will become the grating structure when the shell disappears. If the shell becomes very thick in inverse so that Ag core units become far away from the Ag layer, the band will be similar to that for a thin metal layer without units because metal unit away from metal layer may not be recognized by light and any LSP around them cannot be coupled by PSP.

Figure 3.6 shows the effect of Ag core size on the minimum reflectance band on the θ - λ_R map. The band for the structure with small cores is located in shorter wavelength than that for the structure with large cores. Considering only LSPs of Ag nanoparticles dispersed in solution, which is a simplified model, except for the interaction between PSPs and LSPs, the minimum reflectance band moves from a long to short wavelength because the LSP resonance wavelength becomes short as the Ag nanoparticle size decreases [9, 10]. For this case, the band similarly moves depending on the Ag core size

because the mixed state of PSPs and LSPs is the strongest at the wavelength where the excitation conditions of PSPs and LSPs match to each other. If Ag cores become very small, the surface plasmon has almost a PSP type on the metal layer because incident light cannot recognize the small metal cores.

Figure 3.7 shows the effect of Ag layer thickness on the minimum reflectance band on the θ - λ_R map. The band becomes weak when the metal layer is thick over 70 nm in Figure 3.7(c). The reason is that PSPs are weakly excited on the thick metal layer due to unmatched momentum of incident light and surface plasmons [6-8] and LSPs cannot be excited at Ag cores because the incident light cannot penetrate it. In the other hand, the band has a wide width and low reflectance when the layer is thin less than 30 nm because light can penetrate it and excite LSPs on Ag core units though PSPs is less excited due to unoptimized Ag layer thickness. The band will be similar to that for only LSPs of Ag core units if the thickness is extremely thin.

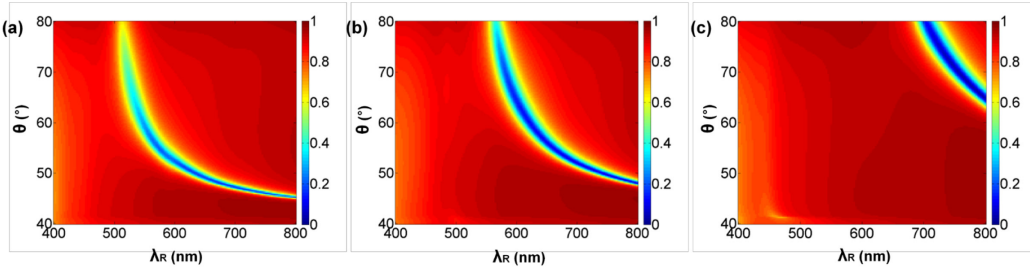


Figure 3.5. Effect of SiO₂ shell thickness on the minimum reflectance band. The thicknesses are (a) 1 nm, (b) 10 nm, and (c) 35 nm.

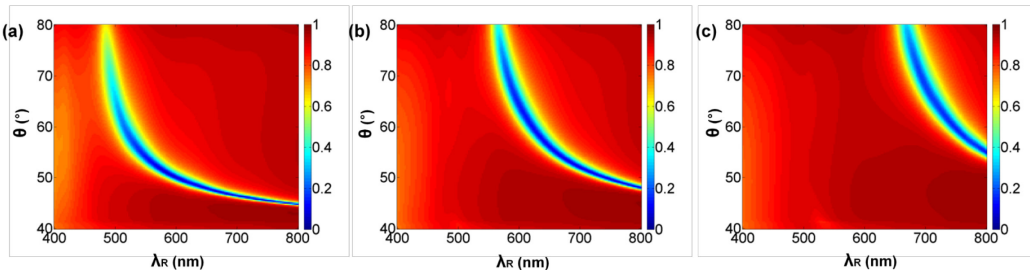


Figure 3.6. Effect of Ag core size on the minimum reflectance band. The diameters are (a) 20 nm, (b) 30 nm, and (c) 40 nm.

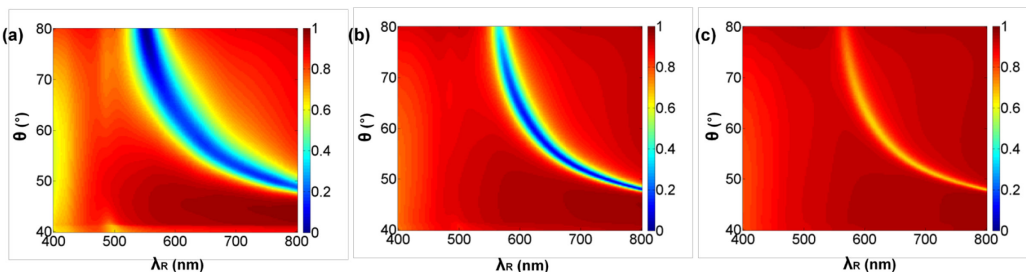


Figure 3.7. Effect of Ag layer thickness on the minimum reflectance band. The thicknesses are (a) 30 nm, (b) 50 nm, and (c) 70 nm.

3.3. Experiment

3.3.1. Chemical fabrication: AgNC@SiO₂ on Ag layer

Synthesis of Ag nanocube: 48 mg/mL solution of silver nitrate (AgNO₃, Sigma-Aldrich), 20 mg/mL of poly(vinyl pyrrolidone) (PVP, Sigma-Aldrich), and 3 mM solution of sodium hydrosulfide (NaHS, Sigma-Aldrich) in ethylene glycol (EG, J.T. Baker) were prepared. 6 mL of EG was heated and stirred with a silicon coated magnetic bar for 1 h in a 20 mL glass vial. 0.08 mL of the sulfide solution, 1.5 mL of the PVP solution, and 0.5 mL of the AgNO₃ solutions were sequentially injected. As silver nitrate was added, the clear and colorless solution immediately turned purple, followed instantly by a bright yellow color. After 2 – 3 min. into the reaction, the solution darkened to an orange color. After 6 – 8 min., the solution changed to a brown color and concurrently became opaque. The final produce was washed with acetone, ethanol, and water.

Synthesis of silicon dioxide shell: Four kinds of AgNC solutions, which are undiluted, 1.25-fold, 2.5-fold, and 20-fold diluted solution, were prepared by diluting the synthesized AgNC solution with ethanol. 25% ammonia solution and 10% solution of tetraethoxysilane (TEOS, Sigma-Aldrich) in ethanol were also prepared. 3.8 mL ethanol was stirred in 20 mL glass vial and then 1.5 mL of the AgNC solution, 0.4 mL of the ammonia solution, and 0.4 mL of the TEOS solution were sequentially injected to the ethanol in the vial. The mixed solution was stirred at room temperature for 12 h.

Preparation of AgNC@SiO₂ on Ag layer: Ag layer with thickness of 50 nm was evaporated on glass substrate with e-beam evaporator. The Ag layer on glass was spin-coated with the four AgNC@SiO₂ solutions at 200 rpm for 20 sec and then dried at 100°C for 2 min.

3.3.2. Optical measurement: dual detection of SPR signals and fluorescence images

Figure 3.8 shows an illustration of the microscope set-up in order to measure an incident angle-dependent reflectance spectrum. The spectral reflectance of the sample was obtained with a spectrometer at several incident angles using a white light source in the TIR geometry.

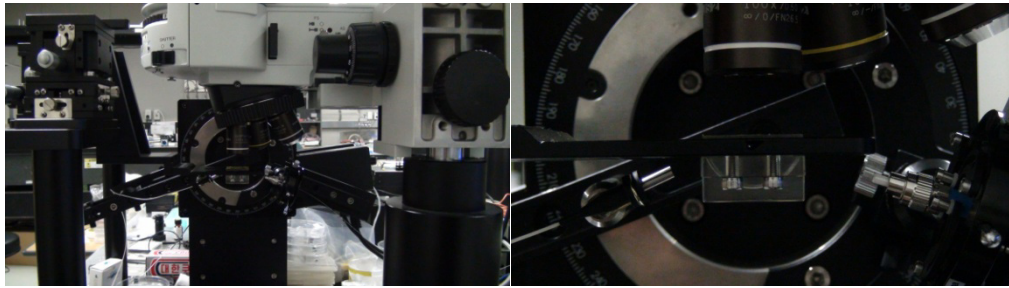
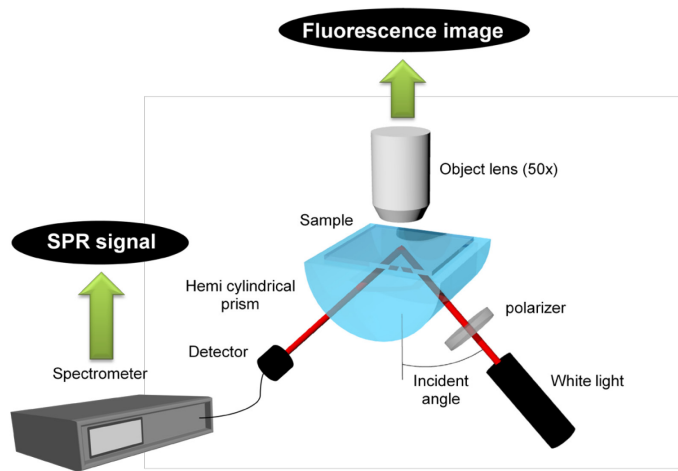


Figure 3.8. Experimental set-up of the Kretschmann configuration.

3.3.3. Results and discussion

I prepared the proposed structure by spin-coating Ag nanocube with SiO₂ shell (AgNC@SiO₂) on the 50 nm Ag layer in order to observe the phenomena that the band slope for the structure is changed on the θ - λ_R map. AgNC@SiO₂ can contact in face-to-face between cubes and a substrate so that they can be assembled denser than other shaped structures even if they are randomly scattered on a substrate. They were synthesized with the polyol method [88-90] and enclosed with SiO₂ shell in the stober process [91-93]. Figure 3.9 indicates characteristics of materials used in experiment.

Comparing Figures 3.9(a) and (b), we can observe that AgNCs have a cubic shape with approx. 30 nm in diameter and SiO₂ shell is wrapped around AgNC with approx. 10 nm in thickness in the TEM images. We can also confirm that most cubes contact with Ag layer in face-to-face. Figures 3.9(c) and (d) show molecular structures of fluorophores, which are Fluorescein isothiocyanate (FITC) and Rhodamine B isothiocyanate (RITC). They were used to measure fluorescence images.

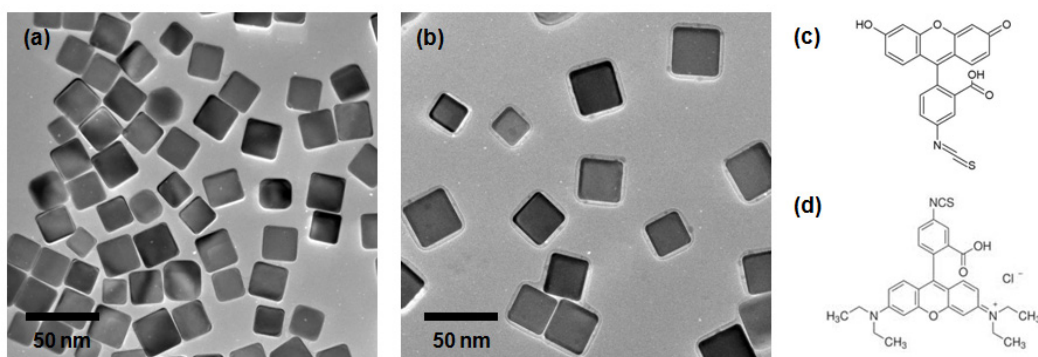


Figure 3.9. TEM images of (a) AgNC and (b) AgNC@SiO₂. Molecular structures of (c) Fluorescein isothiocyanate (FITC) and (d) Rhodamine B isothiocyanate (RITC).

Figure 3.10 provides FE-SEM images of AgNC@SiO₂ settled on the 50 nm Ag layer with different population densities. The population density can be controlled by spin-coating with different concentration of the nanoparticle-dispersed solution. Four diluted solutions were prepared by adding ethanol to the original synthesized AgNC@SiO₂ solution, which are 20-, 2.5-, 1.25-fold dilutions, and the undiluted solution. The FE-SEM images indicate that the population density increases in proportion to the concentration of AgNC@SiO₂ solution. The average values and standard deviations of inter-particle distances are 291.2 ± 149.2 nm, 200.3 ± 84.9 nm, and 117 ± 40.1 nm in Figures 3.10(b)-(d), respectively. (The values cannot be measured in Figure 3.10(a) due to large deviation)

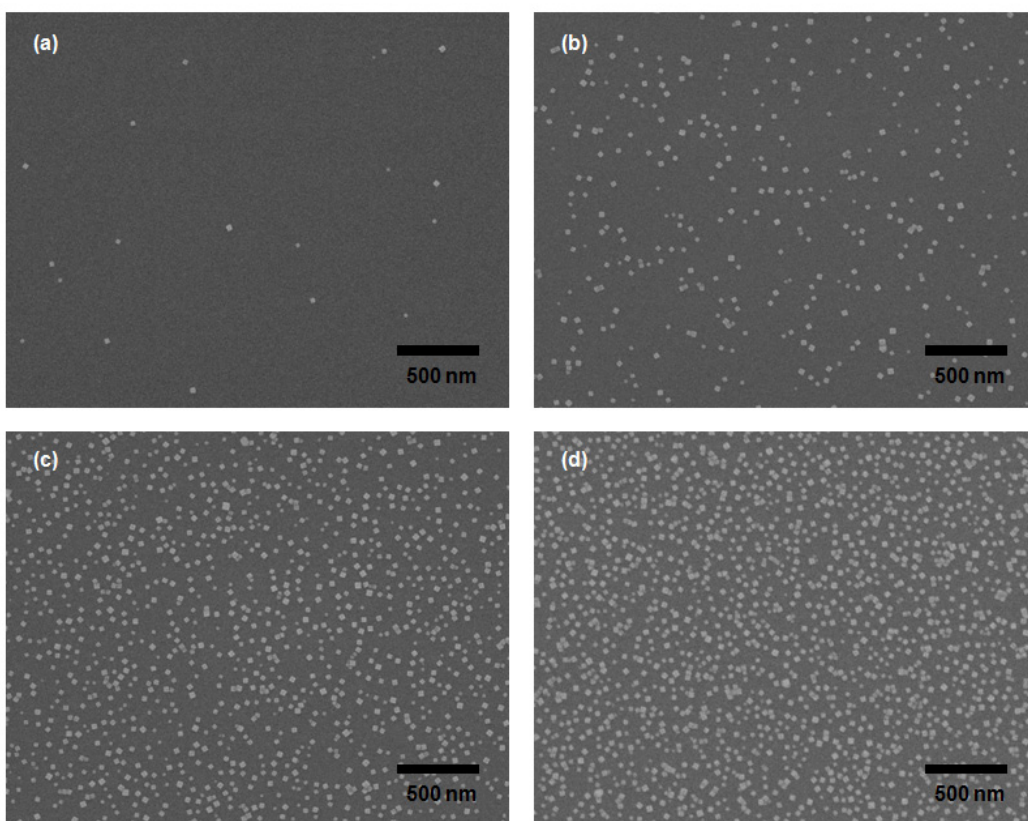


Figure 3.10. FE-SEM images of AgNC@SiO₂ coated on Ag layer (a) 20-, (b) 2.5-, (c) 1.25-fold dilutions, and (d) undiluted solution. The scale bars are 500 nm.

I coated AgNC and AgNC@SiO₂ solutions of the 2.5-fold, 1.25-fold dilutions and undiluted solution on glass and 50 nm Ag layer, and then measured reflectance spectra of those twelve samples in dark field mode. The result spectra are shown in Figure 3.11. Wavelength having the maximum reflectance, which means resonance wavelength of the surface plasmon excited on the sample, shifts toward a long wavelength in all cases when the population density increases, when SiO₂ shell warps around AgNC, and when nanoparticles are located on the Ag layer. First, as the population density increases, the particles become electromagnetically coupled and cause a shift of the resonance to lower

frequencies for parallel polarization because population density of nanoparticles increases and inter-particle distance decreases [94]. Second, when AgNC is coated with SiO₂ shell, the plasmon peak is red shifted because the refractive index of SiO₂ is higher than that of air [91, 93]. Third, when AgNC and AgNC@SiO₂ are located on the Ag layer, the red shift of the surface plasmon resonance occurs because of a dipole-surface interaction [95, 96]. Therefore, I confirmed that all the spectral tendencies coincide with previous research results in literatures by basically measuring those optical properties.

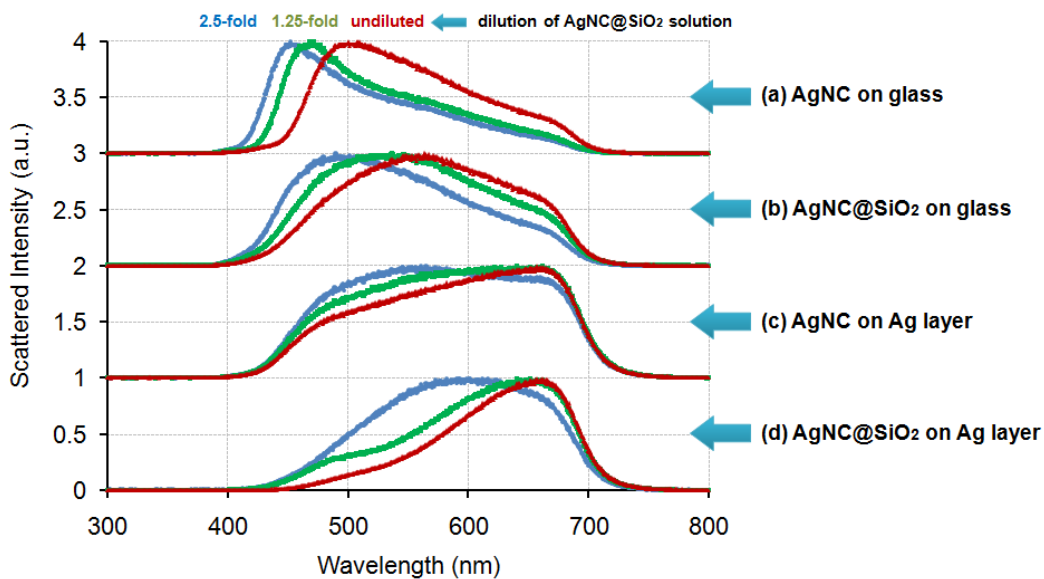


Figure 3.11. Reflectance spectra of (a) AgNC on glass, (b) AgNC@SiO₂ on glass, (c) AgNC on Ag layer, and (d) AgNC@SiO₂ on Ag layer in dark field mode. Blue, green, and red spectra were measured for samples of 2.5-fold, 1.25-fold dilutions, and undiluted solution.

Figure 3.12 shows optical microscopy images of the sample measured in Kretschmann configuration. The images for only Ag layer and only AgNC@SiO₂ on glass substrates as references are shown with incident angles in Figures 3.12(a) and (b). The former images are almost dark even at the PSP excitation angle because the transmitted light is too weak. The latter images emit blue color, which is included in the resonance wavelength of LSP for 30 nm Ag nanoparticles, at all incident angles. On the contrary, images for AgNC@SiO₂ on Ag layer in Figure 3.12(c) become slowly bright as the incident angle increases, reaching the maximum brightness at the PSP excitation angle, and fade out after the excitation angle. The images for adding FITC and RITC into the samples are shown in Figures 3.12(d) and (e) in order to distinguish the angle-dependent resonance wavelength of white light in detail. The color green emitted by FITC in Figure 3.12(d) becomes maximum intensity at a higher angle of 55° than red color emitted by RITC at 52° of the incident angle. They have the highest intensity at different incident angles for the same structure because the absorption and emission wavelength of FITC are approx. 480 nm and 520 nm while those of RITC are approx. 560 nm and 580 nm, respectively. Those phenomena experimentally support all fundamental plasmonic properties which are the mixed states of PSP and LSP, and fluorescence enhanced by surface plasmons on AgNC@SiO₂ on Ag layer.

SPR signals for three types of sample structures were measured by scanning incident angles, and then experimental θ - λ_R maps were completed as shown in Figure 3.13. They are same samples with 20-fold, 1.25-fold dilution, and undiluted AgNC@SiO₂ solutions, measured in Figures 3.10(a), (c), and (d). The experimental θ - λ_R maps display three different slopes of the minimum reflectance bands. In the case of the sample using the 20-fold diluted solution, Figure 3.13(a), the SPR dips are relatively sharp and the band slope is gentle. The position and shape of the band are similar to those for only 50 nm Ag layer because the sparse AgNC@SiO₂ particles cannot influence the excitation of PSPs on Ag layer. As their population density increases, the mixed state of PSPs and LSPs becomes stronger so that the band slope increases, as shown in Figures 3.13(b) and (c).



Figure 3.12. Optical microscope images of (a) Ag layer, (b) AgNC@SiO₂ on glass, (c) AgNC@SiO₂ on Ag layer, (d) AgNC@SiO₂ with FITC on Ag layer, and (e) AgNC@SiO₂ with RITC on Ag layer, which were measured in Kretschmann configuration. The thickness of the Ag layer is 50 nm, the diameter of AgNC is 30 nm, and the thickness of SiO₂ shell is 10 nm.

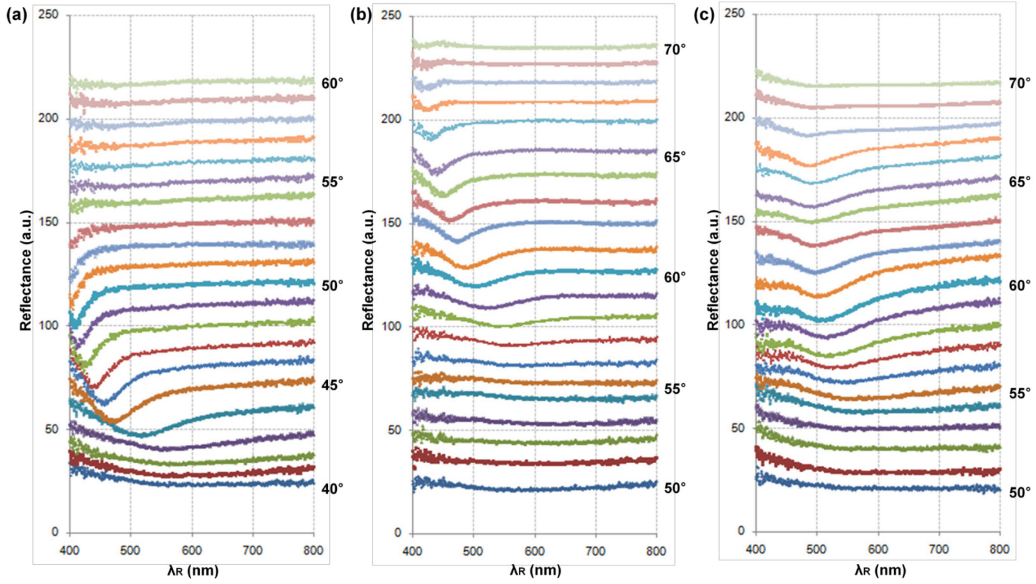


Figure 3.13. The experimental θ - λ_R maps of the samples coated on 50 nm Ag layer with (a) 20-fold, (b) 1.25-fold dilution, and (c) undiluted AgNC@SiO₂ solutions.

However, there are some differences between simulation and experimental results. In experiment, the AgNC@SiO₂ particles are settled on Ag layer with certain distributed distances among them because they are randomly scattered in the process of spin coating, while, in simulation condition, the units are located at exact lattice points with a fixed distance. Therefore, we need to consider the distance distribution in calculation so as to compare the outcomes between simulation and experiment as accurately as possible. I measured the inter-particle distances of AgNC@SiO₂ on Ag layer in FE-SEM images of Figures 3.10(b)-(d) and then calculated the average and standard deviation of the distance distribution with a statistical method as shown in Figures 3.15(a)-(c). The average values and standard deviations of inter-particle distances are 291.2 ± 149.2 nm, 200.3 ± 84.9 nm, and 117 ± 40.1 nm in Figures 3.10(b)-(d), respectively. The distribution does not follow

normal distribution because it is not bilaterally symmetrical with using the average value as a center and have a long tail in long inter-particle distances. We should find an appropriate distribution model to coincide it with the real distribution of inter-particle distances in the sample.

In probability theory and statistics, Weibull distribution is a continuous probability distribution. It is named after Waloddi Weibull, who described it in detail in 1951. This distribution is widely used in analysis of life data, reliability, size distribution of particles, and elsewhere due to its versatility and relative simplicity [97]. The probability density function of a Weibull random variable x is

$$f(x; \alpha, \beta) = \frac{\beta}{\alpha} \left(\frac{x}{\alpha}\right)^{\beta-1} e^{-(x/\alpha)^\beta} , \quad (3.1)$$

where $\alpha > 0$ is the scale parameter and $\beta > 0$ is the shape parameter of the Weibull distribution. A change in the scale parameter, α , has the same effect on the distribution as a change of the abscissa scale. Increasing the value of α while holding β constant has effects of stretching out the probability density function. Since the area under a probability density function curve is a constant value of one, the peak of the probability density function curve will also decrease with the increase of α . If α is increased while β is fixed, the distribution gets stretched out to the right and its height decreases while maintaining its shape and location. If α is decreased while β is kept the same, the distribution gets pushed in towards its beginning or zero, and its height increases. The shape parameter, β , is also known as the Weibull slope. This is because the value of β is equal to the slope of the line in a probability plot. Different values of the shape parameter can have marked effects on the behavior of the distribution. In fact, some values of the shape parameter will cause the distribution equations to reduce to those of other distributions. For example, it interpolates between the exponential distribution ($\beta = 1$) and the Rayleigh distribution ($\beta = 2$). Figure 3.14 shows the Weibull distribution with various values of α and β .

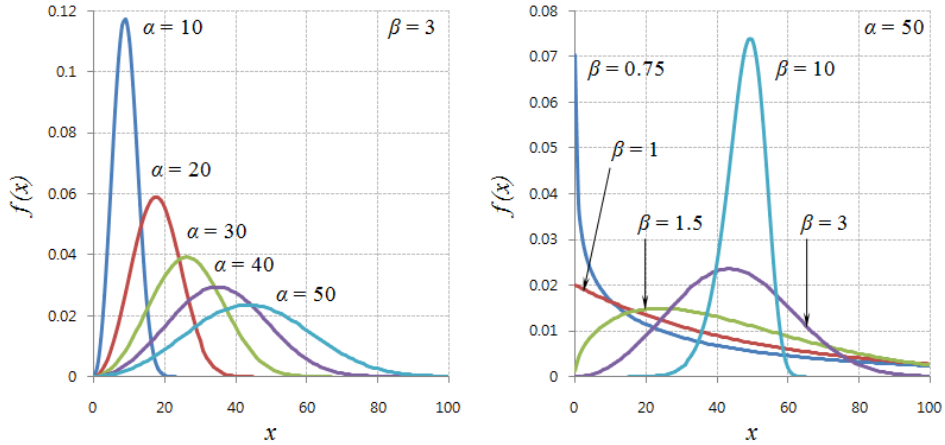


Figure 3.14. The Weibull distribution graphs with various values of α and β .

I tried to fit the inter-particle distance distributions of experimental samples in Figures 3.15(a)-(c) to the Weibull distributions with the specified parameters in Figures 3.15(d)-(f). The three sets of the scale and shape parameters were inversely calculated from the averages and standard deviations acquired from experimental results. When random numbers of distances were generated according to the Weibull distribution with α and β in those three cases, we can confirm that they are considerably similar to the real distributions of the experimental samples as shown in Figure 3.15. The distributions additionally denote the tendency that the standard deviation increases as the average inter-particle distances increase. Considering this tendency, we can expect that experimental results are more similar to the simulation results in the case of a short distance than the case of a long distance between nanoparticles.

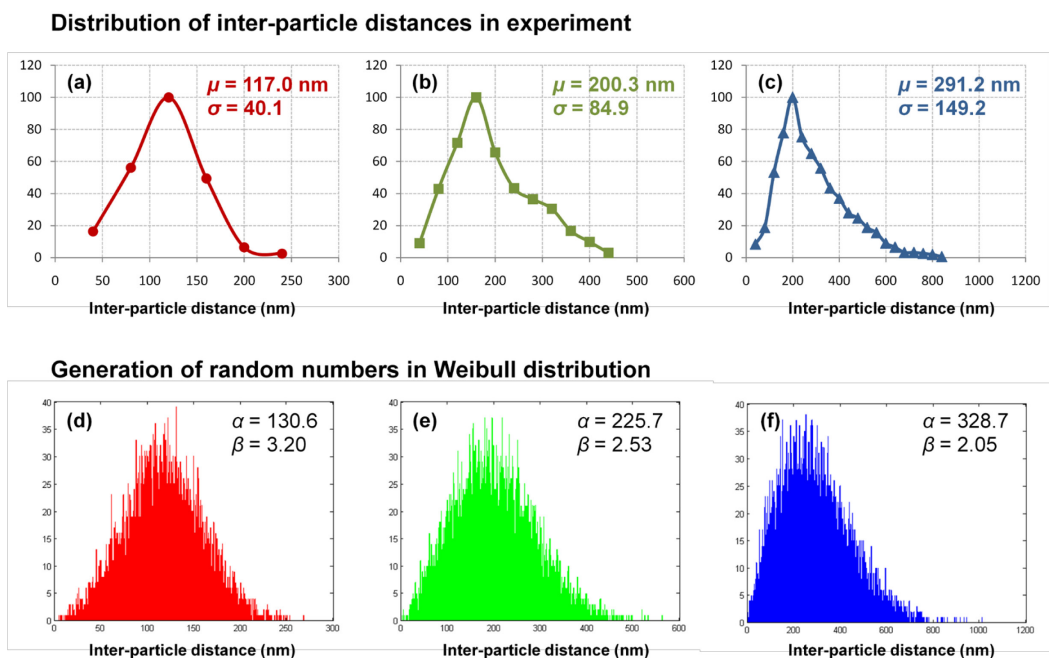


Figure 3.15. Inter-particle distance distributions (a)-(c) measured in experimental data and (d)-(f) calculated with the average and standard deviation values of the samples. They follow the Weibull distributions: (a) and (d) for the undiluted, (b) and (e) for 1.25-fold, and (c) and (f) for 2.5-fold diluted AgNC@SiO₂ solutions

Fifty of random numbers were generated like the Weibull distribution charts in Figures 3.15(d)-(f) and then inputted into a simulation condition shown as a schematic diagram in Figure 3.16. Namely, fifty of the cubic units with random Weibull distribution in one period were calculated under the same conditions as the previous simulations without considering the distribution. The recalculated θ - λ_R map is demonstrated in Figure 13(a) with the initially calculated map in Figure 13(b) and the experimental map in Figure 13(c) for comparison.

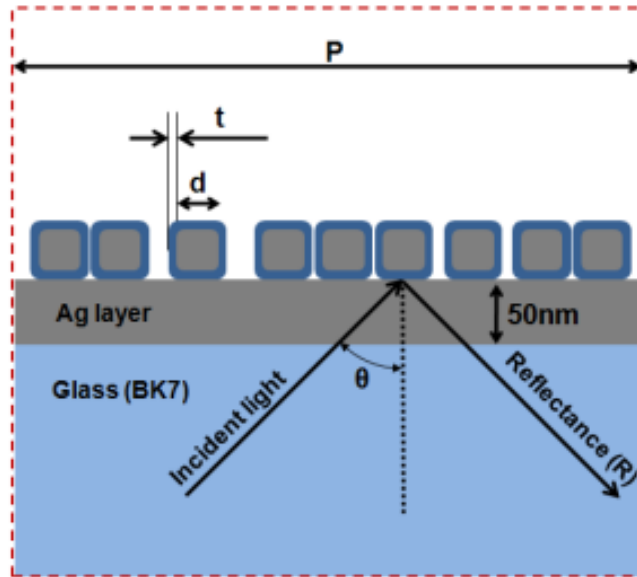


Figure 3.16. Schematic illustration of a structure and parameters for simulation including the Weibull distribution.

Figure 3.17 shows the recalculated results using the Weibull distribution. When the distance distribution is applied to the simulation condition, the width and intensity of the minimum reflectance band are transformed while the position and slope of the band are almost kept. Most of all, the deformation of the band is larger at a short wavelength than at a long wavelength. The Weibull distribution blurs the minimum reflectance band at a shorter than 600 nm of wavelength while it does not in the region of 700 - 800 nm in comparison of Figures 3.17(a) and (b). The reason may be that light with short wavelengths can be more sensitive to the same variation of the unit distribution and then recognize the distribution to be more disordered than that with long wavelengths. In addition, the degree of the band deformation increases as standard deviation, i.e. disorder, increases as shown in Figure 3.17.

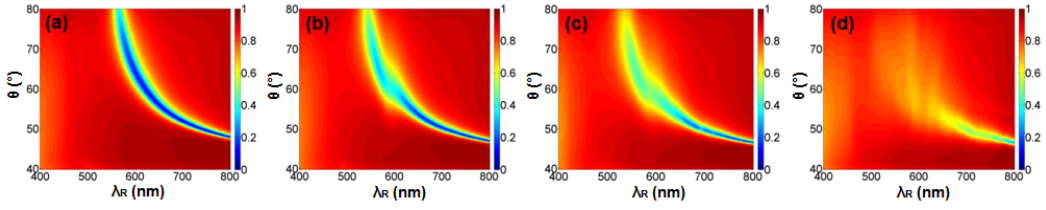


Figure 3.17. Change of θ - λ_R maps depending on standard deviations, which are (a) 0 nm, (b) 10 nm, (c) 40 nm, and (d) 80 nm, in the Weibull distribution of inter-particle distance with an average distance of 117 nm.

For quantitative analysis on the convergence of reflectance, I iteratively calculated the reflectance over 500 times at an incident angle of 60° and a wavelength of 600 nm for the structure with the same average distance, 117 nm, but different standard deviations, which are 10, 40, 49, and 80 nm in the Weibull distribution. Figure 3.18 shows the results. As the standard deviation of the Weibull distance distribution increases, the standard deviation of reflectance are kept at approx. 5%, while the average reflectance increases from 50% to 70%. In other words, although variance or disorder of the inter-particle distance increases, the minimum reflectance band still exists at the same position except for increasing the reflectance. Therefore, I could measure the sequence of weak SPR dips and confirm the existence of the band on the θ - λ_R map from the experiment even though AgNC@SiO₂ are randomly scattered in the Weibull distribution.

The field profiles for different standard deviation in the Weibull distribution with the same average distance, 117 nm, are shown in Figure 3.19. As the standard deviation increases from 15 nm to 80 nm, absorption at the gap between Ag units and Ag layer caused by surface plasmons slowly decreases and reflectance slowly increases because the nanoparticles derails the exact spatial position matched with a resonance wavelength of PSP or coupled between PSP and LSP. As the population density of AgNC@SiO₂ decreases, therefore, standard deviation increases, deviation of AgNC@SiO₂ from the exact position increases, disturbance in the mixed states of PSP and LSP increases, and finally reflectance intensity decreases.

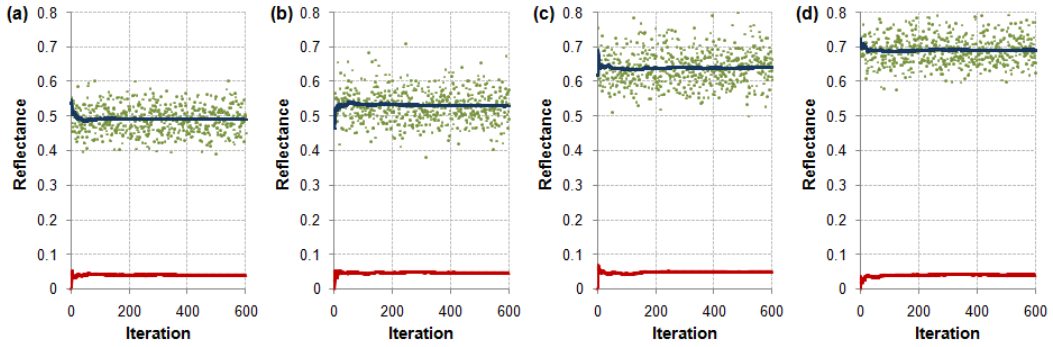


Figure 3.18. Effects of standard deviations on the convergence of the minimum reflectance at an incident angle of 60° and a wavelength of 600 nm in iteration of the simulation. The standard deviations are (a) 10 nm, (b) 40 nm, (c) 49 nm, and (d) 80 nm in the Weibull distribution of the inter-particle distance with 117 nm of the average distance. The green dots, the upper blue lines, and the lower red lines are raw, average, and standard deviation data of reflectance, respectively.

In addition, in order to check the validity for that the structural condition of 50 units per period are appropriate to calculate a reasonable result, iterative calculations were conducted with various number of units per period from 20 to 60 as shown in Figure 3.20. The calculated reflectance has a large standard deviation over 13% when the AgNC@SiO_2 units are below 20 in a period. As the number increases, the standard deviation decreases and it is kept at 5% after 50 units per period. Therefore, the number of units in a period was set as 50 to reduce calculation time in a lower limit of convergence.

Figure 3.21 shows the effect of the Weibull distributions on the θ - λ_R maps for the AgNC@SiO_2 on Ag layer structures having three different inter-particle distances. When the Weibull distribution of experimental data is fed back to simulation, there is an advantage though the band blurs and the reflectance increases. We can see that the perturbation of standard deviation prevents the sudden discontinuity, which originates from exact periodicity of unit array, of the minimum reflectance band. The discontinuity

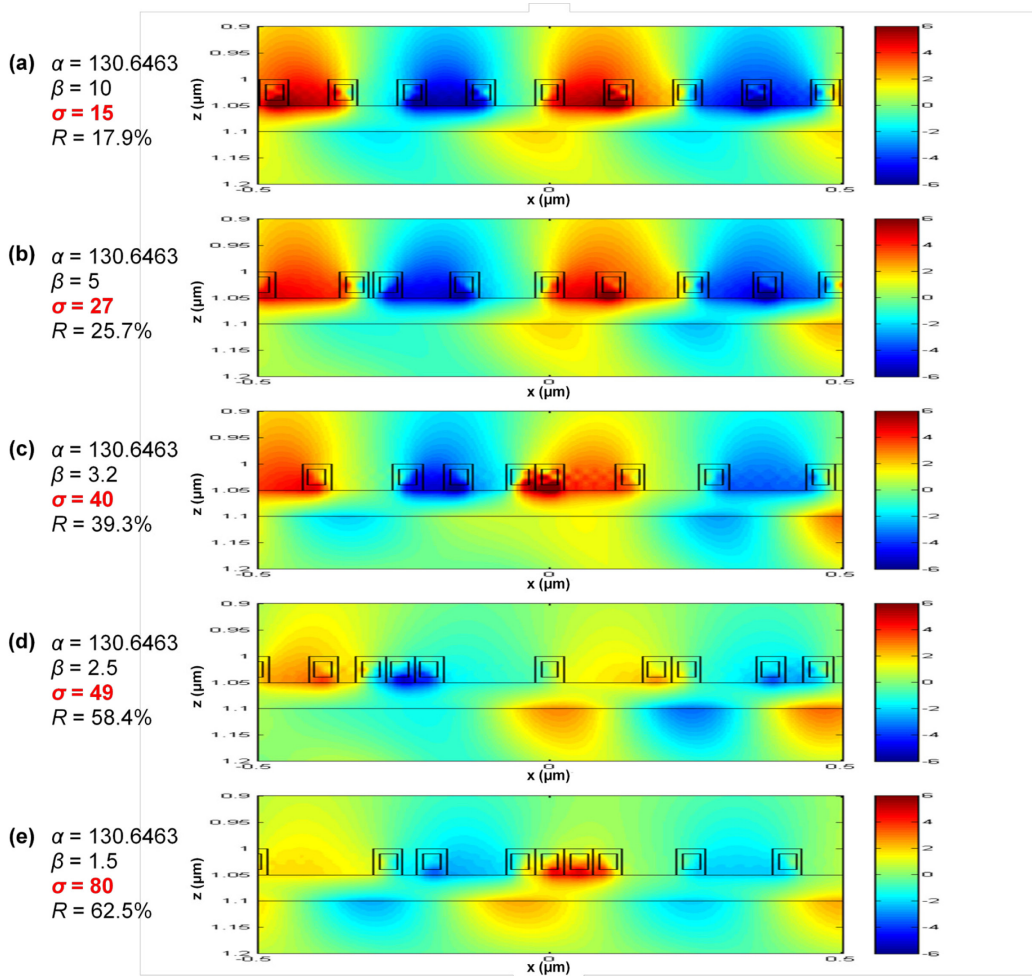


Figure 3.19. H_y -field profiles of AgNCs (30 nm) with SiO₂ shell (10 nm) distributed on Ag layer (50 nm) at an incident angle of 50° and a wavelength of 650 nm. Their average distances are same, 117 nm, and their standard deviations are (a) 15 nm, (b) 27 nm, (c) 40 nm, (d) 49 nm, and (e) 80 nm.

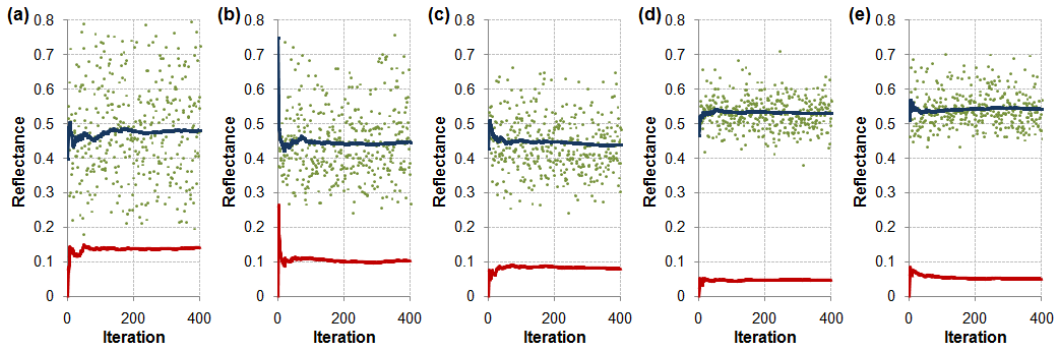


Figure 3.20. Effect of unit (particle) number in a period on and convergence of reflectance. There are (a) 20, (b) 30, (c) 40, (d) 50, and (e) 60 of units per period in the Weibull distribution. The green dots, the upper blue lines, and the lower red lines are raw, average, and standard deviation data of reflectance, respectively.

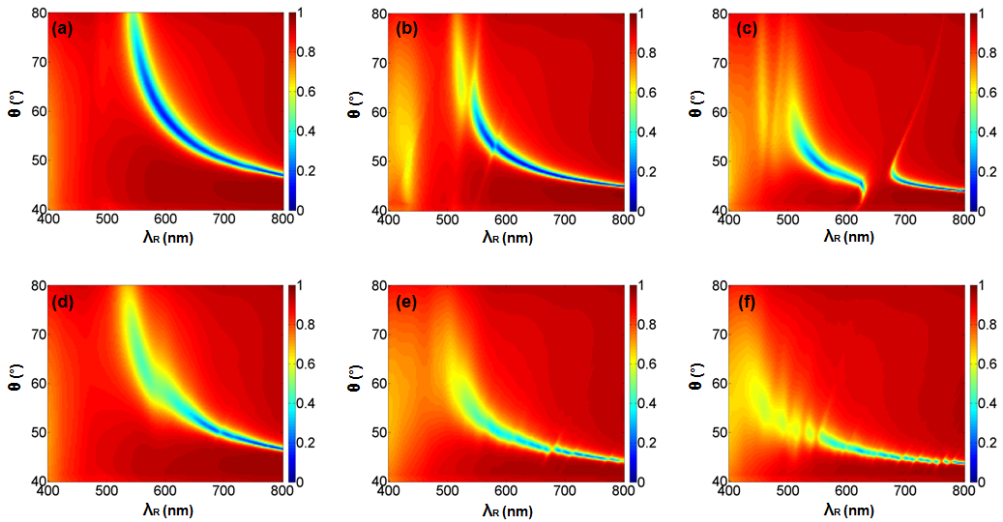


Figure 3.21. Comparisons of θ - λ_R maps for three kinds of inter-particle distances (a)-(c) without and (d)-(f) with the Weibull distribution. The three kinds of distances are: (a) and (d) 117 nm, (b) and (e) 200 nm, and (c) and (f) 300 nm. The standard deviations are (d) 40.1 nm, (e) 84.9 nm, and (f) 149.2 nm, which are same as the values of the experimental samples and Figure 3.15.

dominantly occurs in the structure with a long distance between nanoparticles because the probability and frequency to match the resonance wavelength of PSPs with that of LSPs, which are excited on infrequent Ag particles, decrease. In other word, surface plasmons cannot be excited at many more conditions of the incident angle and wavelength in low population density than in high one.

In order to compare different types of data, simulation θ - λ_R maps, experimental θ - λ_R maps, and fluorescence images for two samples coated with 20-fold diluted and undiluted AgNC@SiO₂ solutions are shown in Figures 3.22 and 3.23. Both FITC and RITC were added to the sample in order to clearly observe SPR dip signals and fluorescence images at a time. The spectral reflectance data were accumulated by scanning incident angles with 1° of difference from 40° to 60° or from 50° to 70°. The minimum reflectance dips in the experimental graphs are marked with circular yellow dots on the same positions of the calculated θ - λ_R maps in Figures 3.22(b) and 23(b) to compare with each other. One spectrum has one minimum reflectance dip and the dips accumulatively form one band in the each map in Figures 3.22(a) and 23(a). The experimental bands almost accord with bands in Figures 3.22(b) and 23(b). We can also confirm that the slope of the minimum reflectance band is steeper for the sample of the undiluted solution than 20-fold dilution while the bands commonly move toward a short wavelength as the incident angle increases. Figures 3.22(c)-(e) and 23(c)-(e) are corresponding fluorescence images of the sample at different points in the bands. Most of all, the fluorescence intensity is stronger in undiluted solution of AgNC@SiO₂ than 20-fold dilution because the mixed states of PSP and LSP are dominant and then the localized electromagnetic fields stimulate the fluorophores, such as FITC and RITC, around AgNC@SiO₂. Additionally, the steep slope of the band enables fluorophores to clearly emit their instinct color in a wide range of incident angles. The fluorescence wavelength can be changed from approx. 600 nm of red due to RITC at 57° to approx. 520 nm of green due to FITC at 51° in Figures 3.23(c)-(e), while it can be done at narrow angles between 44° and 42° in Figures 3.22(c)-(e).

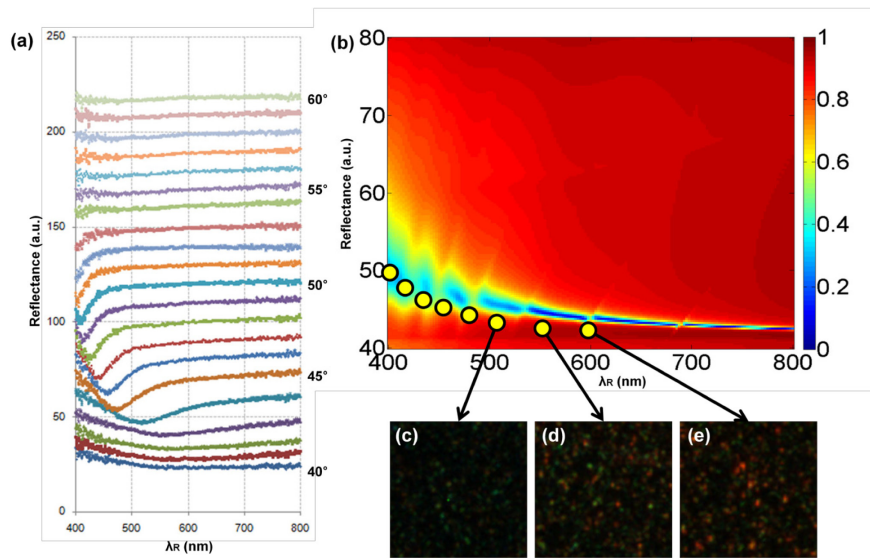


Figure 3.22. Comparison of three kinds of data for 20-fold dilution of AgNC@SiO₂ on Ag layer. They are (a) Experimental, (b) simulation θ - λ_R maps, and fluorescence images at (c) 44°, (d) 43°, and (e) 42°.

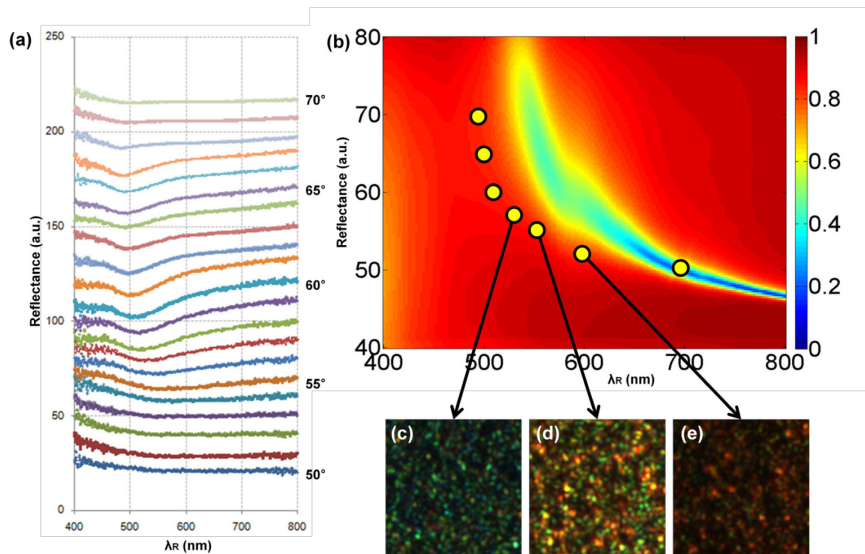


Figure 3.23. Comparison of three kinds of data for the undiluted AgNC@SiO₂ solution on Ag layer. They are (a) Experimental, (b) simulation θ - λ_R maps, and fluorescence images at (c) 57°, (d) 55°, and (e) 51°.

Finally, an example of applications is demonstrated in Figure 3.24. Using the steep slope of the minimum reflectance band, the fluorescent colors can be switched from red to green by changing the incident angle of white light. The fluorescence intensity is very weak and the colors are not clearly distinguished for only 50 nm Ag layer. However, when AgNC@SiO₂ are scattered on the Ag layer with few hundreds of inter-particle distances as homogeneous as possible, the fluorescence is able to have high intensity and the colors can be clearly changed from red to green. This switching technique can be usefully applied to bio sensors. For example, for a complex of plural molecules stained with different fluorophores, we can detect each molecule and highlight only a particular target molecule on the proposed structure by controlling an incident angle.

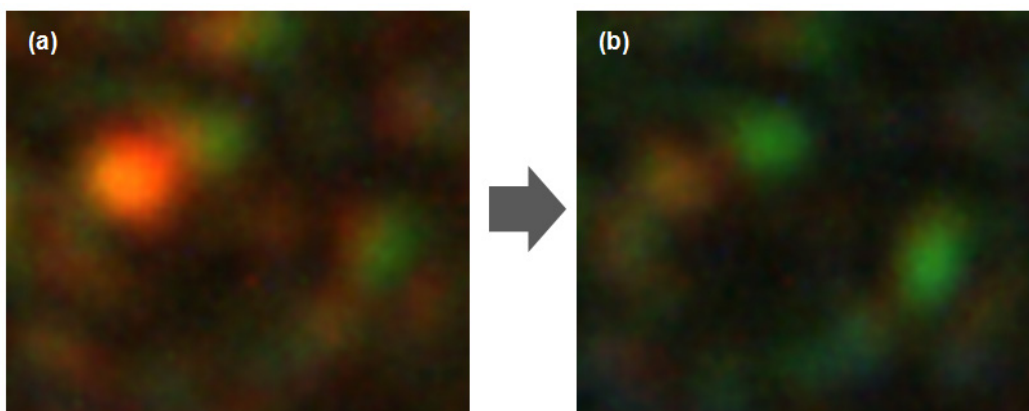


Figure 3.24. Switching the fluorescent colors from red to green depending on the incident angle from (a) 51° to (b) 57°.

3.4. Conclusion

In this research, a structure combined with metal nanoparticles and thin layer is suggested in order to simultaneously acquire SPR signals and fluorescence images based on plasmonic mixed states of PSPs and LSPs. The structure consists of AgNC@SiO₂

nanoparticles on Ag thin layer because LSPs are excited on metal nanoparticles and PSPs propagate on thin metal layer. Although PSP and LSP generally have conflicting properties, i.e. propagation and localization of surface plasmon, they can coexist as a form of the mixed states of PSP and LSP on the proposed structure. The mixed states can appear on either interspaces among AgNC@SiO₂ or SiO₂ gaps between AgNCs and Ag layer. As results of scanning structural parameters, such as inter-particle distance, core size, shell thickness, and layer thickness, to draw the θ - λ_R maps with the RCWA simulator, I found that slope of minimum reflectance band increases as AgNC@SiO₂ particles are close to each other. Decrease of AgNC diameter and SiO₂ shell thickness also give a slope to the band. Therefore, the slope of minimum reflectance band means the proportion of LSP to PSP in their plasmonic mixed states. This simulation results were confirmed by sequentially measuring spectral reflectance and fluorescence images of 30 nm AgNCs with 10 nm SiO₂ shell on 50 nm Ag layer at various incident angles. In particular, real distribution of inter-particle distances measured in experimental samples was fitted to the Weibull distribution and then the statistical data were fed back to calculation process. The recalculation results agreed with the experimental θ - λ_R maps and fluorescence images. This agreement implies validity of the simulation approach and the experimental method used to investigate the proposed structure.

The plasmonic mixed properties of PSP and LSP are useful in various practical applications such as bio sensors. For example, using steep slope of the minimum reflectance band, the fluorescent colors can be switched from red to green by changing incident angle of white light. This example shows promise in multi-detection for a complex of plural molecules stained with different fluorophores.

Chapter 4

Plasmonic intermediate states on AgNC@SiO₂ SAM

4.1. Concept: plasmonic intermediate states on AgNC@SiO₂ SAM

Recently, I began to pay attention to an existence of an intermediate state such as transitional, coexisting, hybrid, or metastable state between PSPs and LSPs because an intermediate state between major states usually has a high probability to have the dual properties of both sides. From nature, we can find a similarity to the phenomenon as well as a clue to an unknown intermediate state of surface plasmons. Most natural materials are consisted with different phases. For examples, the Gutenberg discontinuity exists between the lower mantle, which is considered as solid phase, and the outer core, which is inferred liquid phase, in the Earth's interior. When seismic waves pass the intermediate layer, P wave decreases sharply in velocity while S wave disappears completely because the medium phase changes from solid to liquid [98, 99]. Supercritical fluid is also a substance between liquid and gas phase so that it can diffuse through solid like gas and dissolve materials like liquid [100]. It has been significantly used in chemical extractions, decompositions, and reactions because of the intermediate properties. Although liquid crystal and semiconductor are artificial materials, they also play important roles of switching on-off in active electronic devices. Having a similar perspective, we can expect

a structure where an intermediate state between PSPs and LSPs can be excited.

I could find the intermediate state and the unique plasmonic property between PSPs and LSPs by minutely tuning a gap between nano-scale metal cubic unit structures and changing incident angle of light, as supercritical fluids can be formed by controlling the distance and momentum of the molecules above the critical pressure and temperature. First of all, I supposed that thin metal layer is a lattice array of metal cubic units. On the assumption, the structure without gap between the metal cubic units becomes a continuous metal layer so that PSPs are excited on the surface in Kretschmann configuration, while the structure with large gap becomes a sparse array of metal nanocubes so that LSPs are excited on the structure. Therefore an unfound plasmonic intermediate state between PSPs and LSPs may exist on the structure with a certain gap between the metal units. The changes of surface plasmon states can be analyzed by tracing a spectral reflectance and an electromagnetic field profile on the structure during scanning both a gap between units and an incident angle of light. In particular, the proposed structure can be approximately built with silver nanocubes with silicon dioxide shell ($\text{AgNC}@\text{SiO}_2$) in experiment though a nanofabrication for few nanometer scales is impracticable in current lithography techniques. I could, finally, acquire the evidence for the plasmonic intermediate state through simulation and experiment, so that each result can be matched with each other after a statistical feedback.

A structure on which I investigate the intermediate state between PSPs and LSPs is a lattice array of cubic units which are metal cubic cores with dielectric shell. As shown in Figure 4.1(a), while the structure is a continuous metal layer when the shell thickness is zero, the increase of shell thickness transforms it into a discontinuous lattice array of metal cubes with dielectric gap. It is only PSPs to be excited on the metal layer without shell and it is oppositely only LSPs to exist on the array with a wide dielectric gap. Therefore, we can trace a kind of transition from PSPs to LSPs and find an intermediate state between them by minutely increasing the shell thickness from zero. Silver (Ag) was selected as the metal materials because surface plasmon can propagate in the longest distance and silicon dioxide (SiO_2) was selected as dielectric materials because it is suitable for synthesis of shell in experiment. Reflectance spectra at various incident

angles, which can be converted into incident angle versus wavelength of reflectance graph (θ - λ_R map), should be calculated and measured to confirm the excitation of surface plasmons in the Kretschmann configuration. The data can be appropriate values to represent the excitation of surface plasmons because light absorption to excite surface plasmon causes a decrease of reflectance at the interface between a metal structure and a prism in total internal reflection (TIR) condition and the Kretschmann configuration has been also verified as classical experimental method in plasmonics for a long time. Therefore, the changes of θ - λ_R map will represent an alteration of surface plasmon state on the transformed structure.

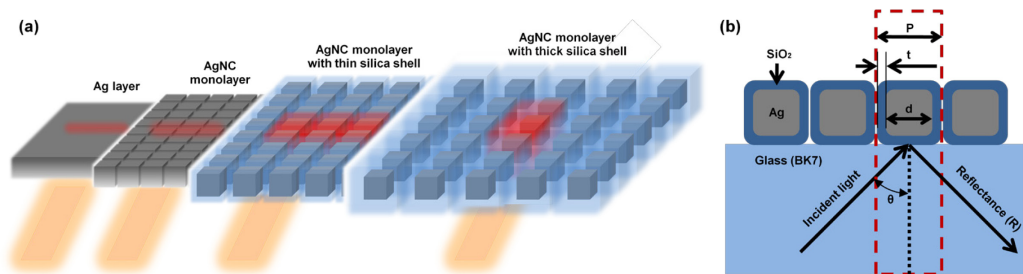


Figure 4.1. (a) Concept image of plasmonic intermediate state between PSPs and LSPs on a lattice array of the cubic units. (b) Structure and parameters used in simulation. One period includes one cubic unit. P , d , t , θ , and R are period, core diameter, shell thickness, incident angle, and reflectance.

4.2. Simulation part

I calculated a series of reflectance at wavelengths from 400 nm to 800 nm and incident angles from 40° to 80° using RCWA simulation tool to make a θ - λ_R map for one fixed structure. Two-dimensional (2D) simulation was selected because it is more efficient in calculation time than three-dimensional (3D) calculation. It is also appropriate for

enormous calculations in minutely scanning an inter-core gap, incident angle, and wavelength. Additionally, when light illuminates to a cube monolayer in one direction on the perpendicular plane to the monolayer plane, it can be approximated to the case in which light goes through a monolayer of long rods with two square sides in short axis direction. Although 3D calculation can make a more exact θ - λ_R map than 2D calculation, I will demonstrate validity of 2D simulation by comparing the calculated results with experimental data later. Figure 4.1(b) shows the structure and variables used in simulation.

As results of the simulation, the intermediate states of PSPs and LSPs are found in the narrow region, such as 25 - 50 nm of core diameters and 0 - 10 nm of shell thicknesses. In particular, the optimized θ - λ_R map is acquired when the diameter of Ag core is 35 nm and the thickness of SiO₂ shell is 2 nm as shown in Figure 4.2(b). For comparison, the representative θ - λ_R maps for PSP and LSP states are in Figures 4.2(a) and (c). The map of Figure 4.2(a) is calculated for 35 nm of Ag thin layer, which is same as the monolayer of only Ag core units without SiO₂ shell, and the map of Figure 4.2(c) is from the array of Ag cores with 70 nm of distance, which is same as monolayer of units with 35 nm of Ag core diameter and 17.5 nm of SiO₂ shell thickness. As known already and generally, they have only one minimum reflectance band in each θ - λ_R map. The map of Figure 4.2(a) shows one diagonal band (D-band) because a resonance wavelength of PSPs depends on an incident angle of light, while the map of Figure 4.2(c) shows an incident angle-independent vertical band (V-band) because a resonance wavelength of LSPs does not depend on an incident angle of light but a shape and size of Ag core unit: the reflectance at an incident angle under 61.3° is almost zero in Figure 4.2(c) because light penetrates wide dielectric gaps at an incident angle under the critical angle of TIR. In contrast, the map of Figure 4.2(b) shows two minimum reflectance bands. It seems intuitively that they are hybridized from intercrossing D- and V-bands. In addition, I selected the environmental refractive index 1.33 of water because most intercrosses of D- and V-bands clearly appear under that condition. The corresponding θ - λ_R maps for refractive index of air are shown in Figures 4.2(d)-(f).

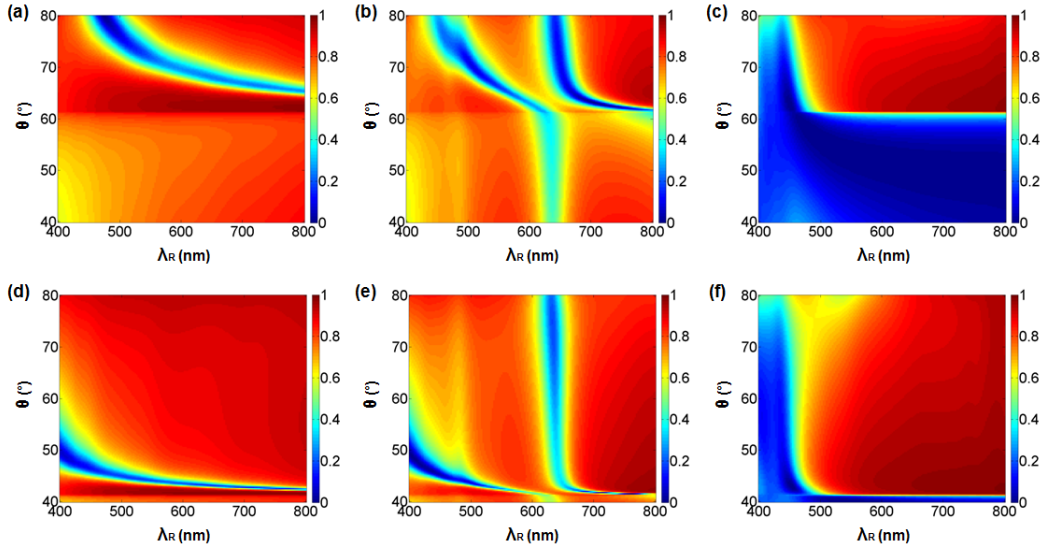


Figure 4.2. θ - λ_R maps of (a) AgNC (35 nm) with shell (0 nm), (b) AgNC (35 nm) with shell (2 nm), and (c) AgNC (35 nm) with shell (17.5 nm). There are (a) D-band, (b) two hybrid bands, and (c) V-band. (d)-(f) θ - λ_R maps of structures corresponding to (a)-(c) for an environmental refractive index of 1.00.

4.2.1. Intermediate states of PSPs and LSPs

I calculated H_y -field profiles at seven distinguishing points in two bands on the θ - λ_R map of Figure 4.4(a), which is brought from Figure 4.2(b) for convenience, in order to investigate the intermediate states in detail. The corresponding H_y -field profiles for the θ - λ_R maps of Figures 4.2(a) and (c) are also shown in Figure 4.3 as the reference data for PSP and LSP state. Firstly, considering the H_y -field profile in Figure 4.4(b), surface plasmons are propagating as PSP state on the structure because the incident light perceives the array of Ag cores as a quasi-continuous Ag layer under the condition of 508 nm wavelength and 70° incident angle. However, as incident angle decreases and

wavelength increases, the electromagnetic field is gradually confined and finally turned into LSP state at the gaps between Ag cores, as shown in Figures 4.4(c) and (d). Considering H_y -field profiles of LSP state, there is a difference in Figure 4.4(d) and Figure 4.3(d): the former is LSP in gap between Ag cores because the cores are close to each other and the latter is LSP at top and bottom of Ag cores because they are apart from each other. Secondly, in the right band, the H_y -field profile at 70° of incident angle and 652 nm of wavelength in Figure 4.4(f) is analogous to that in not Figure 4.4(b) but Figure 4.4(d), which is LSP state. The electromagnetic field slowly changes into PSP state as an incident angle decreases and a wavelength increases in Figures 4.4(f)-(h). Namely, state of surface plasmon on the same structure is changing in the opposite directions depending on an incident angle and wavelength. The left band may exist as a form connected by the left part of the D-band due to PSPs and the lower part of the V-band due to LSPs, while the right band may have a shape linked by the higher part of the V-band due to LSPs and the right part of the D-band due to PSPs.

I am interested in the cross point of the D- and V-bands on the θ - λ_R map in Figure 4.4(a) and surmise that the H_y -field profile in Figure 4.4(e) may represent for a plasmonic state of the cross point. LSPs do not exist at gaps between Ag cores and the phases of two surface plasmon states on top and bottom of the array structure are opposite to each other. Comparing the θ - λ_R maps of Figures 4.4(c) and (g), which are located at antipodes with the cross point as a center, the phases of PSPs on surface are reversed while the phases of LSPs at gaps are kept. In other words, the cross point is a kind of a metastable state as a saddle point. Sudden changes in both a phase of PSP and an existence of LSP occur around the cross point on the proposed structure. The sudden changes of PSP and LSP bring about interference between two different states. The phases of PSP and LSP are same so that an intensity of H_y -field increases and the reflectance decreases in Figure 4.4(g), while the phases of PSP and LSP are opposite so that an intensity of H_y -field decreases and the reflectance increases in Figure 4.4(c). Namely, the former comes from a constructive interference of PSPs and LSPs and the latter comes from a destructive interference of them. While PSP state survives and propagates as a result of interference because the intensity of PSP under a PSP excitation condition is stronger than that of LSP

in Figure 4.4(b), LSP state survives and propagates because the intensity of LSP under a LSP excitation condition is stronger than that of PSP in Figure 4.4(f). Previous researches have reported that LSPs can propagate along a chain of nanoparticles with a narrow gap [101-103].

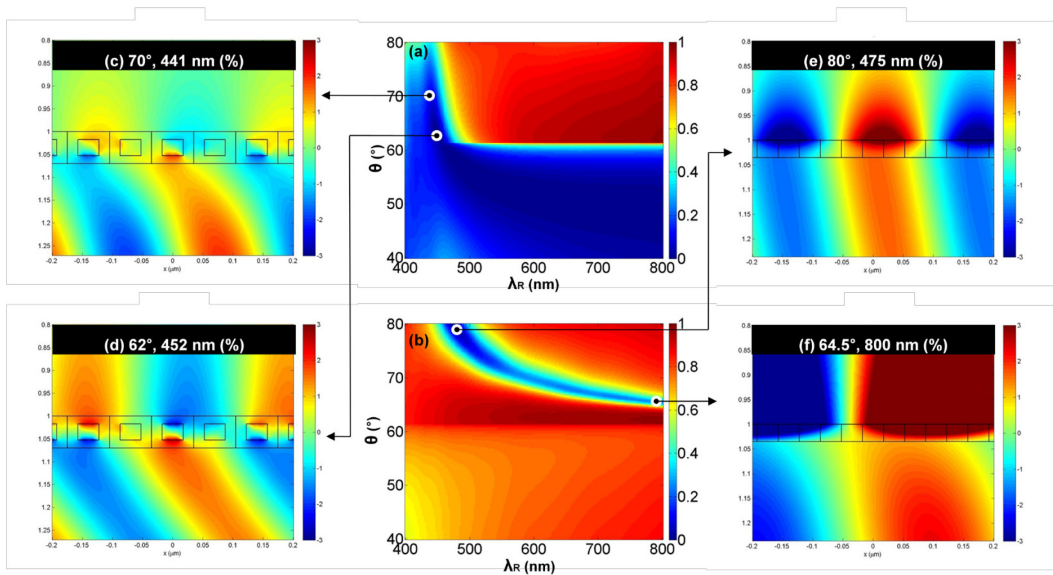


Figure 4.3. θ - λ_R maps of (a) AgNC (35 nm) with shell (17.5 nm) and (b) AgNC (35 nm) with shell (0 nm). H_y -field profiles at θ and λ_R of (c) 70° and 441 nm in (a), (d) 62° and 452 nm in (a), (e) 80° and 475 nm in (b), (f) 64.5° and 800 nm in (b).

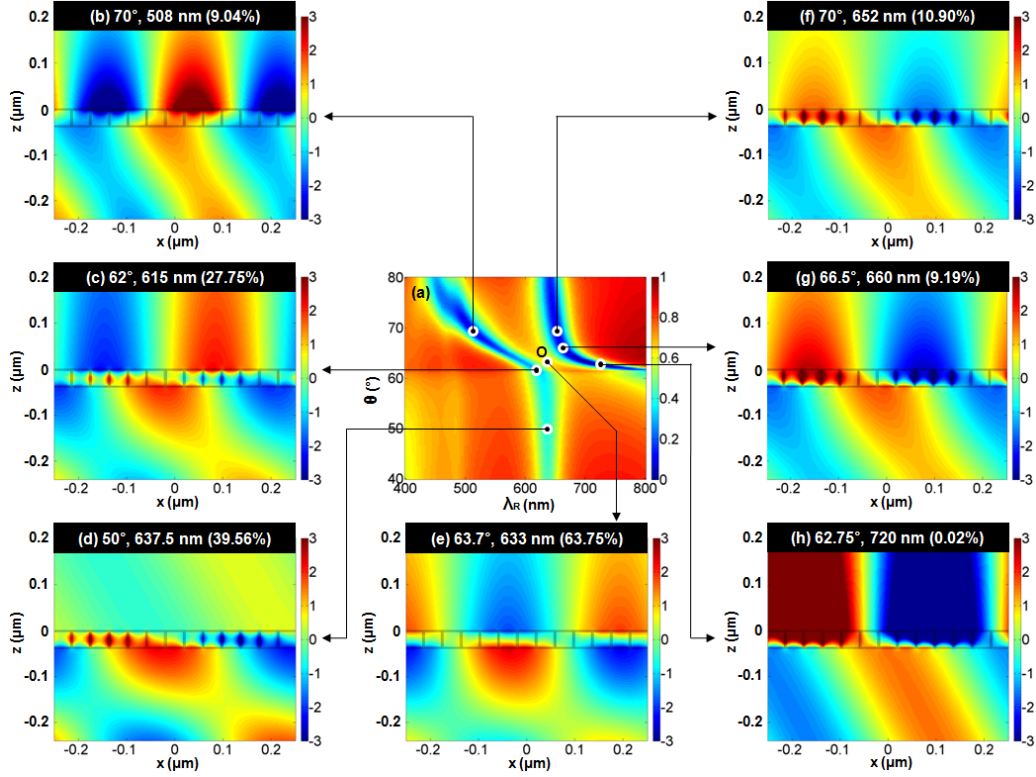


Figure 4.4. (a) θ - λ_R map of AgNC (35 nm) with shell (2 nm) and H_y -field profiles at θ and λ_R of (b) 70° and 508 nm (c) 62° and 615 nm, (d) 50° and 637.5 nm, (e) 63.7° and 633 nm, (f) 70° and 652 nm, (g) 66.5° and 660 nm, and (h) 62.75° and 720 nm. (b)-(d) show transition from PSP to LSP and (f)-(h) show a transition from LSP to PSP. H_y -field profile of (e) shows a metastable state at a saddle point, O , on the θ - λ_R map of (a).

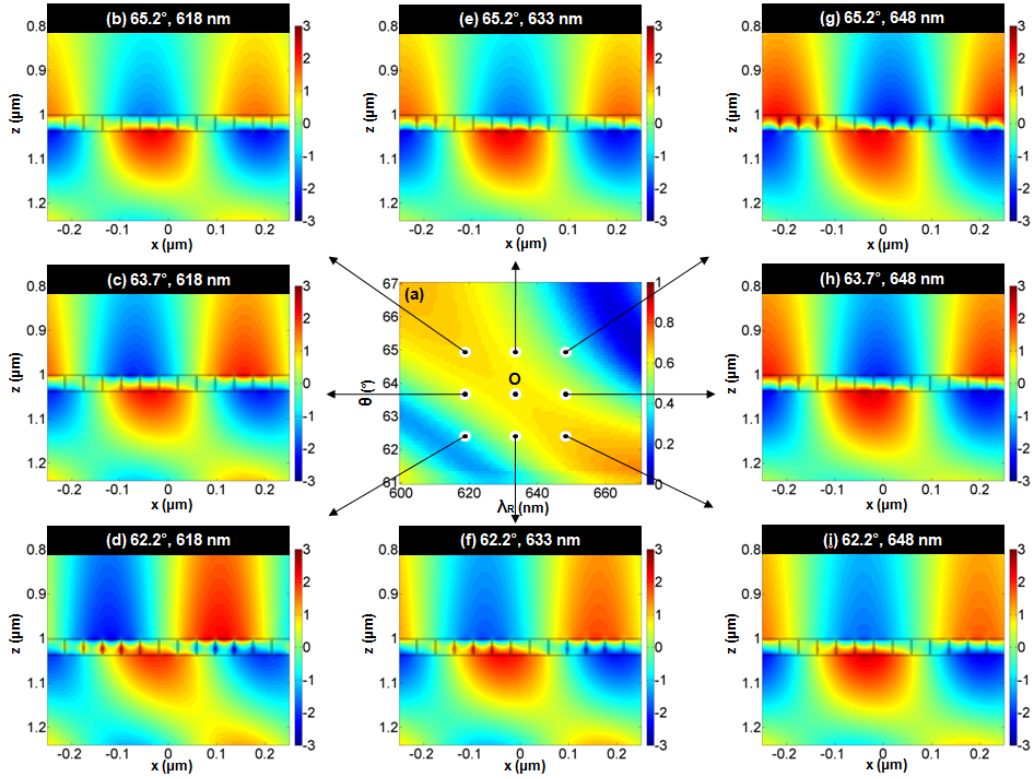


Figure 4.5. H_y -field profiles around the cross point or saddle point, O , on a θ - λ_R map for the lattice array of AgNC (43 nm) with shell (3.5 nm).

4.2.2. Effect of structural parameters on two minimum reflectance bands

A position and intensity of two bands on a θ - λ_R map can be freely controlled by tuning Ag core diameter and SiO₂ shell thickness because they are main factors which can decide the balance or interaction of PSP and LSP states as shown in Figure 4.6. A shell thickness primarily influences the position of the V-band (Figure 4.6(a)) and a core

diameter mainly influences the balance of the D- and V-band intensities (Figure 4.6(b)). In terms of a shell thickness, PSP state on Ag core array without shell slowly turns into an intermediate state of PSP and LSP in the narrow region of shell thicknesses 0 nm - 8 nm, and then completely changes into LSP state when a shell thickness becomes above 8 nm. The V-band specially moves toward a short wavelength as a shell is thickening because the thick shell put the cores apart from each other and the number of Ag cores covered by LSP resonance wavelength decreases [17]. We can confirm that many more Ag cores participate in a resonance wavelength of LSP at either a narrow gap or a long wavelength than at either a wide gap or a short wavelength in Figure 4.7. In terms of core size, for large cores with diameter over 60 nm, PSP excitation efficiency becomes very low so that the D-band intensity is weakened: PSP can be effectively excited at 40 - 60 nm of Ag layer thicknesses in the Kretschmann configuration [6-8] and the V-band due to LSP relatively has a high intensity and moves forward a long wavelength because incident light can recognize the large cores as more discontinuous particles than small cores.

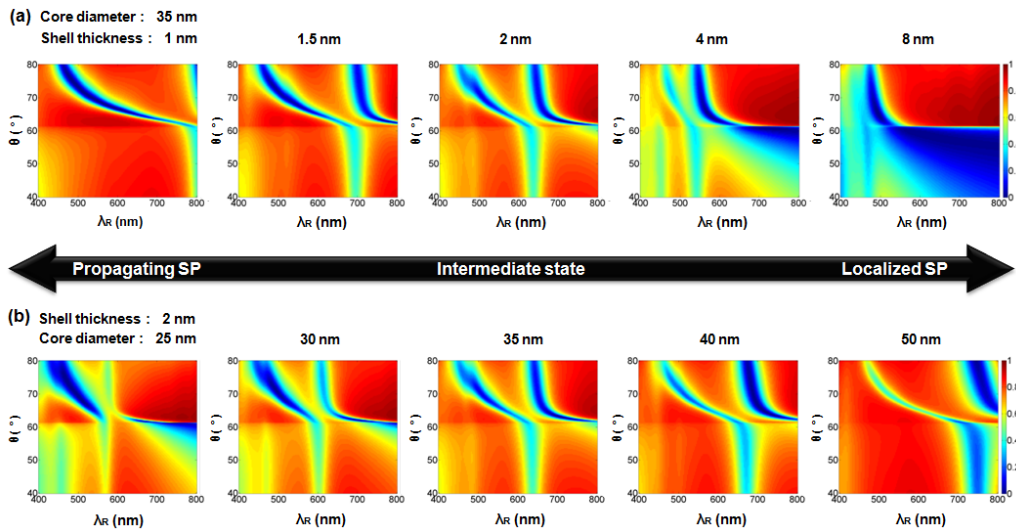


Figure 4.6. Effect of (a) shell thickness and (b) core diameter on two hybrid bands of θ - λ_R map.

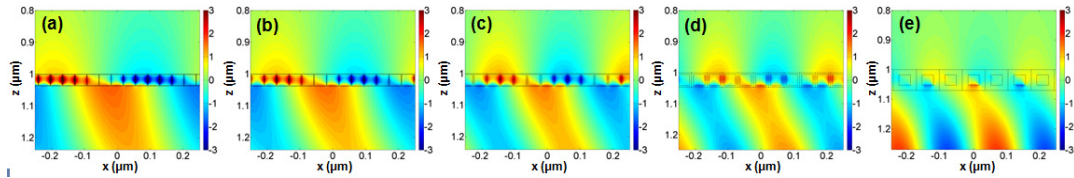


Figure 4.7. H_y -field profiles of AgNC (35 nm) with shell thickness (t) at 70° and λ_R . t and λ_R are (a) 1 nm and 813 nm, (b) 1.5 nm and 704 nm, (c) 3 nm and 582 nm, (d) 6 nm and 495 nm, and (e) 17.5 nm and 437 nm.

4.3. Experiment

4.3.1. Chemical fabrication and optical measurement

Preparation of AgNC@SiO₂ solution is the same as that in Section 3.3.1 and optical measurement of them is also the same as that in Section 3.3.2 of Chapter 3.

Preparation of AgNC@SiO₂ self-assembled monolayer (SAM): A clean Petri dish filled with deionized water was used for the entire process of monolayer film formation. The AgNC@SiO₂ solution was dropped onto the water surface. Once the monolayer film was formed at an interface between air and water, glass substrate was attached onto the water surface to transfer the monolayer film.

4.3.2. Results and discussion

According to the simulation results, unit structures of several tens nanometer scales should have a tiny gap of few nanometers between them in order to experimentally ascertain an existence of two bands in a θ - λ_R map. However, carving a straight line of few nanometers on a metal layer is impossible because the minimum line width of current lithography techniques is about 30 nm [104]. Therefore I attempted to build the proposed structure with cubic structure units because bottom-up methods can provide opportunities of manufacturing materials in a few nanometer scales. Ag nanocubes (AgNC) were selected as the cubic structure units of an Ag layer in this experiment because cubic structures have a geometric advantage in forming a monolayer of a lattice array: they can contact face to face with each other or between cubes and a substrate so that they can be assembled with a higher population density than other shaped structures even if they are randomly scattered on a substrate. They were synthesized with the polyol method [88-90] and enclosed with SiO₂ shell in the stöber process [91-93]. A monolayer of AgNC with SiO₂ shell (AgNC@SiO₂) was prepared by the self-assembled monolayer (SAM) method which is using differences in solubility and surface tension of water and organic solvents where AgNC@SiO₂ are dispersed [105-107]. As shown in Figures 4.8(a) and (b), AgNC@SiO₂ has approx. 43 nm of core and 3.5 nm of shell in the TEM image and they are settled into a monolayer with a high population density in the SEM image. We can confirm that most cubes contact face to face with each other on a substrate. In order to compare with the monolayer of AgNC@SiO₂, SEM images of partial monolayer and multilayer of the nanocubes are shown in Figures 4.8(c) and (d). Although the nanocubes are packed tighter in Figures 4.8(c) and (d) than Figure 4.8(b), they are not complete monolayers. The monolayer unavoidably has a certain distribution of the inter-particle gaps. The spectral reflectance of the sample was obtained with a spectrometer at several incident angles using a white light source in the TIR geometry.

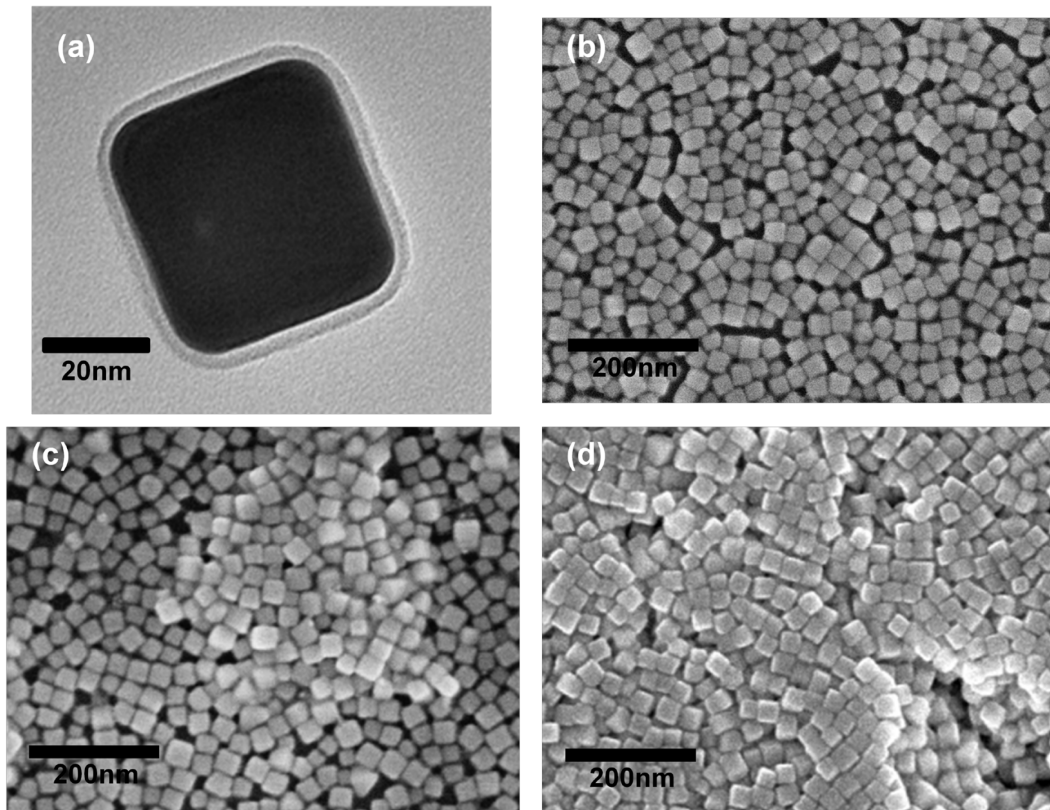


Figure 4.8. (a) TEM image of AgNC@SiO₂ (43 nm / 3.5 nm). SEM images of (b) monolayer, (c) partial monolayer, and (d) multilayer of AgNC@SiO₂. Scale bars are (a) 20 nm and (b)-(d) 200 nm.

Three measured results are shown in Figure 4.9 with the corresponding simulation θ - λ_R maps. The samples are a 43 nm Ag layer evaporated on glass in Figures 4.9(a) and (d), an AgNC@SiO₂ SAM with 43 nm core and 3.5 nm shell on glass in Figures 4.9(b) and (e), and an AgNC@SiO₂ randomly scattered on glass without face-to-face contact in Figures 4.9(c) and (f), respectively. The spectral reflectance data are accumulated by scanning incident angles with a difference of 1° from 60° to 75°. The minimum reflectance dips in the experimental graphs are marked with circular black dots on the same positions of the θ - λ_R maps in Figures 4.9(d), (e), and (f) to compare with each other. For reference, they are the results for an environmental refractive index 1.33 of water and

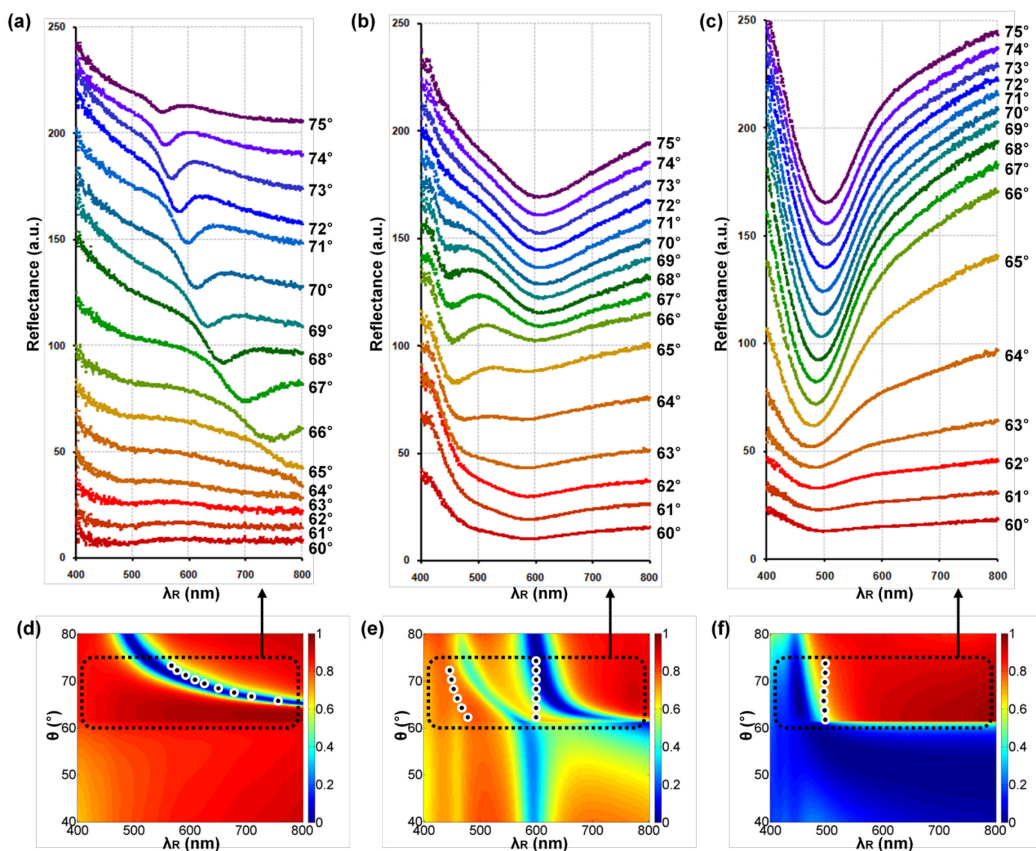


Figure 4.9. (a)-(c) Experimental and (d)-(f) calculated θ - λ_R maps for (a) and (d) AgNC (43 nm) with shell (0 nm), (b) and (e) AgNC (43 nm) with shell (3.5 nm), and (c) and (f) AgNC (43 nm) with shell (21.5 nm). The positions of dips on the experimental maps of (a)-(c) are marked with circular black dots at the same positions on the simulation maps of (d)-(f). The whole regions in the experimental maps are denoted by dotted boxes on the simulation maps.

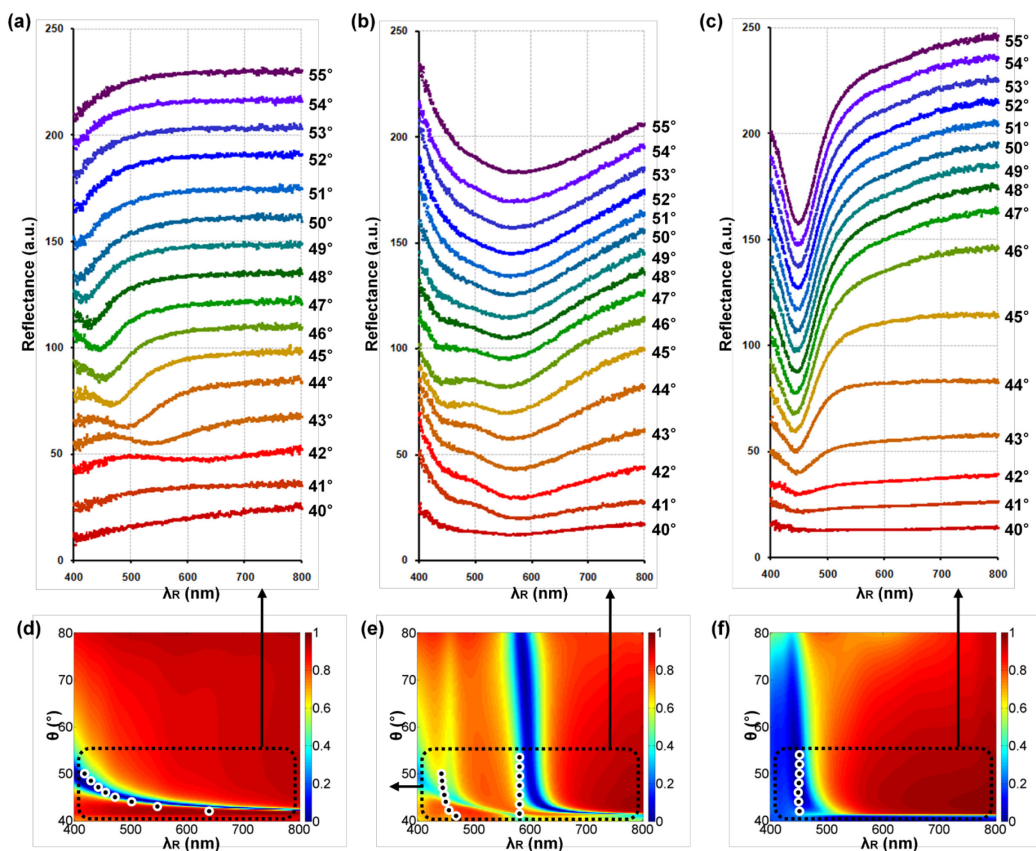


Figure 4.10. For an environmental refractive index of 1.00 (air), (a)-(c) experimental and (d)-(f) calculated θ - λ_R maps for (a) and (d) AgNC (43 nm) with shell (0 nm), (b) and (e) AgNC (43 nm) with shell (3.5 nm), and (c) and (f) AgNC (43 nm) with shell (21.5 nm). The positions of dips on the experimental maps of (a)-(c) are marked with circular black dots at the same positions on the simulation maps of (d)-(f). The whole regions in the experimental maps are denoted by dotted boxes on the simulation maps.

the corresponding results for a refractive index of air are shown in Figure 4.10. One spectrum has one minimum reflectance dip and the dips accumulatively form one band in each map in Figures 4.9(a) and (c). The bands almost accord with both the D-band due to PSP and the V-band due to LSP in Figures 4.9(d) and (f). On contrary to those, there are two dips in one spectrum and two accumulated bands on the experimental θ - λ_R map in Figure 4.9(b). As an incident angle increases, one band near 460 nm moves toward a short wavelength while the other band near 600 nm keeps its position. The experimental θ - λ_R map in Figure 4.9(b) can be an evidence for an existence of an intermediate state between PSP and LSP because the number, position, and shift tendency of the bands are similar to the calculated θ - λ_R map in Figure 4.9(e).

We can reduce the differences between the experimental and calculated θ - λ_R maps by feeding back statistical data for a gap distribution of AgNC@SiO₂ SAM to the prior simulation. The SAM has certain distributed gaps between the units in a real sample while the units are located at exact lattice points with the same gap in a simulation condition. The limitation of the SAM method brings about differences between them: for example, two bands of Figure 4.9(c) are placed at a shorter wavelength than those of Figure 4.9(d) and the slop of the left band is different in between Figures 4.9(c) and (d). In order to solve the problem, I measured the gaps between Ag cubic units in the sample and then calculated an average and standard deviation of the gap distribution with statistical method. Random numbers were generated in the normal distribution with the statistical values and then fed back to calculation condition after confirming that the measured gap data follow a normal distribution through a test of normality.

The gap distribution measured from SEM image of Figure 4.8(b) is shown in Figure 4.11(a). The average of gaps was 49.3 nm and the standard deviation was 7.47 nm. One hundred of random numbers were generated as the distribution chart in Figure 4.11(b) and inputted into the simulation condition as the schematic diagram in Figure 4.11(c). Namely, one hundred of cubic units randomly and normally distributed in one period were calculated. The recalculated θ - λ_R map is demonstrated in Figure 4.11(f) with the initial calculated map in Figure 4.11(d) and the experimental map in Figure 4.11(e) for comparison. When the gap distribution is applied to the simulation condition, two bands

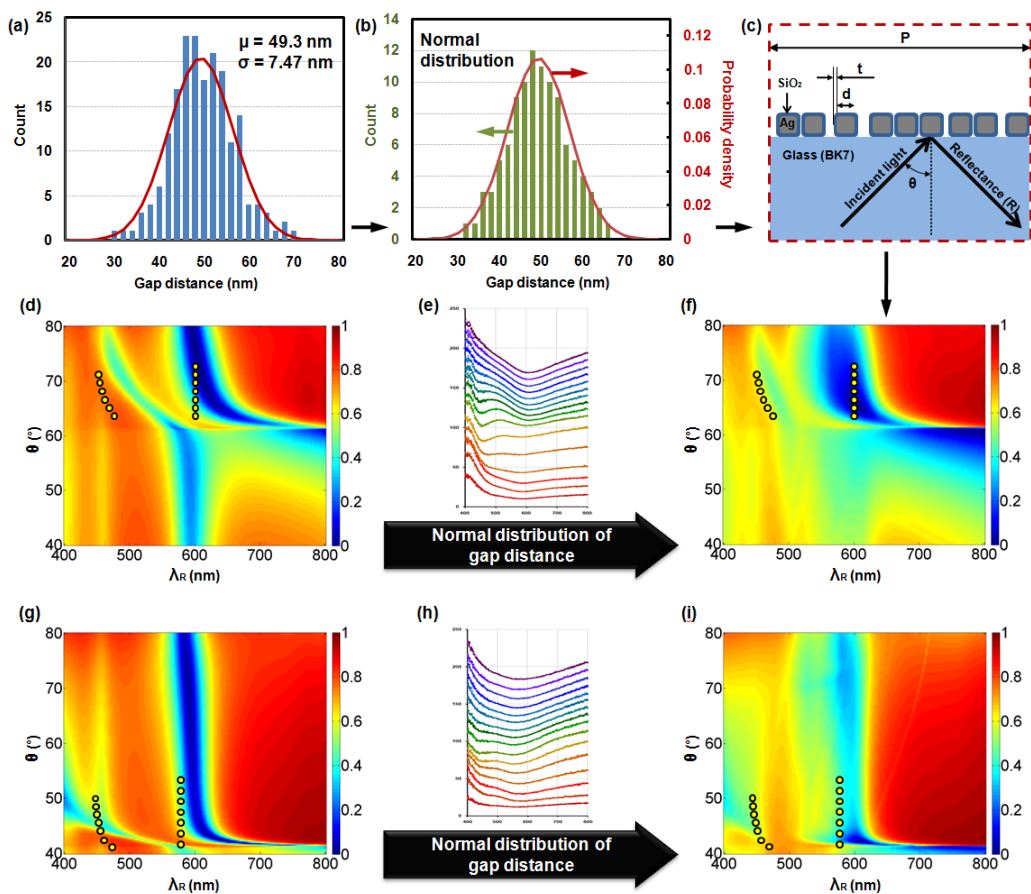


Figure 4.11. (a) Gap distribution of AgNC@SiO₂ in sample. The average gap distance is 49.3 nm and standard deviation is 7.47 nm. (b) Randomly generated gap distribution with normality. (c) Simulation condition. One period includes one hundred of randomly distributed cubic units with normality. P , d , t , θ , and R are period, core diameter, shell thickness, incident angle, and reflectance. (d) Initial calculated, (e) experimental, and (f) recalculated θ - λ_R maps. Positions of dips on the experimental map in (e) are marked with yellow open circles at the same positions on simulation maps of (d) and (f). For environmental refractive index of 1.00 (air), (g) Initial calculated, (h) experimental, and (i) recalculated θ - λ_R maps. Positions of dips on the experimental map in (h) are marked with yellow open circles at the same positions on simulation maps of (g) and (i)

become broad and the reflectance increases a little while overall tendency of θ - λ_R map is kept. In particular, a blue-shift of the left band is bigger than that of the right band because a short wavelength of light can distinguish the variation of the unit distribution more than a long wavelength can. The experimental θ - λ_R map consequentially became closer to the θ - λ_R map in Figure 4.11(f) than that in Figure 4.11(d) through the statistical treatment. The similarity between the experimental and calculated graphs can give a validity of two-dimensional simulation at least in this case though a nanocube monolayer is three-dimensional structure.

4.4. Conclusion

I found the plasmonic intermediate state between PSP and LSP on the lattice array of metal nanocubes with few nanometer gaps in simulation and proved the existence and the properties by using both the pseudo-lattice array of AgNC@SiO₂ SAM in experiment and a feedback of gap distribution to calculation in statistics. The intermediate state has two distinguishing bands on θ - λ_R map on contrary to PSP or LSP state which has only one band (D- or V-band) on the map. Changes of H_y -field profiles in the bands demonstrate the reversal transition between PSP and LSP in each other band. The cross point of the D- and V-bands becomes a metastable state where the phase of PSP turns opposite and LSP instantly vanishes at gap so that a breakage of PSP phase equilibrium, a sudden discontinuity of LSP, and a rapid changes of reflectance occur around the cross point. They can be enough evidences to infer that the two bands may be hybridized from an intercross of the D- and V-bands on θ - λ_R map. I acquired the experimental θ - λ_R map of the plasmonic intermediate stat and confirmed the two hybrid bands by measuring the pseudo-lattice array, AgNC@SiO₂ SAM. Additionally, the feedback of statistical data from experiment to simulation enabled the recalculated θ - λ_R map to come close to the experimental results. Those can support both the validity of 2D simulation for lattice

array of nanocubes and the experimental substantiation for the plasmonic intermediate state predicted with the simulation.

Although I made AgNC@SiO₂ SAM with bottom-up method as similar to the proposed structure as possible, spectrum dips were so broad that only identification of two hybrid bands and confirmation of their spectral shift were possible. It is due to distribution in size and position of nanocubes as unsolved limitations of the method. However, the structure cannot be perfectly made in current technology: even though lithography can make an accurate lattice structure in several tens of nanometer scale at least, it cannot carve line with width of few nanometers owing to limit of minimum line width in current lithography. It is, therefore, meaningful research that the plasmonic intermediate state is found and proved in both simulation and experiment though it can be observed in only the very narrow windows of gap distance between cubic units.

Although a few nanometer gap cannot be realized yet with neither of top-down nor bottom-up process in current technology, the plasmonic intermediate on the proposed structure will clearly show the distinguishing property if an innovative process for the nanofabrication is developed in future. The plasmonic intermediate properties, which include the existence of multiple minimum reflectance bands, the control of two minimum reflectance bands, the metastable state at the cross point of PSP and LSP, and the sudden change of properties near the cross point, are very valuable in various future technologies as liquid crystal and semiconductor technologies in current industry.

Chapter 5

Conclusion

This dissertation demonstrated chemical fabrication of metal/dielectric nanoparticle arrays and optical analysis of their surface plasmon couplings in three major parts as above.

In the first part of this thesis, I suggested a new chemical method called site-selective synthesis, which enables to synthesize and align silver (Ag) nanoparticles simultaneously in a designed trench. Ag nanoparticles can be nucleated and grown, not on a hydrophobic fluorosilane-coated surface, but in a hydrophilic polyvinylpyrrolidone-rich trench. Using this new method, a sample of Ag nanoparticle arrays was prepared and its plasmonic scattering property was measured as a function of an angle and polarization of incident light in the configuration of total internal reflectance. Therefore, this research shows not only the improvement of process efficiency but also the possibility of an array design for a plasmonic structure.

In the second part, a structure combined with metal nanoparticles and thin layers is suggested to acquire SPR signals and fluorescence images simultaneously based on the coupling of PSPs and LSPs. Although PSPs and LSPs generally have conflicting properties, i.e. propagation and localization of surface plasmon, they can coexist as a form of coupling PSP and LSP on AgNC@SiO₂ on the Ag thin layer. A slope of the minimum reflectance band on the θ - λ_R map increases as an inter-particle distance, core diameter, and shell thickness decrease. Therefore, the band slope means the proportion of LSP to PSP in their plasmonic coupling. In particular, when the Weibull distribution of inter-particle distances was fed back to the simulation, the recalculation results accorded

with the experimental θ - λ_R maps and fluorescence images. This agreement implies the validity of the simulation approach and the experimental method used for investigating the proposed structure. This distinguishing plasmonic coupling property will be useful in various practical applications such as bio sensors.

In the third part, I found the plasmonic intermediate state between PSPs and LSPs on the pseudo-lattice array of AgNC@SiO₂ SAM through a simulation, experiment, and feedback of gap distribution to calculation. The intermediate state has two distinguishing bands on the θ - λ_R map on the contrary to PSP or LSP states which have just one band (D- or V-band) on the map. Changes of H_y -field profiles in the bands demonstrate a reversal transition between PSPs and LSPs in each other's band. The cross point between the D- and V-bands becomes a metastable state so that a breakage of PSP phase equilibrium, a sudden discontinuity of LSP, and rapid changes of reflectance occur around that point. This study, which is focused on the plasmonic intermediate state, will become a bridgehead for the simultaneous use of PSPs and LSPs in order to improve their plasmonic property in one device.

As described above, the three main parts were sequentially conducted in this research from a new fabrication method of metal nanoparticle arrays to various propagating, localized, and their coupled surface plasmons excited on metal nanoparticle arrays. This study provides a further understanding of systems based on metal nanoparticle arrays. From a practical point of view, it may open the way to the engineering in a controllable and predictable way of the spectral properties of metal nanoparticle-based systems to reinforce their applicability especially in sensing and surface enhancement Raman scattering. The plasmonic mixed state of PSP and LSP will show promise in multi-detection of SPR signals and fluorescence images for a complex of plural molecules stained with different fluorophores. Furthermore, the plasmonic intermediate and metastable state will open new opportunities to control PSP and LSP in active plasmonic devices in future. In order to conduct this research, chemical, and optical approaches are used in the preparation of samples, measurement of plasmonic properties, and simulation analysis of results. This complex approach is expected to be a model of interdisciplinary research.

Bibliography

- [1] H. S. Redgrove, "Alchemy ancient and modern," (William Rider & Son. Ltd, 1922).
- [2] A. G. Debus, "Alchemy and early modern chemistry," (Jeremy Mills Publishing, 2004).
- [3] A. Greenberg, "From alchemy to chemistry in picture and story," (Wiley-Interscience, 1st edition, 2007).
- [4] E. Hecht, "Optics," (Addison-Wesley, 4th edition, 2002).
- [5] J. C. Maxwell, "A dynamical theory of the electromagnetic field," *Philosophical Transactions of the Royal Society of London* **155**, 459-512 (1865).
- [6] H. Raether, "Surface plasmons on smooth and rough surfaces and on gratings," (Springer-Verlag, Berlin, 1988).
- [7] S. A. Maier, "Plasmonics: fundamentals and applications," (Springer, United Kingdom, 2007).
- [8] M. L. Brongersma and P. G. Kik, "Surface plasmon nanophotonics," (Springer, 2007).
- [9] Y. Xia and N. J. Halas, "Shape-controlled synthesis and surface plasmonic properties of metallic nanoparticles," *MRS Bull.* **30**, 338–344 (2005).
- [10] D. J. Campbell and Y. Xia, "Plasmons: why should we care?," *J. Chem. Educ.* **84**, 91–96 (2007).
- [11] M. O. Marder, "Condensed matter physics," (John Wiley & Sons, Inc, New York, 2000).
- [12] Y. A. Illinskii and L.V. Keldysh, "Electromagnetic response of material media," (Plenum Press, New York, 1994).

- [13] S. Linic, P. Christopher, and D. B. Ingram, "Plasmonic-metal nanostructures for efficient conversion of solar to chemical energy," *Nat. Mater.* **10**, 911–922 (2011).
- [14] B. T. Draine and P. J. Flatau, "Discrete-dipole approximation for scattering calculations," *J. Opt. Soc. Am.* **11**, 1491–1499 (1994).
- [15] W. H. Yang, G. C. Schatz, and R. P. Van Duyne, "Discrete dipole approximation for calculating extinction and Raman intensities for small particles with arbitrary shapes," *J. Chem. Phys.* **103**, 869–875 (1995).
- [16] X. Lu, M. Rycenga, S. E. Skrabalak, B. Wiley, and Y. Xia, "Chemical synthesis of novel plasmonic nanoparticles," *Annu. Rev. Phys. Chem.* **60**, 167–192 (2009).
- [17] W. Rechberger, A. Hohenau, A. Leitner, J. R. Krenn, B. Lamprecht, and F. R. Aussenegg, "Optical properties of two interacting gold nanoparticles," *Opt. Comm.* **220**, 137 (2003).
- [18] British Museum. Lycurgus cup. <http://www.britishmuseum.org>, 2008.
- [19] E. Kretschmann and H. Reather, "Radiative decay of nonradiative surface plasmon excited by light," *Z. Naturf.* **23A**, 2135 (1968).
- [20] A. Otto, "Excitation of nonradiative surface plasma waves in silver by the method of frustrated total reflection," *Z. Phys.* **216**, 398 (1968).
- [21] P. Nordlander and E. Prodan, "Plasmon hybridization in nanoparticles near metallic surfaces," *Nano Letter* **4**, 2209-2213 (2004).
- [22] W. R. Holland and D. G. Hall, "Frequency shifts of an electric-dipole resonance near a conducting surface," *Phys. Rev. Lett.* **52**, 1041-1044 (1984).
- [23] A. Leitner, Z. Zaho, H. Brunner, F. R. Aussenegg, and A. Wokaum, "Optical properties of a metal island film close to a smooth metal surface," *Appl. Opt.* **32**, 102-110 (1993).
- [24] J. Cesario, M. U. Gonzalez, S. Cheylan, W. L. Barnes, S. Enoch, and R. Quidant, "Coupling localized and extended plasmons to improve the light extraction through metal films," *Optics Express* **15**, 10533-10539 (2007).
- [25] N. Papanikolaou, "Optical properties of metallic nanoparticle arrays on a thin metallic film," *Physical Review B* **75**, 235426 (2007).

- [26] A. Ghoshala and P. G. Kik, "Theory and simulation of surface plasmon excitation using resonant metal nanoparticle arrays," *J. Appl. Phys.* **103**, 113111 (2008).
- [27] M. -C. Daniel and D. Astruc, "Gold nanoparticles: assembly, supramolecular chemistry, quantum-size-related properties, and applications toward biology, catalysis, and nanotechnology," *Chem. Rev.* **104**, 293–346 (2004).
- [28] A. Chatterjee and D. Chakravorty, "Electrical conductivity of sol-gel derived metal nanoparticles," *J. Mater. Sci.* **27**, 4115–4119 (1992).
- [29] S. Pillai, K. R. Catchpole, T. Trupke, and M. A. Green, "Surface plasmon enhanced silicon solar cells," *J. Appl. Phys.* **101**, 093105 (2007).
- [30] C. Hägglund, M. Zäch, G. Petersson, and B. Kasemo, "Electromagnetic coupling of light into a silicon solar cell by nanodisk plasmons," *Appl. Phys. Lett.* **92**, 053110 (2008).
- [31] K. Nakayama, K. Tanabe, and H. A. Atwater, "Plasmonic nanoparticle enhanced light absorption in GaAs solar cells," *Appl. Phys. Lett.* **93**, 121904 (2008).
- [32] H. A. Atwater and A. Polman, "Plasmonics for improved photovoltaic devices," *Nat. Mater.* **9**, 205–213 (2010).
- [33] J. Verbeeck, D. van Dyck, H. Lichteb, P. Potapova, and P. Schattschneider, "Plasmon holographic experiments: theoretical framework," *Ultramicroscopy* **102**, 239–255 (2005).
- [34] M. Ozaki, J. Kato, and S. Kawata, "Surface-plasmon holography with white-light illumination," *Science* **332**, 218–220 (2011).
- [35] K. E. Shafer-Peltier, C. L. Haynes, M. R. Glucksberg, and R. P. van Duyne, "Toward a Glucose Biosensor Based on Surface-Enhanced Raman Scattering," *J. Am. Chem. Soc.* **125**, 588–593 (2003).
- [36] J. Chen, B. J. Wiley, Z. -Y. Li, D. Campbell, F. Saeki, H. Cang, A. Leslie, J. Lee, X. Li, and Y. Xia, "Gold nanocages: engineering their structure for biomedical applications," *Adv. Mater.* **17**, 2255–2261 (2005).
- [37] S. Roh, T. Chung, and B. Lee, "Overview of the characteristics of micro- and nano-structured surface plasmon resonance sensors," *Sensors* **11**, 1565–1588 (2011).

- [38] J. J. Mock, M. Barbic, D. R. Smith, D. A. Schultz, and S. Schultz, "Shape effects in plasmon resonance of individual colloidal silver nanoparticles," *J. Chem. Phys.* **116**, 6755–6759 (2002).
- [39] S. Lal, S. Link, and N. J. Halas, "Nano-optics from sensing to waveguiding," *Nat. Photonics* **1**, 641–648 (2007).
- [40] M. Pelton, J. Aizpurua, and G. Bryant, "Metal-nanoparticle plasmonics," *Laser & Photon. Rev.* **2**, 136–159 (2008).
- [41] R. Jin, Y. Cao, C. A. Mirkin, K. L. Kelly, G. G. Schatz, and J. G. Zheng, "Photoinduced conversion of silver nanospheres to nanoprisms," *Science* **294**, 1901–1903 (2001).
- [42] Y. Sun and Y. Xia, "Shape-controlled synthesis of gold and silver nanoparticles," *Science* **298**, 2176–2179 (2002).
- [43] N. R. Jana, L. Gearheart, and C. J. Murphy, "Wet chemical synthesis of high aspect ratio cylindrical gold nanorods," *J. Phys. Chem. B* **105**, 4065–4067 (2001).
- [44] M. Liu, M. Leng, C. Yu, X. Wang, and C. Wang, "Selective synthesis of hexagonal Ag nanoplates in a solution-phase chemical reduction process," *Nano Res.* **3**, 843–851 (2010).
- [45] C. N. R. Rao, G. U. Kulkarni, P. J. Thomas, and P. P. Edwards, "Metal nanoparticles and their assemblies," *Chem. Soc. Rev.* **29**, 27–35 (2000).
- [46] M. D. Musick, C. D. Keating, L. A. Lyon, S. L. Botsko, D. J. Pena, W. D. Holliway, T. M. McEvoy, J. N. Richardson, and M. J. Natan, "Metal films prepared by stepwise assembly. 2. construction and characterization of colloidal Au and Ag multilayers," *Chem. Mater.* **12**, 2869–2881 (2000).
- [47] B. D. Gates, Q. Xu, M. Stewart, D. Ryan, C. G. Willson, and G. M. Whitesides, "New approaches to nanofabrication: molding, printing, and other techniques," *Chem. Rev.* **105**, 1171–1196 (2005).
- [48] J. H. Choi, S. M. Adams, and R. Ragan, "Design of a versatile chemical assembly method for patterning colloidal nanoparticles," *Nanotechnology* **20**, 065301 (2009).
- [49] B. E. A. Saleh and M. C. Teich, "Fundamentals of Photonics 2nd ed." (Wiley-Interscience: Hoboken, New Jersey, 2007).

- [50] H. Yun, I. -M. Lee, and B. Lee, "Selectively synthesized silver nanoparticle arrays and their localized surface plasmon resonance," *Photonics 2010: Int. Conf. on Fiber Optics and Photonics* (Guwahati: Viva Books) p 293 (2010).
- [51] H. K. Park, J. K. Yoon, and K. Kim, "Novel fabrication of Ag thin film on glass for efficient surface-enhanced Raman scattering," *Langmuir* **22**, 1626–1629 (2006).
- [52] F. Fievet, J. P. Lagier, and B. Blin, "Homogeneous and heterogeneous nucleations in the polyol process for the preparation of micron and submicron size metal particles," *Solid State Ionics* **32/33**, 198–205 (1998).
- [53] C. Ducamp-Sanguesa, R. Herrera-Urbina, and N. Figlarz, "Synthesis and characterization of fine and monodisperse silver particles of uniform shape," *J. Solid State Chem.* **100**, 272–280 (1992).
- [54] Z. Zhang, B. Zhao, and L. Hu, "PVP protective mechanism of ultrafine silver powder synthesized by chemical reduction processes," *J. Solid State Chem.* **121**, 105–110 (1996).
- [55] P. -Y. Silvert, H.-U. Ronaldo, N. Duvanchelle, V. Vijayakrishnan, and K. T. Elhissen, "Preparation of colloidal silver distributions by the polyol process," *J. Mater. Chem.* **6**, 573–577 (1996).
- [56] H. Wang, X. Qiao, J. Chena, X. Wang, and S. Ding, "Mechanisms of PVP in the preparation of silver nanoparticles," *Mat. Chem. Phys.* **94**, 449–453 (2005).
- [57] G. Ghosh, M. K. Naskar, A. Patra, and M. Chatterjee, "Synthesis and characterization of PVP-encapsulated ZnS nanoparticles," *Optical Materials* **28**, 1047–1053 (2006).
- [58] T. K. Sau and A. L. Rogach, "Nonspherical noble metal nanoparticles: colloid-chemical synthesis and morphology control," *Adv. Mater.* **22**, 1781–1804 (2010).
- [59] C. Wu, . P. Mosher, K. Lyons, and T. Zeng, "Reducing ability and mechanism for polyvinylpyrrolidone (PVP) in silver nanoparticles synthesis," *J. Nanosci. Nanotechnol.* **10**, 2342–2347 (2010).
- [60] R. G. Horn, "Surface forces and their action in ceramic materials," *J. Am. Cerum. Soc.* **73**, 1117–1135 (1990).
- [61] K. Kimura, H. Yao, and S. Sato, "Self-assembling of gold and silver nanoparticles at a hydrophilic/hydrophobic interface: a synthetic aspect and superstructure

- formation," *Synth. React. Inorg., Met.-Org., Nano-Met. Chem.* **36**, 237–264 (2006).
- [62] A. Y. Olenin, A. Yu. A. Krutyakov, A. A. Kudrinskii, and G. V. Lisichkin, "Formation of surface layers on silver nanoparticles in aqueous and water–organic media," *Colloid Journal* **70**, 71–76 (2008).
- [63] K. Shrivastava and H. -F. Wu, "Modified silver nanoparticle as a hydrophobic affinity probe for analysis of peptides and proteins in biological samples by using liquid–liquid microextraction coupled to AP-MALDI-ion trap and MALDI-TOF mass spectrometry," *Anal. Chem.* **80**, 2583–2589 (2008).
- [64] D. K. Owens and R. C. Wendt, "Estimation of the surface free energy of polymers," *J. Appl. Polymer Sci.* **13**, 1741–1747 (1969).
- [65] http://solutions.3m.com/wps/portal/3M/en_US/electronics/home/productsandservices/products
- [66] V. V. Agrawal, G. U. Kulkarni, and C. N. R. Rao, "Surfactant-promoted formation of fractal and dendritic nanostructures of gold and silver at the organic–aqueous interface," *J. Colloid Interface Sci.* **318** 501–506 (2008).
- [67] H. Raether, "Surface plasmons on smooth and rough surfaces and on gratings," (Springer-Verlag: berlin Heidelberg, 1998).
- [68] C. Jiang, S. Markutsya, and V. V. Tsukruk, "Collective and individual plasmon resonances in nanoparticle films obtained by spin-assisted layer-by-layer assembly," *Langmuir* **20**, 882–890 (2004).
- [69] W. -S. Chang, L. S. Slaughter, B. P. Khanal, P. Manna, E. R. Zubarev, and S. Link, "One-dimensional coupling of gold nanoparticle plasmons in self-assembled ring superstructures," *Nano Lett.* **9**, 1152–1157 (2009).
- [70] H. Ditlbacher, J. R. Krenn, B. Lamprecht, A. Leitner, and F. R. Aussenegg, "Spectrally coded optical data storage by metal nanoparticles," *Opt. Lett.* **25**, 563–565 (2000).
- [71] C. J. Orendorff, T. K. Sau, and C. J. Murphy, "Shape-dependent plasmon-resonant gold nanoparticles," *Small* **2**, 636–639 (2006).
- [72] W. A. Murray and W. L. Barnes, "Plasmonic materials," *Adv. Mater.* **19**, 3771–3782 (2007).

- [73] B. Lee, I. -M. Lee, S. Kim, D. -H. Oh, and L. Hesselink, "Review on subwavelength confinement of light with plasmonics," *J. Mod. Optic.* **57**, 1479–1497 (2010).
- [74] M. K. Corbierre and R. B. Lennox, "Preparation of Thiol-Capped Gold Nanoparticles by Chemical Reduction of Soluble Au(I)–Thiolates," *Chem. Mater.* **17**, 5691–5696 (2005).
- [75] L. Eurenus, C. Hagglund, E. Olsson, B. Kasemo, and D. Chakarov, "Grating formation by metal-nanoparticle-mediated coupling of light into waveguided modes," *Nat. Photonics* **2**, 360–364 (2008).
- [76] M. -D. He, Z. -Q Gong, S. Li, Y. -F. Luo, J. -Q. Liu, X. Chen, and W. Lu, "Coupling of localized surface plasmon modes in compound structure with metallic nanoparticle and nanohole arrays," *J. Appl. Phys.* **108**, 093520 (2010).
- [77] <http://www.horiba.com/scientific> & <http://www.biorad-ads.com/> & <http://www.microspectra.com/>
- [78] S. Roh, T. Chung, and B. Lee, "Overview of the characteristics of micro- and nano-structured surface plasmon resonance sensors," *Sensors* **11**, 1565-1588 (2011).
- [79] K. Aslan, M. Wu, J. R. Lakowicz, and C. D. Geddes, "Fluorescent core-shell Ag@SiO₂ nanocomposites for metal-enhanced fluorescence and single nanoparticle sensing platforms," *J. Am. Chem. Soc.* **129**, 1524-1525 (2007).
- [80] K. Ray, R. Badugu, and J. R. Lakowicz, "Metal-enhanced fluorescence from CdTe nanocrystals: a single-molecule fluorescence study," *J. Am. Chem. Soc.* **128**, 8998-8999 (2006).
- [81] J. Malicka, I. Gryczynski, J. Kusba, and J. R. Lakowicz, "Effects of metallic silver island films on resonance energy transfer between N,N'-(dipropyl)-tetramethyl- indocarbocyanine (Cy3)- and N,N'-(dipropyl)-tetramethyl-indodicarbocyanine (Cy5)-labeled DNA," *Biopolymers* **70**, 595 (2003).
- [82] M. G. Moharam, E. B. Grann, and D. A. Pommet, "Formulation for stable and efficient implementation of the rigorous coupled-wave analysis of binary gratings," *J. Opt. Soc. Am. A* **12**, 1068–1076 (1995).
- [83] P. Lalanne and E. Silberstein, "Fourier-modal methods applied to waveguide computational problems," *Opt. Lett.* **25**, 1092–1094 (2000).

- [84] H. Kim, I.-M. Lee, and B. Lee, "Extended scattering-matrix method for efficient full parallel implementation of rigorous coupled-wave analysis," *J. Opt. Soc. Am. A* **24**, 2313–2327 (2007).
- [85] A. W. Katherine and P. van D. Richard, "Localized surface plasmon resonance spectroscopy and sensing," *Annual Review of Physical Chemistry* **58**, 267-297 (2007).
- [86] E. Petryayeva and U. J. Krull, "Localized surface plasmon resonance: nanostructures, bioassays and biosensing," *Anal Chim Acta.* **7**, 8-24.(2011).
- [87] K. S. Lee and M. A. El-Sayed, "Gold and silver nanoparticles in sensing and imaging: sensitivity of plasmon response to size, shape, and metal composition," *J Phys Chem B.* **110**, 19220-19225 (2006).
- [88] A. R. Siekkinen, J. M. McLellan, J. Chen, and Y. Xia, "Rapid synthesis of small silver nanocubes by mediating polyol reduction with a trace amount of sodium sulfide or sodium hydrosulfide," *Chemical Physics Letters* **432**, 491-496 (2006).
- [89] S. H. Im, Y. T. Lee, B. Wiley, and Y. Xia, "Large-scale synthesis of silver nanocubes:the role of HCl in promoting cube perfection and monodispersity," *Angew. Chem. Int. Ed* **44**, 2154-2157 (2005).
- [90] C. M. Copley, S. E. Skrabalak, D. J. Campbell, and Y. Xia, "Shape-controlled synthesis of silver nanoparticles for plasmonic and sensing applications," *Plasmonics* **4**, 171-179 (2009).
- [91] Y. Lu, Y. Yin, Z. -Y. Li, and Y. Xia, "Synthesis and self-assembly of Au@SiO₂ core-shell colloids," *Nano Lett.* **2**, 785-788 (2002).
- [92] C. Graf, D. L. J. Vossen, A. Imhof, and A. van Blaaderen, "A general method to coat colloidal particles with silica," *Langmuir* **19**, 6693-6700 (2003).
- [93] L. M. Liz-Marza 'n, M. Giersig, and P. Mulvaney, "Synthesis of nanosized gold-silica core-shell particles," *Langmuir* **12**, 4329-4335 (1996).
- [94] W. Rechberger, A. Hohenau, A. Leitner, J. R. Krenn, B. Lamprecht, and F. R. Aussenegg, "Optical properties of two interacting gold nanoparticles," *Opt. Comm.* **220**, 137 (2003).
- [95] W. R. Holland and D. G. Hall, "Frequency shifts of an electric-dipole resonance near a conducting surface," *Phys. Rev. Lett.* **52**, 1041 (1984).

- [96] H. R. Stuart and D. G. Hall, "Enhanced dipole-dipole interaction between elementary radiators near a surface," *Phys. Rev. Lett.* **80**, 5663 (1998).
- [97] Z. Fang, B. R. Patterson, and M. E. J. Turner, "Modeling particle size distributions by the Weibull distribution function," *Materials Characterization* **31**, 177–182 (1993).
- [98] B. Gutenberg, "On the layer of relatively low wave velocity at a depth of about 80 kilometers," *Bull. Seism. Soc. Am.* **38**, 121-148 (1948).
- [99] N. Schmerr, "The Gutenberg discontinuity: melt at the lithosphere-asthenosphere boundary," *Science* **335**, 1480-1483 (2012).
- [100] B. Berche, M. Henkel, and R. Kenna, "Critical phenomena: 150 years since Cagniard de la Tour," *Journal of Physical Studies* **13**, 3001-1-3001-4 (2009).
- [101] J. R. Krenn, A. Dereux, J. C. Weeber, E. Bourillot, Y. Lacroute, J. P. Goudonnet, G. Schider, W. Gotschy, A. Leitner, F. R. Aussenegg, and C. Girard, "Squeezing the optical near-field zone by plasmon coupling of metallic nanoparticles," *Phys. Rev. Lett.* **82**, 2590-2593 (1999).
- [102] A. Christ, G. Tikhodeev, N. A. Gippius, J. Kuhl, and H. Giessen, "Waveguide-plasmon polaritons: strong coupling of photonic and electronic resonances in a metallic photonic crystal slab," *Phys. Rev. Lett.* **91**, 183901 (2003).
- [103] R. E. Noskov, P. A. Belov, and Y. S. Kivshar, "Subwavelength modulational instability and plasmon oscillons in nanoparticle arrays," *Phys. Rev. Lett.* **108**, 093901 (2012).
- [104] Y. Lu and A. Lal, "Vacuum-free self-powered parallel electron lithography with sub-35-nm resolution," *Nano Lett.* **10**, 2197-2201 (2010).
- [105] Y. -J. Li, W. -J. Huang, and S. -G. Sun, "A universal approach for the self-assembly of hydrophilic nanoparticles into ordered monolayer films at a toluene/water interface," *Angew. Chem. Int. Ed* **118**, 2599-2601 (2006).
- [106] T. Wen and S. A. Majetich, "Ultra-large-area self-assembled monolayers of nanoparticles," *ACS nano* **5**, 8868-8876 (2011).
- [107] H. Duan, D. Wang, D. G. Kurth, and H. Mhwald, "Directing self-assembly of nanoparticles at water/oil interfaces," *Angew. Chem. Int. Ed* **43**, 5639-5642 (2004).

국문 초록

빛은 매질로서의 물질과 만나면서 반사, 굴절, 간섭, 회절과 같은 변화를 일으키기도 하고 반대로 물질이 빛과 만나면서 에너지를 전달받아 그 분자구조가 변형되기도 한다. 이와 같이 빛은 일종의 전자기파로서 물질을 구성하는 원자나 전자 혹은 분자들과 상호작용을 한다. 한편, 표면 플라즈몬은 외부로부터 빛의 자극을 받아 금속과 유전체 사이의 계면에서 생성되는 자유전자들의 집합체적인 공명상태를 입자화시켜 일컫는 용어로서 금속표면에서 존재하는 특수한 형태의 전자기파에 해당한다. 표면 플라즈몬 역시 빛과 마찬가지로 금속물질과 상호작용을 하는 특성을 가지고 있기 때문에 광학, 물리학, 전자공학, 화학, 재료공학 등의 여러 분야에서 접근할 수 있으며 특히 미래의 차세대 기술로 주목 받는 나노광학의 한 분야로 성장하기 위해서는 학제 간의 공동연구를 통한 심도 깊은 연구가 필요하다. 이러한 견지에서 본 학위논문은, 금속 나노입자의 분산구조를 화학적 방법으로 합성하고 그에 의해 발생하는 표면 플라즈몬의 구조의존적 특성을 광학적 방법으로 측정 및 해석한 연구결과들을 담고 있다.

먼저, 금속 나노입자 배열에 관한 화학적 접근에 초점을 맞춘 것으로서, 은 나노입자의 합성과 동시에 특정 모양을 따라 선택적으로 배열할 수 있는 새로운 화학적 방법을 제시하였다. 은 이온과의 친화도 차이를 보이는 친수성 폴리비닐피롤리돈(polyvinylpyrrolidone)과 소수성 플루오르실란(fluorosilane)을 이용하면 집속이온빔으로 미리 새겨놓은 특정 모양의 참호(trench)에서만 선택적으로 은 나노입자가 생성된다. 이를 통해 제작된 은 나노입자 배열 구조에 대해 입사각 및 편광의존적 산란특성을 측정함으로써 표면 플라즈몬 효과를 확인할 수 있었다. 이 방법은 화학적 합성과 배열의 일원화를 통해 공정의 효율성을 높여주고 미리 설계한 모양대로 금속 나노입자가 배열될 수 있는

가능성을 제시할 뿐만 아니라 플라즈모닉 금속 나노입자 구조물 제작에 활용할 수 있는 가능성을 보여준다.

금속 나노입자에서는 주로 국소적 표면 플라즈몬이 여기되는데 입자 간 간격이 좁아지는 배열 형태가 되면 플라즈모닉 결합이 생겨서 광학적 특성이 변하게 된다. 이러한 원리를 이용하여 국소 표면 플라즈몬이 여기되는 은 나노입자들과 진행 표면 플라즈몬이 여기되는 은 박막을 결합시킨 새로운 나노구조물을 제안하였다. 비록 진행 표면 플라즈몬과 국소 표면 플라즈몬은 진행과 국소라는 서로 상반된 특성을 가지고 있지만, 제안된 나노구조물의 최적화된 조건에서 두 종류의 표면 플라즈몬은 혼합된 상태로 공존할 수 있다. 이때 금속 간의 직접적인 접촉을 방지하기 위하여 정육면체 모양의 은 나노입자(Ag nanocube; AgNC) 둘레를 유전체인 이산화규소(silicon dioxide; SiO₂)의 얇은 막으로 둘러싼 코어-셸(core-shell) 구조의 AgNC@SiO₂ 나노입자를 화학적으로 합성하였다. 이 나노입자들이 은 박막 위에 분포된 구조에 대하여 입사각을 변화시키며 반사스펙트럼을 측정하면 입자 간 거리, 코어의 지름, 셸이나 박막의 두께 등 구조적 변수의 변화에 따라 입사각-파장 그래프 상의 최저반사율 밴드 위치나 기울기가 변하는데 이러한 현상을 2차원 시뮬레이션으로 발견하였고 실험적으로 증명하였다. 이러한 현상을 통해, 최저반사율 밴드의 기울기 변화가 의미하는 것은 전체 표면 플라즈몬 가운데 입사각 의존적인 진행 표면 플라즈몬과 입사각 독립적인 국소 표면 플라즈몬이 차지하는 비중의 변화라고 볼 수 있다. 특히 와이불(Weibull) 분포 모형으로 입자 간 거리의 실제 분포를 모사하여 계산과정에 피드백함으로써, 계산과 실험의 결과를 더 정확하게 비교할 수 있었고 그 결과들 사이의 유사성을 보임으로써, 제안된 금속 구조물에 대한 계산적, 실험적 접근방법의 타당성을 뒷받침할 수 있었다. 또한 최저반사율 밴드 기울기의 변화특성을 이용하여 진행 표면 플라즈몬에 의한 스펙트럼 변화신호와 국소 표면 플라즈몬에 의한 형광이미지를 동시에 측정함으로써 바이오 센서와 같은 실용적 기기에 적용할 수 있음을 보여주었다.

위의 연구에서 더 나아가, 진행 표면 플라즈몬과 국소 표면 플라즈몬 사이의 결합 현상을 더 규명하기 위하여 은 박막 없이 AgNC@SiO₂ 나노입자들만의 고밀도 격자배열 구조를 제안하였고 이 구조로부터 진행 및 국소 표면 플라즈몬 간의 전이과정 및 중간상태를 발견할 수 있었다. 진행 혹은 국소 표면 플라즈몬이 단독으로 존재할 때에는 입사각-파장 그래프에서 최저반사율 밴드가 대각선 방향 혹은 수직 방향으로 각각 한 개씩 존재하는 반면, 둘 사이에 플라즈모닉 결합이 생기는 영역에서는 대각선과 수직 방향의 밴드가 교차하는 형태와 유사하게 변형된 두 개의 최저반사율 밴드가 존재한다. 이때 각각의 변형된 밴드에서는 두 종류의 표면 플라즈몬 간의 전이가 서로 반대방향으로 일어나고 두 밴드의 교차점에서는 반사율이 높아지는 준안정적인 안장점 특성을 보이며 그 주변으로 진행 및 국소 표면 플라즈몬의 변화가 급격하게 일어난다. 특히 이러한 중간적 특성을 실험적으로 구현하기 위해서는 금속 나노입자들 사이의 간격이 수 나노미터에 해당하는 매우 좁은 조건을 만족해야 하는데, 일반적으로 배열 구조를 정확하게 만들 수 있는 탑-다운(top-down) 방식의 리소그래피 방법으로는 최소선폭의 한계로 인해 실제 구조물의 제작이 불가능하기 때문에 버텀-업(bottom-up) 방식의 하나인 자기조립법(self-assembly method)을 이용하여 고밀도의 AgNC@SiO₂ 단일층을 형성할 수 있었다. 제안된 구조를 최대한 모사한 샘플의 반사 스펙트럼을 위와 동일한 방법으로 측정하고 나노입자 간 간격의 확률적 분포 정보를 계산에 반영한 결과, 시뮬레이션과 실험 결과 사이에서 일관된 유사성을 도출할 수 있었다. 이러한 유사성은 제안된 구조에 대한 계산적, 실험적 접근 방법의 타당성과 이 구조의 중간적 플라즈모닉 특성의 유효성을 뒷받침한다고 판단된다.

이상과 같이 본 연구에서는 표면 플라즈모닉 특성을 가지는 금속 나노입자를 원하는 모양에 따라 효율적으로 배열하기 위해 합성과 배열이 동시에 일어나는 새로운 화학적 방법을 제시하였고 이같은 금속 나노입자 배열 구조에서 빈번히 나타날 수 있는, 중요하지만 연구가 많지 않았던 이중 표면 플라즈몬 간 결합의

새로운 특성을 밝히기 위해 두 가지 금속 나노입자 배열 구조를 제안하고 연구하였다. 이 연구의 실험에서 사용된 모든 샘플은 주로 화학적 방법으로 제작하였고 그 플라즈모닉 특성은 광학적 방법으로 측정하였으며 시뮬레이션을 이용하여 물리적 해석 및 상호간 검증을 시행하였는데 일련의 이러한 복합적 연구 방법은 학제 간 연구 혹은 융합연구의 한 모델이 될 수 있을 것으로 기대한다.

주요어 : 표면 플라즈몬, 진행 표면 플라즈몬, 국소 표면 플라즈몬, 금속 나노입자 배열, 플라즈모닉 결합

학 번 : 2009-30200